INFLUENCE OF THE MEMBRANE ION EXCHANGE CAPACITY ON THE CATALYST LAYER OF PROTON EXCHANGE MEMBRANE FUEL CELL

by

TITICHAI NAVESSIN

B.Sc. (Hons.), Imperial College, University of London, 1999

A THESIS SUBMITTED IN PARTIAL FULFILLMENT OF
THE REQUIREMENTS FOR THE DEGREE OF

DOCTOR OF PHILISOPHY

In the
Department of Chemistry

SIMON FRASER UNIVERSITY

October 2004

APPROVAL

Name:	Titichai Navessin
Degree:	Ph.D.
Title of Thesis:	Influence of the Membrane Ion Exchange Capacity on the Catalyst Layer of Proton Exchange Membrane Fuel Cell.
Examining Committee:	
Chair:	Dr. N.R. Branda (Professor)

Dr. S. Holdcroft (Professor) Senior Supervisor

Dr. I.D. Gay (Professor) Committee Member

Dr. P.C.H. Li (Assistant Professor) Committee Member

Dr. G.R. Agnes (Associate Professor) Internal Examiner

Dr. G. Lindbergh (Professor) External Examiner
Department of Chemical Engineering and Technology,
Royal Institute of Technology, Sweden

Date Approved: October 13, 2004

Abstract

This work investigated the effect of ion exchange capacity (IEC) of polymer electrolyte membranes (PEM) on the PEM fuel cell cathode catalyst layer. A series of radiation grafted ethylene tetrafluoroethylene-g-polystyrene sulfonic acid (ETFE-g-PSSA) membranes was used to provide a systematic variation of IEC. A method to fabricate gas diffusion electrodes (GDEs) was adapted and custom-made GDEs with known compositions were prepared. Oxygen electrochemistry, mass transport properties, water absorption behaviour and proton conductivity were studied in relation to the IEC. Electrochemical characterization including cyclic voltammetry, electrochemical impedance spectroscopy and linear sweep voltammetry were employed. The agglomerate model for cathodes was adapted and used to extract mass transport parameters from experimental results.

Prior to investigation in fuel cell systems, studies were performed in a half-fuel cell, which simplified complicating parameters associated with fuel cell operation. It was found that membranes with higher IEC resulted in a higher active surface area of electrode. In contrast, they exhibited lower oxygen reduction performance. The extracted effective diffusion coefficient of oxygen and O_2 solubility in the catalyst layer was used to estimate the extent of flooding, which revealed that ~67 - 70% of void space was filled with water. The membrane's IEC regulates the extent of flooding of the cathode, which in turn affects its electrochemical characteristics.

The investigation under operating fuel cell conditions revealed an increase in fuel cell performance with increasing IEC –a contradicting trend to that found for the half-fuel cell. This is explained by the interplay of electroosmotic flux and hydraulic counterflux in the membrane which affects water management in the membrane electrode assembly (MEA). The influence was most significant in the cathode catalyst layer, where it affects mass transport and electrochemical characteristics. It was found that the higher IEC facilitated better water management in MEAs.

Comparing results obtained with half fuel cell and fuel cell systems revealed insights into the state of hydration and effective use of Pt in the catalyst layer. The two types of measurements provide a convenient approach to study the interplay of different mechanisms of water flux in the membrane.

Dedication

This thesis is dedicated to

my grandmother, Jumlong Vongtase, who was always there for me,

and to

my parents, Vichai and Titima Navessin, whose dedications and personal
sacrifices have given me the fortunes I have today.

Acknowledgements

I would like to thank my senior supervisor Prof. S. Holdcroft for supervision, support and guidance throughout this thesis. The supervisory committee members, Prof. I. Gay and Prof. P. Li, are thanked for supervising and reviewing this thesis.

Thanks to the members of the theory and modelling team of the Institute for Fuel Cell Innovation, National Research Council, Dr. Z. Liu, Dr. Q. Wang, Dr. D. Song, Prof. M. Eikerling and Dr. B. Andreaus for technical guidance and friendship during the joint SFU-NRC collaboration research in the modelling of membrane electrode assembly for the proton exchange membrane fuel cells.

The staff members of the electronic shop and the machine shop of the faculty of science are thanked for valuable discussions and technical supports.

Past and present members of the Holdcroft research group are thanked for their friendship and moral supports.

Lastly, and perhaps the most influential, Mr. C. P. Morris, Mr. M. S. Sprig and Mr. M. A. Mason, my high school science teachers (Ealing College Upper School, London, UK), are thanked for their dedication to educating me and for inspiring my scientific career.

Table of Contents

List of Figures

List of Tables

List of Abbreviations and Symbols

Symbols

A_a	Catalyst surface area per unit volume, m^{-1}
c_0	Position dependent concentration of O_2, mol l^{-1}
c_0^{ref}	Oxygen reference concentration at the surface of agglomerate in equilibrium with 1 atm. O_2 pressure at open circuit potential, mol l^{-1}
D	Diffusion coefficient of O_2
i_0	Exchange current density, A cm^{-2}
i	Total current density, A cm^{-2}
j	Protonic current density, A cm^{-2}
H	Henry's constant for O_2
L	Thickness, cm
P	Cathode oxygen pressure, atm
R_a	Agglomerate radius, cm
R_{ORR}	Local chemical reaction rate in the agglomerate, mol cm^{-3} s^{-1}
T	Cell temperature, K
t	Critical exponent
x	Catalyst layer depth, cm
v	Volume fraction

Greek

α_r	Cathode transfer coefficient
η	Local potential difference between metal potential and electrolyte potential, V
σ	Proton conductivity, S cm^{-1}
ρ_a	Agglomerate density in the catalyst layer, cm^{-3}
τ	Tortuosity of the catalyst layer
Θ	Heaviside step function

Subscripts

a	Agglomerate
p	Percolation threshold
C	Carbon
CL	Catalyst layer
g	gas
GDL	gas diffusion layer
O	oxygen
N	Nafion
v	void

Superscripts

eff	effective
s	surface

Abbreviations

ESA	Electrochemically active surface area
GDE	Gas diffusion electrode
GDL	Gas diffusion layer
HMEA	Half-membrane electrode assembly
IEC	Ion exchange capacity
MEA	Membrane electrode assembly
OCP	Open circuit potential
ORR	Oxygen reduction reaction
PEM	Proton exchange membrane
PEMFC	Proton exchange membrane fuel cell

Chapter 1 : Introduction

1.1 Proton Exchange Membrane Fuel Cell (PEMFC)

Development of proton exchange membrane fuel cell (PEMFC) has gained much momentum in the past decade. One of the main thrusts is the need for environmentally friendly solution to power generation in order to satisfy growing demands for power consumption worldwide. PEMFCs possess many attractive characteristics such as low operating conditions (10 – 90 °C), near zero emission, ultra-low operating noise level, high thermodynamic efficiency and high power density. These make them suitable for large scale power generation, automotive and small mobile applications.

The basic principles of PEMFC is illustrate in Figure 1.1. During an operation, hydrogen gas is oxidized at the anode (equation 1) forming protons, which are transported through the proton exchange membrane to the cathode. Oxygen reduction reaction (ORR) (equation 2) occurs at the cathode reducing protons and oxygen to water. The electronic conduction in an external pathway provides useful electricity.

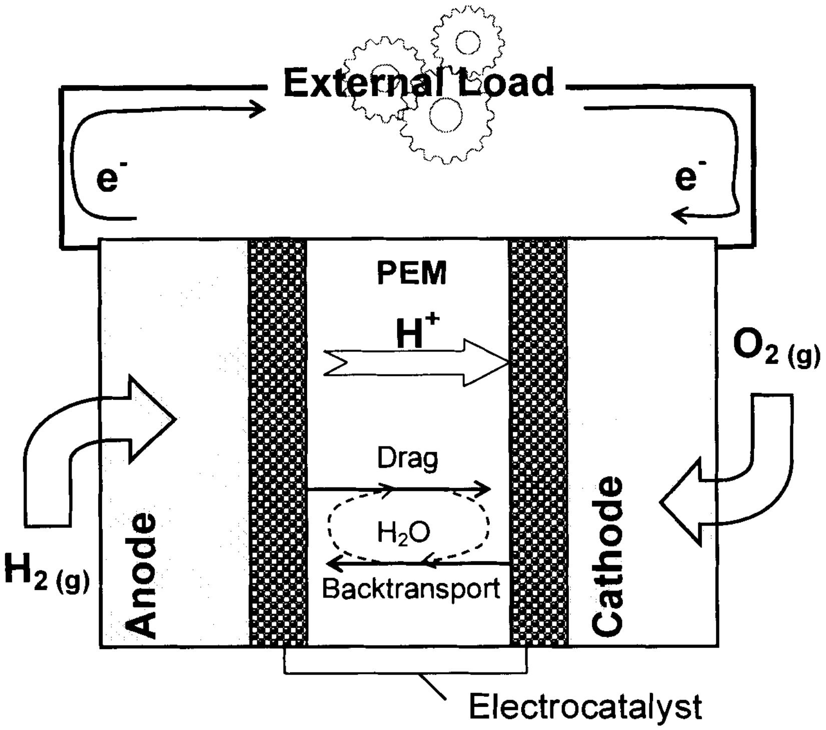

Figure 1.1: Basic principles of proton exchange membrane fuel cell.

$$H_2 \rightarrow 2H^+ + 2e^- \qquad E^o = 0.000\,V \qquad (1)$$

$$\frac{1}{2}O_2 + 2H^+ + 2e^- \rightarrow H_2O \qquad E^0 = 1.229\,V \qquad (2)$$

$$H_2 + \frac{1}{2}O_2 \rightarrow H_2O \qquad \begin{array}{cc} \Delta H\,(\text{KJ mol}^{-1}) & \Delta G\,(\text{KJ mol}^{-1}) \\ -286 & -237 \end{array} \qquad (3)$$

At equilibrium, the ideal reversible cell potential is 1.23 V. For the overall electrochemical conversion process, shown in equation (3), the thermodynamic efficiency (η_t) defined as the ratio of electrical output (ΔG) to the maximum heat output (ΔH) is 0.83. This is much higher than the efficiency of conventional internal combustion engines (< 50 %). Nevertheless, under the maximum thermodynamic efficiency, the cell would still produce 17 % heat.

Protons transport in the membrane requires H^+ ions to be solvated in order to achieve sufficient conductivity. This requires the membrane to be well hydrated during fuel cell operation. Humidification of inlet gases before fed into the cell is often done to prevent membrane dehydration. Transport of protons in the membrane[1] is thought to occur by migration and Grotthus hopping mechanism. Migration of solvated H^+ ions from the anode to the cathode creates electro-osmotic drag of water associated with the hydration shell[2-4]. This creates a water gradient within an MEA. Backtransport of water from cathode to anode occurs concertedly reducing the water gradient built up. If net water transport across the membrane is substantial, the membrane / anode interface has tendency to dehydrate. This may lead to an increase in the overpotential for hydrogen oxidation reaction (HOR), high membrane protonic resistance, and consequently, a reduction of fuel cell performance. In parallel to the anode dehydration, the flooding of the cathode could occur if water cannot be rapidly removed. This represents the water management issue in PEMFC[5-10].

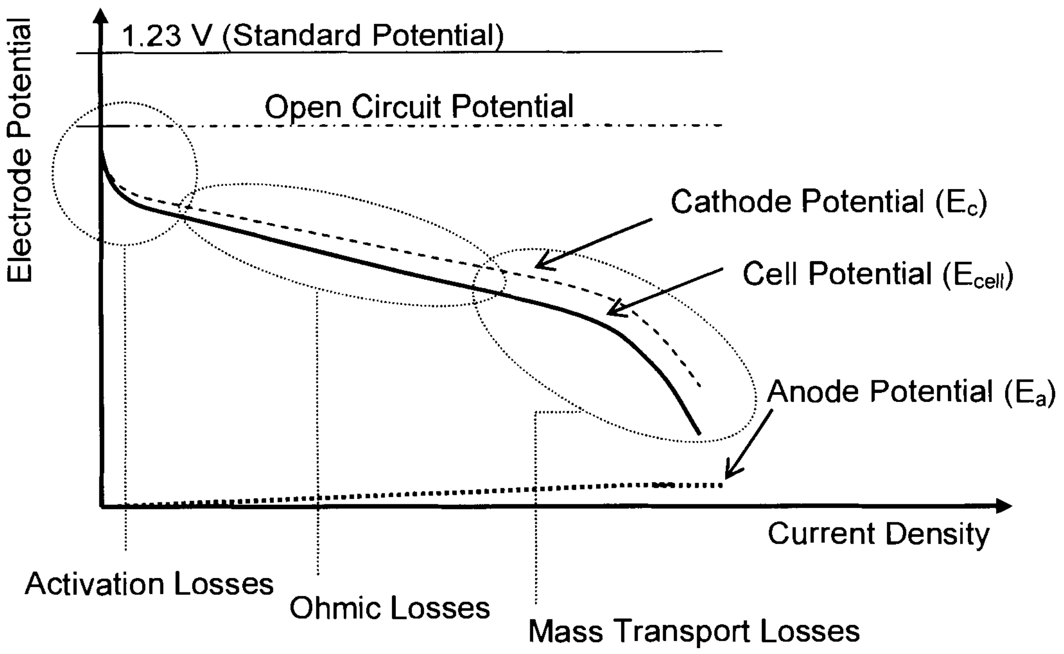

Figure 1.2: Typical fuel cell polarization curve.

Performance of a fuel cell is measured by its polarization characteristics, a profile of the electrode potential as a function of output current density. The cell potential (E_{cell}) is the difference between the potential of the cathode (E_c) and the anode (E_a).

$$E_{cell} = E_c - E_a \tag{4}$$

In order to draw a net current density, the electrochemical reaction equilibrium must be perturbed (or commonly referred as polarized). The extent of polarization is quantified by the overpotential (η), which is the deviation of electrode potential (E) from its equilibrium (E_{eq}).

$$\eta = E - E_{eq} \tag{5}$$

In the kinetically controlled region, η is related to current density (i) by Butler-Volmer equation (6) [11].

$$i = i_0 e^{-\frac{\alpha nF}{RT}\eta} - i_0 e^{\frac{(1-\alpha)nF}{RT}\eta} \tag{6}$$

where α is the transfer coefficient, n is the number of electrons transferred in the reaction. R, T and F are ideal gas constant, temperature and Faraday's constant, respectively. The important parameter is the exchange current density (i_0) which measures the rate of exchange of electrons at equilibrium, and is related to the concentrations of the oxidizing (C_O) and reducing (C_R) species, and the reaction rate (k_0) by

$$i_0 = nFk_0 c_O^{(1-\alpha)} c_R^{\alpha} \tag{7}$$

In a polarization profile, η is considered the loss of potential in order to achieved output current density. A typical polarization curve is illustrated in Figure 1.2. There are three main sources of potential loss: (i) the activation overpotential (η_{ac}) is related to the slow electrode kinetics of ORR because its i_0 (10^{-9} A cm^{-2}) is much smaller than that of HOR (10^{-3} A cm^{-2})[11], (ii) the Ohmic overpotential is related to the internal resistances of the fuel cell which consist of ionic resistance in the membrane, electronic resistance within the electrodes and interfacial contact resistances between components; and (iii) the mass transport overpotential which occurs when supply of reactant to catalytic sites is slower than its consumption rate.

1.2 Oxygen Reduction Reaction (ORR)

The overpotential of oxygen reduction is the predominant source of activation overpotential in PEMFCs. Despite significant efforts to increase the ORR kinetics, Pt remains one of the most electroactive material[12,13]. Oxygen reduction occurs via two reaction pathways. The first pathway is the direct 4-electron reduction.

$$O_2 + 4H^+ + 4e^- \rightarrow 2H_2O \qquad E^0 = 1.23\,V \qquad (8)$$

The second pathway involves two 2-electron steps via a formation of hydrogen peroxide.

$$O_2 + 2H^+ + 2e^- \rightarrow H_2O_2 \qquad E^0 = 0.67\,V \qquad (9)$$

$$H_2O_2 + 2H^+ + 2e^- \rightarrow H_2O \qquad E^0 = 1.77\,V \qquad (10)$$

The hydrogen peroxide can also undergo chemical decomposition

$$2H_2O_2 \rightarrow 2H_2O + O_2 \qquad (11)$$

Depending on electrode materials[14], electrolytes and electrode potentials[15], the ORR can proceed by either pathway or by parallel pathways. A recent study[15] using rotating ring disc electrode to detect the presence of H_2O_2 during ORR has revealed that for carbon supported Pt[1] catalyst the 4-electron pathway predominates when electrode potential is more positive than 0.65 V. The 2-electron pathway initiates at electrode potential below 0.65 V and rapidly predominates at potential less than 0.20 V. In view of PEMFC operation,

---

[1] Also known as Pt-on-C or Pt/C

minimizing the 2-electron pathway is beneficial because the H_2O_2 intermediate is known to produce $HO_2\cdot$ radicals[14] which attack the membrane's chemical structure causing membrane degradation[16-18] and early failure of fuel cell operation.

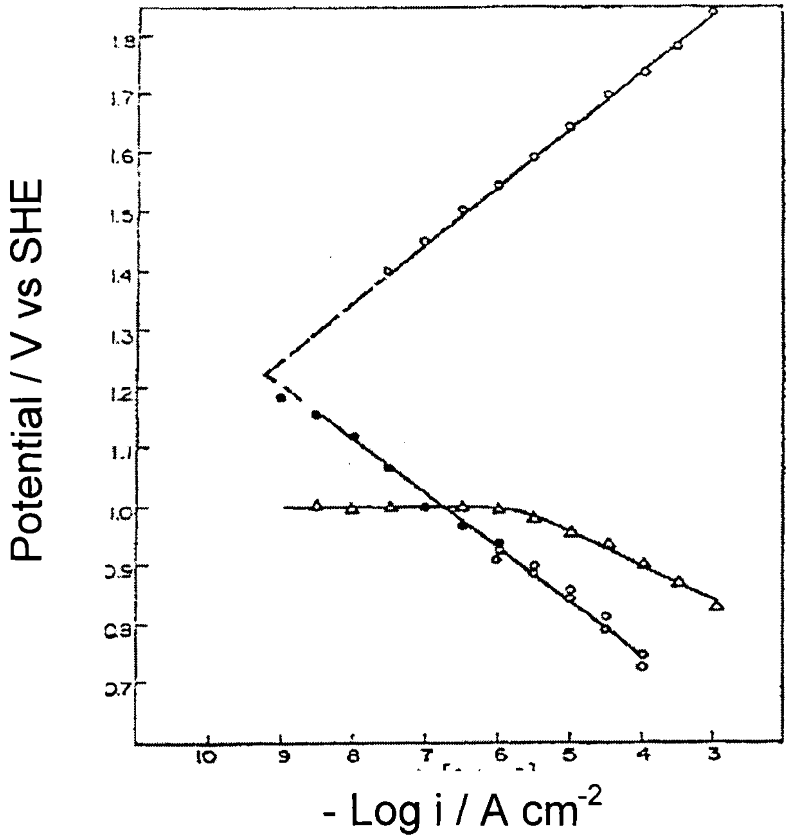

Figure 1.3: Oxygen reduction on Pt electrodes in acid solutions. (•) cathodic line obtained from Pt oxide-covered surface starting from reversible potential; (O) cathodic line obtained by reversing anodic current and fast measurements; (Δ) cathodic line using oxide-free Pt surface. Reprinted from ref.[19]. Copyright (1966), with permission from Elsevier.

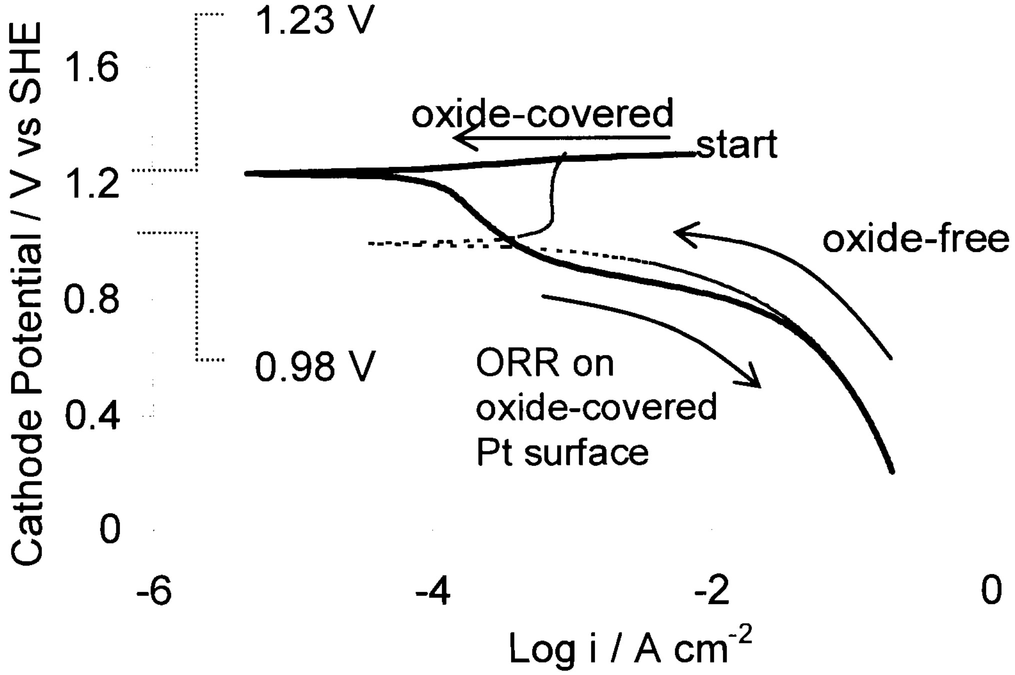

Figure 1.4: Potential cycling of oxygen reduction on a gas diffusion electrode (0.5 mg Pt cm^{-2}. 20 wt% Pt-on-C) measured in a half-fuel cell apparatus using 1.0 M H_2SO_4 electrolyte at 25 °C and 1 atm. oxygen. The electrode was anodized at 1.4 V for 1 min before cycling at 1 mV s^{-1}.

In many electrochemical systems involving ORR, the reversible oxygen potential (E^0) at 1.23 V is rarely observed. This is because ORR is highly irreversible, as reflected in the very low exchange current density (~10^{-9} A cm^{-2}). In an acid electrolyte, the electrode potential at zero net current (rest potential[2], E_{rest}) is most often observed between 0.92 and1.05 V [20]. The discrepancy arises because Pt surface be covered by oxides[19]. The extent of oxide coverage varies with electrode potential, electrode material and pH[20,21]. Figure 1.3 illustrates the existence of E_{rest} for oxide-covered and oxide-free Pt

---

[2] The definition of rest potential applies to all reaction regardless of their reversibility nature. This distinguishes it from the standard reversible potential (E^0).

surface. When Pt is fully oxidized by anodizing electrode at a potential more positive than ~ 1.3 V or by pre-treating with a strong acid, a thick layer of Pt oxide is formed and the reversible E_{rest} at 1.23 V is observed[19]. On the other hand, when Pt electrode is electrochemically reduced to form oxide-free Pt surface, E_{rest} is 0.98 V.

Under many practical conditions including PEMFC, various Pt oxide surfaces exist (reaction 12 to 15) and the interplay of these surfaces results in a mixed electrode potential. The open circuit potential (OCP) for Pt-on-C catalyst is often observed in the region of 0.9 to 1.0 V. Compared to the thermodynamics value of 1.23 V, this represents ~25 % loss of electrode potential.

$$PtO_3 + 2H^+ + 2e^- \square \quad PtO_2 + H_2O \qquad E^0 = 1.48\ V \tag{12}$$

$$PtO_2 + 2H^+ + 2e^- \square \quad Pt(OH)_2 \qquad E^0 = 1.11 V \tag{13}$$

$$Pt(OH)_2 + 2H^+ + 2e^- \square \quad Pt + 2H_2O \qquad E^0 = 0.98\ V \tag{14}$$

$$PtO + 2H^+ + 2e^- \square \quad Pt + 2H_2O \qquad E^0 = 0.88\ V \tag{15}$$

Reduction of oxygen on the oxide-covered and the oxide-free surfaces have slightly different polarization profiles. This causes the hysteresis in the polarization. Figure 1.4 shows a hysteresis in a potential cycle of Pt/C electrode (measured in this study). The implication of this hysteresis on the dynamics of fuel cells operation may be an important one. A fuel cell powered vehicle would produce a lower power output upon accelerating from idle (cathodic sweep) than that during a deceleration to stop (anodic sweep). The state of oxide coverage of

Pt, and its history in the cycle would be another factor that determines the power output of the fuel cells.

1.3 Membrane Electrode Assembly (MEA)

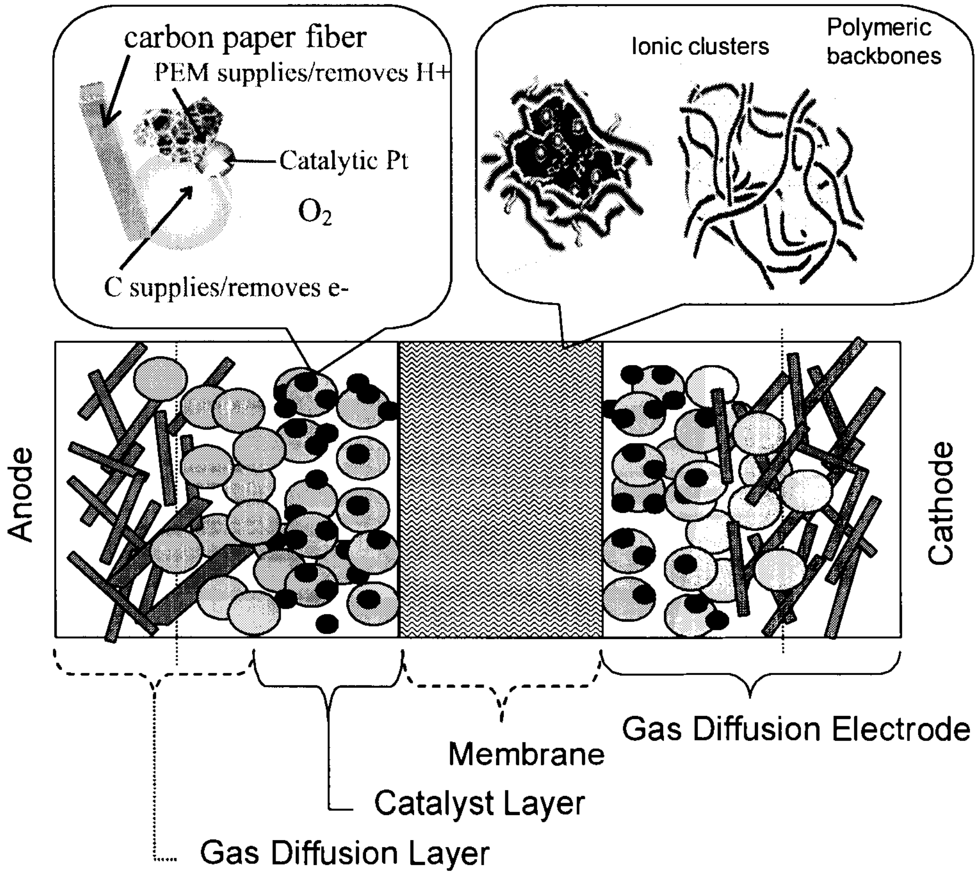

Figure 1.5: Scheme of a cross-sectional plane of a membrane electrode assembly (MEA). Insets depict three-phase interface in the catalyst layer (left) and ion cluster morphology of proton exchange membrane (right, reprinted from ref. [22] with permission).

At the heart of PEMFC is a membrane electrode assembly (MEA), comprising of a proton exchange membrane sandwiched between two gas diffusion electrodes (GDEs). Figure 1.5 depicts the composition and structure of

MEA. The gas diffusion electrode consists of catalyst layer deposited on carbon cloth or carbon paper substrate. Located at the membrane / electrode interface, the catalyst layer contains Pt electrocatalyst dispersed on high surface area carbon black: this effectively utilizes Pt by maximizing its surface area to mass ratio. The carbon-supported Pt[3] particles are held together by binding agents such as polytetrafluoroethylene (PTFE) and/or a proton conducting polymer. The hydrophobic polymer backbone of PTFE serves as a wet-proofing agent in the catalyst layer, thereby reducing the propensity of electrode flooding and promoting gas permeable pathways in order to achieve rapid gas transport to catalytic sites[12]. The gas diffusion layer serves as a substrate for catalyst layer, an electron-conducting medium between catalyst layer and current collecting plate, and a uniform distributor of reactant gases from flow field channels to the catalyst layer[23,24].

At the membrane / electrode interface, three-phase interface exists between reactant gas, electronically conducting Pt/C and proton conducting membrane. These phases provide the required ingredients for hydrogen oxidation and oxygen reduction electrochemical reactions. Consequently, only Pt particles located within the three-phase interface are electrochemically active[25].

1.4 Gas Diffusion Electrode (GDE)

Three-dimensional porous electrodes are important component in many industrial electrochemical reactors[26-28] because they provide high electrochemical conversion rate per unit geometrical area. The gas diffusion

---

[3] Also known as Pt-on-C or Pt/C

electrode is a class of porous electrode that facilitates electrochemical reactions involving gas, liquid and solid phases. There are three functional requirements for a GDE, which are high electronic conduction, high protonic conduction and high gas permeation pathways[29]. These requirements are inherently conflicting because conduction is proportional to the volume fraction of the conducting phase. An increase in volume fraction of one component leads to a reduction of other components. Consequently, the best performing electrode will be the result of a compromise. This represents a common optimization problem for porous electrodes[30]. In the case of GDEs for fuel cell applications, the conflicting components are namely, Pt loading, impregnated Nafion loading and weight percentage of Pt-on-C. The inter-relationships of these parameters are reviewed in the Section 1.4.2.

1.4.1 Development of Gas Diffusion Electrodes

Since the early applications of PEMFCs in NASA's Gemini space missions in 1960s, many breakthroughs in improvements of fuel cell performance were the direct results from a better understanding of gas diffusion electrode, membrane materials and MEA[13]. PEMFC systems for Gemini flights employed electrodes containing high loading of Pt black (4 mg cm^{-2}) and hydrocarbon based membranes (see section 1.5). The use of Pt black limits accessible surface area as a result of particles agglomeration (10 - 20 nm average diameter). High Pt loading is, therefore, required in order to provide sufficient active surface area. By replacing Pt black with carbon supported Pt catalyst, the surface area of Pt is more effectively utilized since Pt particles are dispersed onto high surface area carbon support, e.g. Vulcan XC-72® by Cabot Corporation. This reduces particle agglomeration (average size ~ 3 nm) and enhances the specific surface area (70 - 140 m^2 g^{-1} compared to 30 m^2 g^{-1} for Pt black). Subsequently, a 10-fold reduction of Pt loading is achieved while maintaining the same the performance[31].

Without the presence of impregnated Nafion in the catalyst layer, a gas diffusion electrode is electrochemically active at the membrane / catalyst layer interface only. The electrochemically active three-phase interfacial area is extended throughout the catalyst layer when proton conducting phase is incorporated into it. Essentially, this transforms a 2-dimensional active area into a 3-dimensional electrode. Impregnation of Nafion is achieved either by applying dilute solubilized Nafion onto catalyst layer surface[32] or solution mixing Nafion ionomers with Pt-on-C prior to formation of catalyst layer[33]. Consequently, Nafion impregnation increases Pt utilization from < 10 % to > 25 % [13].

The interface between membrane and GDE is crucial for good proton transport between the bulk membrane and the impregnated ionomers. Improvement of this interfacial binding can be achieved by hot-pressing the electrode / membrane / electrode unit under appropriate conditions[13] of temperature (130-160 ^{0}C for Nafion), pressure (1000 -2000 Psi) and time (30-90 s). A hot-pressed MEA containing Pt-on-C and impregnated Nafion exhibits ~10-fold performance improvement compared to the MEAs used in Gemini missions[13,32,34,35].

In the past decade, refinements of MEA by using various novel materials and fabrication methods further improve Pt utilization (> 50%) and reduce the catalyst layer thickness (1 – 20 μm). A summary of the development is summarized in Table 1.1.

Table 1.1: Summary of development of the gas diffusion electrode since 1960s to the present

Year	1960s	1980-1990	1990s-present
Dimension of active layer	2-D	3-D	3-D
Catalyst	Pt black	Pt-on-C	Pt-on-C
Pt loading (mg Pt/cm^2)	~ 4	~0.4`	0.2-0.05
Catalyst thickness (μm)	100	50	< 20-1
Particle size (nm)	10	3	1 - 3
Pt Utilization (%)	5 -10	25	> 50

1.4.2 Factors Influencing the Performance of GDEs

The factors affecting performance of GDE can be broadly categorized into material properties, electrode composition and fabrication method. These factors are interdependent. In view of material, the conventional standard GDE materials are carbon paper, Pt/C (Vulcan XC-72®) and impregnated Nafion ionomer. Novel materials for GDEs are continually being developed, and many have demonstrated significant improvements[13,36]. Within this context, the standard materials are considered. In regards to fabrication, several methods can be employed. A typical approach is to deposit a solution of catalyst ink containing Pt/C and Nafion ionomer onto gas diffusion layer to form gas diffusion electrodes. This is followed by hot-pressing the electrodes to a membrane to form an MEA. The second approach is to deposit the catalyst ink directly onto a membrane forming a "catalyst coated membrane". Two uncatalyzed gas diffusion layers are assembled on both sides of the catalyzed membrane and hot-pressed to form MEA. For the aspects of electrode composition, the catalyst layer composition, strongly influences the electrochemical kinetics of fuel cell. The important parameters are the Pt loading, the impregnated Nafion content, the thickness of catalyst layer, and the weight ratio of Pt to C. Inter-relationships exist between these paramters. Their influence on the electrode performance is discussed in the following paragraphs.

Reducing of Pt loading without sacrificing performance has always been a goal in PEMFC research because Pt is expensive and limited in supply[37-41]. Dispersion of Pt on carbon support improves the surface to mass ratio. The extent of dispersion is conventionally characterized by the weight ratio of Pt to C expressed as "wt%". A decrease in the weight ratio represents more carbon-support per Pt particle, and therefore a higher dispersion and a larger Pt specific surface area but also a tendency to make thicker[4] or denser[5] catalyst layer[42]. The effect of the weight ration on Pt specific surface area is illustrated in Table 1.2.

---

[4] When compared with a higher wt% at a constant porosity of catalyst layer.

[5] When compared with a higher wt% at a constant thickness of catalyst layer.

Table 1.2: Effect of weight ratio of Pt to C on specific surface area. Reprinted from ref. [43]. Copyright (1999), with permission from Elsevier.

Catalyst type	Surface area/Pt mass, A_s (m^2/g)
10% Pt on carbon black	140
20% Pt on carbon black	112
30% Pt on carbon black	88
40% Pt on carbon black	72
60% Pt on carbon black	32
80% Pt on carbon black	11
Pt black	28

The effect of the weight ratio on fuel cell performance is illustrated in Figure 1.6. At low Pt loading (< 0.2 mg Pt cm^{-2}), the current densities of all weight ratios are limited by Pt surface area. A lower weight ratio (20 wt%.) provides higher current densities because of increased surface area. At high Pt loading (>0.4 mg Pt cm^{-2}), the consumption rate of reactant increases and the current densities are mass transport limited. The higher weight ratios (40 and 60 wt.%) show a slight improvement when compared with 20 wt.%. This is attributed the lower content of carbon in the catalyst layer reducing the thickness and improving the mass transport. When using a lower weight ratio catalyst, the benefit from increasing surface area is offset by mass transport limitations.

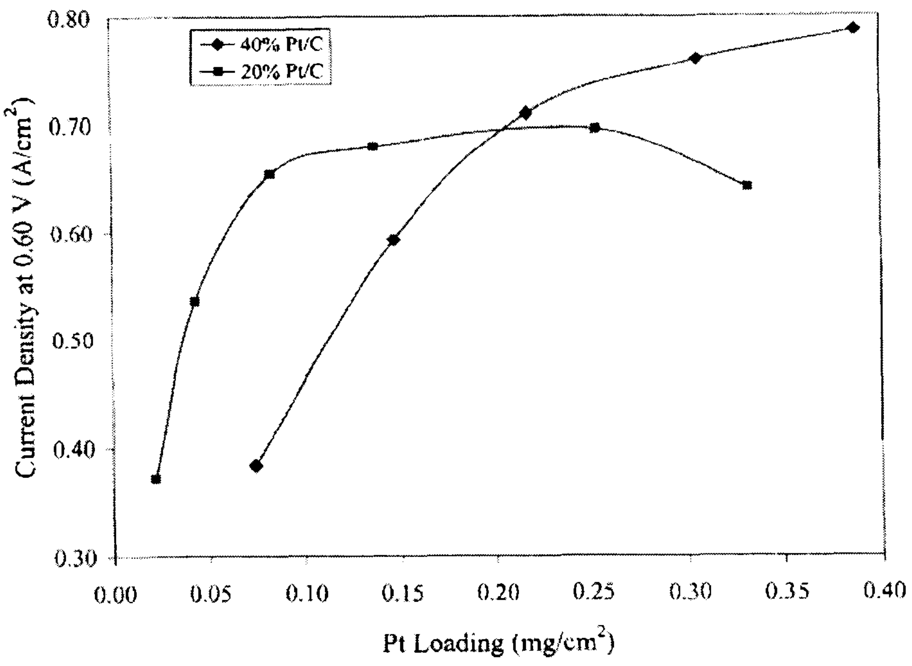

Figure 1.6: Influence of Pt loading and Pt / C weight ratio on the performance of fuel cell. Comparing 20 wt% to 40 wt% Pt/C. Reprinted from ref. [44]. Copyright (2003), with permission from Elsevier.

The Nafion content in the catalyst layer affects proton conductivity, electrochemically active surface area, propensity of flooding and mass transport limitation of an electrode[32,45]. Conventionally, Nafion content is quantified by the weight ratio of the impregnated Nafion to the catalyst layer (Pt, C and impregnated Nafion), and is expressed in wt%. Although the important parameter representing the effect of Nafion is its volume fraction, Nafion is dimensionally unstable (upto 15 vol% expansion upon hydration) which causes the volume fraction to change depending on operating conditions. Hence, the weight ratio is preferential. Figure 1.7 illustrates the influence of impregnated Nafion on electrode performance. At low Nafion content (10 - 30 wt%), increasing the Nafion content increases the three-phase interface within the catalyst layer, improves the proton conductivity and the current density increases. At high Nafion content (> 45 wt.%), the hydrophilicity associated with SO_3^- groups in Nafion increases water content. This dramatically reduces the effective porosity of the catalyst layer, and consequently the limiting current density decreases. Within an intermediate Nafion content (30 – 40 wt%), many studies[44-47] have shown that a compromise is achieved and the maximum performance can be obtained.

Without fully considering other complicating parameters associated with materials and fabrication methods, the parameters of electrode compositions demonstrate a level complexity that must be taken into account in the development of GDEs. The inter-relationships between Pt loading, Pt/C (wt%) and Nafion content (wt%) control the electrochemically active surface, thickness, porosity, electrical conductivity and proton conductivity within the catalyst layer, which in turn determines the electrode performance.

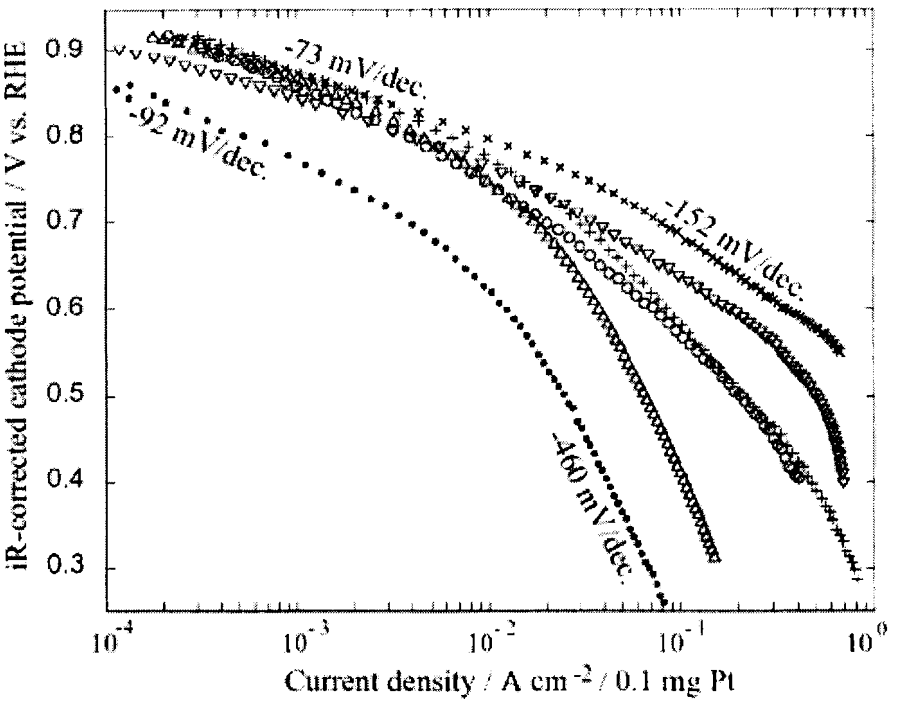

Figure 1.7: Effect of impregnated Nafion in the catalyst layer on PEMFC performance (50 °C and 1 atm).Nafion wt.%: (¨) 10; (+) 30; (X) 36; (∇) 43; (O) 50; (Δ) 70. Reprinted from ref. [46]. Copyright (2003), with permission from Elsevier.

1.5 Proton Exchange Membrane (PEM)

The proton exchange membrane is a polymer network containing covalently bonded negatively charged functional groups capable of exchanging cations. The polymer matrix consists of polymer backbone, which can be hydrocarbon-based polymers such as polystyrene and polyethylene or their fluorinated polymer analogs. The type of polymer matrix strongly influences the physical properties of the membrane[48]. For fuel cell applications, sulfonic acid functional group (SO_3^-) is the most widely used because the protons are fully dissociated in the presence of water, and thereby functioning as a good hydronium ion conductor.

The hydrophobic backbones create a non-wetting region which contains a high concentration of oxygen[49-51], while the hydrophilic sulfonic acid groups take up water which is needed to facilitate proton conduction. The hydrophobic and the hydrophilic regions are incompatible. This causes the ionic groups to phase separate from the fluorocarbon backbones to an extent allowed for by the flexibility of polymeric structure. This results in an ion-clustered morphology[48]. Studies of Nafion structure by x-ray diffraction[52] and neutron scattering[53] confirms the existence of inverted micelle type structure with interconnected ionic clusters. When the membrane is hydrated, ionic clusters swell creating more extensive pathways for proton conduction. To date, the exact morphology change during hydration is not yet completely understood[54].

For fuel cell applications, the membrane materials must satisfy functional requirements[55-57] which are: (i) high proton conductivity to facilitate electrochemical reactions and minimize internal ohmic loss; (ii) low gas permeability to prevent cross-over of reactant gases which reduces columbic efficiency; (iii) sufficient mechanical strength and dimensional stability to achieve good sealing and stable performance; (iv) good water retention to maintain uniform water content and minimize dehydration; (v) high thermal, chemical and electrochemical stability under fuel cell environment (high resistance to oxidation, reduction, hydrolysis, and thermal cycles) to provide sufficient operating life-time; and (vi) surface properties that allows good bonding to catalyst particles.

There are many classes of proton exchange membranes developed for PEMFC. Based on the chemical structure, the membranes can be classified[55] as: perfluorinated polymers such as Nafion® developed by DuPont, Flemion® by Asahi Glass Co. and Aciplex® by Asahi Chemical; partially fluorinated polymers such as poly(trifluorostyrene sulfonic acid)[49,58,59] and radiation grafted poly(ethylene tetrafluoroethylene sulfonic acid)[60-63]; and (iii) non-fluorinated polymers such as poly(styrene sulfonic acid)[64,65], sulfonated poly(oxy-1,4-pheylenecarbonyl-1,4-phenylene) (sulfonated PEEK)[66-69].

Poly(styrene sulfonic acid)[70] and the analogous polymers such as phenol sulfonic acid[71] and poly(trifluorostyrene sulfonic acid)[72] (all are non-fluorinated polymers) were the first membranes for PEMFCs used in Gemini space missions in 1960s. Because these polymers are non-cross linked, they had low mechanical strength, and high permeability of gases (poor separation ability)[13]. As a result, the performance (< 100 mW cm^{-2} [13]) and life-time (< 1000 hours) were limited. Rapid membrane degradation was caused by radicals produced from decomposition of H_2O_2, attacking the weak benzylic C-H bonds in the polymeric structure [16].

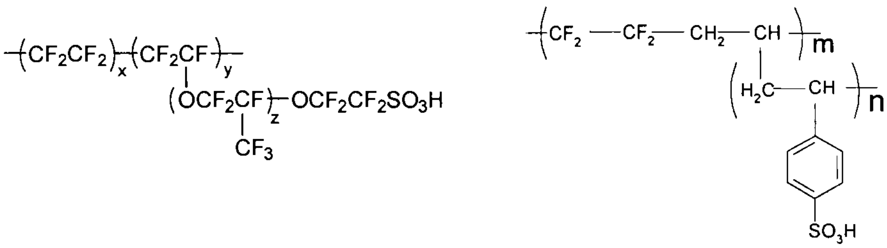

Nafion

Poly(ethylene tetrafluoroethylene sulfonic acid)

Figure 1.8: The general chemical structure of Nafion (x = 6 – 10 and y = z = 1 [73]) and poly(ethylene tetrafluoroethylene sulfonic acid) [63].

The introduction of perfluorosulfonic acid Nafion® membranes (DuPont) in 1966 was an important breakthrough for improving life-time and performance. The general formula for Nafion membranes is shown in Figure 1.8. The chemical structure of Nafion offers two obvious advantages. The first is related to the electronegativity effect due presence of fluorine atoms bonded to the same carbon atom as the SO_3H group. This significantly stabilizes SO_3^- group when deprotonated and therefore, makes SO_3H a super-acid, i.e. similar to the trifluoromethane sulfonic acid. Consequently, the proton conductivity (~70 mS cm^{-1} when fully hydrated and 25 ^{o}C) is sufficiently high enough for many applications. The second advantage is the highly stable C-F bonds, which resists chemical attack and improves life-time (> 60,000 hours). Among the three classes of proton exchange membranes, Nafion® (DuPont) perfluorinated membranes has been the most extensively studied and therefore regarded as "industry standard" membrane for PEMFCs [74].

Novel membranes are continually being developed. From an engineering viewpoint, performance improvements and cost reduction are the primary objectives facilitating commercialization of PEMFCs. In order to push the frontier of engineering, a fundamental study of novel membranes, whose microstructure and physicochemical properties can be controlled by synthesis, is important because it allows systematic understanding of complex relationships between chemical structure, morphology, physicochemical properties, and electrochemical kinetics.

One such class of novel membrane is the partially-fluorinated radiation grafted polymers[16,62,65,75-78], obtained by radiation-induced polymerization of styrene monomer onto commercial membranes, such as fluorinated ethylene propylene (FEP), poly(vinylidene fluoride) (PVDF) and ethylene tetrafluoroethylene (ETFE), with subsequent sulfonation of polystyrene. Several radiation-grafted membranes have been produced[63,78-80], and characterized[75,77,81], and a few have been evaluated in PEMFCs[16,62,65,76]. In this study, a series of tetrafluoroethylene-g-polystyrene sulfonic acid (ETFE-g-PSSA) membranes (Figure 1.8) are used to provide a systematic variation of the membrane's physicochemical property. The relation between chemical structure and physicochemical properties of ETFE-g-PSSA are introduced in the sub-section below.

1.5.1 Influence of Membrane's IEC on Electrochemical Kinetics of ORR.

Proton exchange membranes are characterized by ion exchange capacity (IEC / mmol g^{-1}), which is defined by number of moles of SO_3^- ($n_{SO_3^-}$) per unit mass of dry polymer (m_{dry}).

$$IEC = \frac{n_{SO_3^-}}{m_{dry}} \tag{16}$$

For a given class of membrane, the IEC is directly proportional to its water content (percentage ratio of volume of water to volume of wet membrane), the ratio of H_2O to SO_3^- (known as λ value) and its proton conductivity[49,75]. For a series of radiation grafted membranes, systematic variation of IEC can be achieved by controlling the extent of grafting of polystyrene and the extent of sulfonation[63]. Essentially, the SO_3^- concentration in the polymer is controlled.

Recently, the influence of the membrane's IEC on the electrochemical kinetics of ORR for various radiation grafted membranes[49-51,75,81,82] has been investigated using Pt-microelectrode system[49-51], which provides a well defined Pt / membrane interface under controlled operating conditions. These studies have found that for a given class of membrane, those with lower IEC contain less water, are more hydrophobic, dissolve more O_2, and enhance ORR in the kinetically controlled region. In contrast, they have lower rate of O_2 diffusion because diffusion through polymer (10^{-7} cm^2 s^{-1} in PTFE) is much slower than through water (10^{-5} cm^2 s^{-1}), and consequently they exhibit a lower mass transport limited current. These studies provide a clear indication that in addition to providing the primary functional requirement of transporting protons, the nature of proton conducting membrane affects the electrochemical kinetics of ORR.

In a recent study[62], a performance comparison between fuel cells containing ETFE-g-PSSA membranes (IEC of 0.7 and 2.2 mmol g^{-1}) and Nafion (0.9 mmol g^{-1}) has been reported. Using the same gas diffusion electrode and fabrication process for the MEAs, it was observed that increasing the IEC, increases fuel cell performance. With comparable thickness, the MEA containing Nafion showed similar performance to the MEA containing high IEC ETFE-g-PSSA membrane despite having much lower IEC and lower proton conductivity. Some other factors were likely to influence the fuel cell electrochemical reactions.

The anomalously low performance of ETFE-g-PSSA membrane was not fully understood. The influence of membrane's IEC on the fuel cell electrochemical reactions requires further investigation, and this is addressed in this research.

1.6 Objectives:

The relationship between the chemical structure, the membrane's IEC, proton conductivity and other physicochemical properties have been previously studied[49-51,58,59,82-85]. An understanding of these relationships provides the ability to control the physicochemical properties by varying the chemical structure of the polymer. For fuel cell applications, the next logical question is how the physicochemical properties of the membrane affect fuel cell performance. Reports investigating such relationships are scarce[62,77,86]. A good understanding of the role of the membrane's IEC on fuel cell performance has not yet been addressed.

The goal of this research is to provide better understanding of the influence of membrane's ion exchange capacity on the electrochemical reactions of PEMFC. The IEC is chosen as the variable function because it directly influences water content, proton conductivity and mass transport properties of the membrane.

1.6.1 Technical Approach

A series of radiation-grafted tetrafluoroethylene-g-polystyrene sulfonic acid (ETFE-g-PSSA) membranes are employed to provide a systematic variation of membrane's IEC. The membranes were produced and supplied by Cranfield

University (U.K.). The composition of the gas diffusion electrodes is kept constant throughout the investigations. However, in order to fully analyze experimental results, complete characterization of GDEs and control of the fabrication method (the two critical factors controlling the electrode performance) must be achieved. Commercial GDEs are based on proprietary compositions and fabrication techniques, which are often not revealed. For this reason, a methodology to fabricate GDEs was developed in this laboratory. Operating conditions are kept at ambient temperature and pressure. This is closely related to targeted mobile applications for this class of membrane.

Chapter 2 describes the agglomerate model for the PEMFC cathode and is based on co-authored published papers[87,88]. In order to extract relevant mass transport parameters in the cathode, the agglomerate model was adapted from previously published studies by Perry et. al.[89] and Jaouen et. al.[90]. The mathematical modeling efforts were carried out in joint-collaboration with Dr. Zhongsheng Liu, Dr. Qianpu Wang and Dr. Datong Song of the Institute for Fuel Cell Innovation, National Research Council, and Professor Michael Eikerling of Simon Fraser University. The model was used to extract mass transport properties of the electrodes, which are affected by the membrane's IEC, when operated under half-fuel cell and fuel cell conditions. It also provided insights into the influence of the transport parameters on the electrochemical kinetics of ORR.

Chapter 3 is a collection of experimental procedures and apparatus setups found throughout this research. Congregating these aspects as a stand-alone chapter allows details to be described at length without distracting from the context of research topics. It also minimizes repetitions of the experimental descriptions in Chapter 4 and Chapter 5.

Chapter 4 is based on a published paper[61] that describes the role of the membrane's IEC on the electrochemical ORR at the cathode under a half-fuel cell system. Prior to investigation in actual fuel cell systems, studies were performed in a half-fuel cell electrochemical system, which is designed to closely simulate the cathode under fuel cell conditions but significantly simplifies many complicating parameters associated with fuel cell testing. The apparatus was adapted from published studies[47,91,92] and fabricated by the Machine Shop at Simon Fraser University. Electroanalytical techniques, including electrochemical impedance spectroscopy (EIS), current interruption, cyclic-voltammetry and galvanostatic steady state polarization, were employed. Fitting of the agglomerate model to the experimental results provided insight into the mass transport of O_2 in the catalyst layer. This was used to confirm the interpretation of experimental results.

Chapter 5 describes the parallel analog study to Chapter 4 but the influence of membrane's IEC is studied under operating fuel cell conditions. A concise version of this chapter has been submitted for publication[93]. The experimental results obtained under half-fuel cell and fuel cell conditions were compared. Insights into the mode of transport of oxygen in the cathode catalyst layer are revealed. The intrinsic differences between the two systems are discussed.

Chapter 2 : Modelling of the Cathode Catalyst Layer

Despite significant development in the PEMFC in the past decade, the cathode remains the largest source of energy loss. In order to improve ORR and Pt utilization, understanding of the relation between structural characteristics and performance is important. Within the scope of this thesis, modelling efforts were used to understand the influence of membrane on the ORR. This chapter provides an overview of the agglomerate model for the cathode. In addition to providing the mathematical description of the agglomerate model, polarization curves were computed in order to gain an insight into the influence of mass transport parameters on the cathode performance.

2.1 Brief Introduction

The structural features within a GDE influence transport of reactant. In the catalyst layer, carbon grains (20 – 40 nm) form agglomerates (200 – 300 nm). According to porosimetry measurements[94], a bimodal pore size distribution exists within the porous structure. Micro- and mesopores (< 40 nm) exist inside the agglomerates of carbon particles. Macropores (40 – 200 nm) constitute the inter-agglomerate void spaces. The relative pore volume of the two types of pores is determined by (i) the type of carbon, (ii) the contents of the impregnated Nafion and PTFE, and, to some extent, (iii) the preparation method. Transport of O_2 to the catalytic sites is affected by the structure of pores. Contributions from Knudsen flow, viscous flow and molecular diffusion constitute an effective diffusion coefficient, which influences the ORR. In the micro- and the mesopores, Knudsen diffusion would likely be the prevailing mechanism. On the other hand, transport in the macropores would favour a molecular diffusion mechanism. From the fuel cell operation viewpoint, water management affects the relative pore volumes and the gas porosity of the catalyst layer, which in-turn influences the ORR performance. An increase in water content within the catalyst layer is likely to reduce the gas spaces causing the contribution of gaseous phase molecular diffusion to decrease. Consequently, the effective diffusion coefficient is decreased.

A cathode model should be able to describe the structure as well as the physical and the electrochemical processes occurring therein. There are three main approaches to describe the cathode: (i) the homogeneous, (ii) the thin film, and (iii) the agglomerate models. In the homogeneous model[95-98], the catalyst layer is treated as a homogeneous medium, whose performance is characterized by an effective diffusion constant for O_2, a specific proton conductivity and parameters describing interfacial charge transfer processes. Effects of the electrode structure, i.e. porosity and Nafion content, are embedded within these parameters and they may not explicitly be accounted for in the model. In the film model[99], the electrode is assumed to contain gas pores and the catalyst particles are covered by a thin polymer film. In the agglomerate model[46,89,96,100], the catalyst layer is assumed to consist of both spherical agglomerates and gas-pore network. A homogeneous mixture of Pt/C and Nafion form agglomerates. This model can be viewed as a discretized homogeneous model, which may closely describe the structure of the catalyst layer. In this research, the agglomerate model is a taken as a starting approach towards understanding the influence of membrane on the electrochemical ORR in the catalyst layer.

2.2 Agglomerate Model for PEMFC Cathode

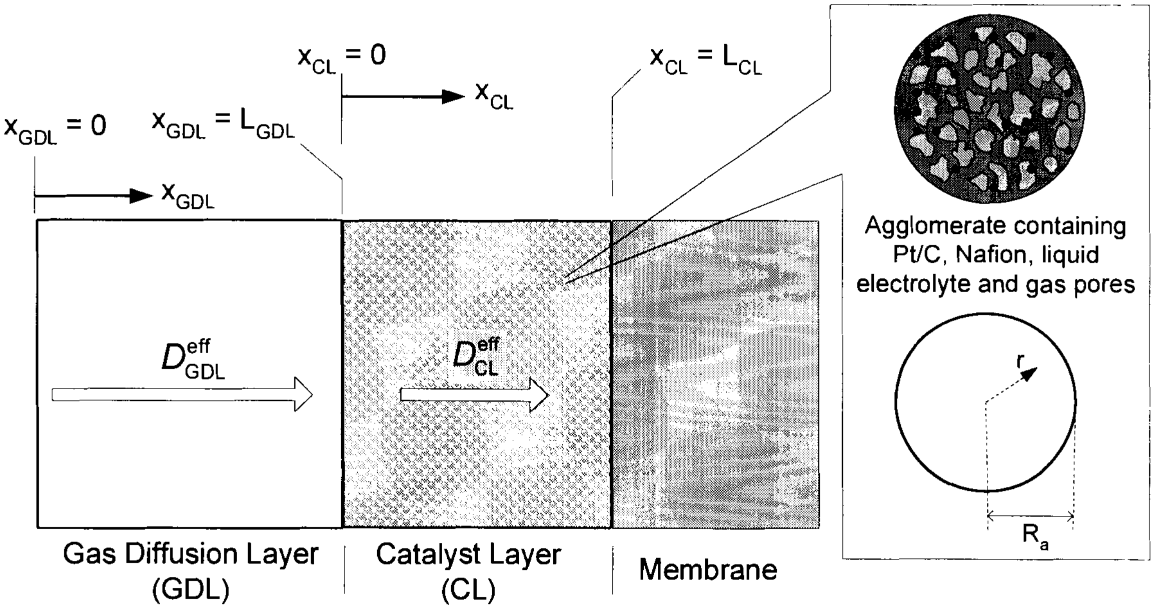

Figure 2.1: Schematic diagram of the agglomerate model for cathode.

The agglomerate model for cathode is adapted from the flooded-agglomerate liquid electrolyte model described by Perry et al [89] and Jaouen et al. [100]. Figure 2.1 shows a schematic diagram of the agglomerate model. In the catalyst layer, Pt/C catalyst and Nafion form agglomerates[94]. For the purpose of modelling the agglomerates in the catalyst layer are assumed spherical with a radius (R_a) and consisting of a homogeneous mixture of Pt/C, impregnated Nafion, liquid water and gas space. Compositions, electrochemical activities and operating conditions are assumed constant at a given thickness: the model is one–dimensional; and isothermal conditions are assumed.

2.2.1 *In the Gas Diffusion Layer:*

Transport of oxygen within the GDL is assumed to occur via diffusion only. A uniform molar flux of oxygen (N_O) is assumed, since there is neither production nor consumption. N_O, which is related to the total current density produced in the catalyst layer (i) (equation 17), is assumed to be proportional to oxygen concentration gradient in the GDL according to Fick's Law (equation 18). The constant of proportionality, $D_{GDL}{}^{eff}$, is the effective diffusion coefficient in GDL.

$$N_{\mathrm{O}} = \frac{i}{4F} \tag{17}$$

$$\frac{dc_{\mathrm{O},g}}{dx_{GDL}} = -\frac{N_{\mathrm{O}}}{D_{\mathrm{GDL}}^{\mathrm{eff}}} = -\frac{i}{4FD_{\mathrm{GDL}}^{\mathrm{eff}}} \tag{18}$$

Equation (18) is used to derive the key parameter, which is the concentration of oxygen at the GDL / catalyst layer interface (c^*). There are two boundary conditions employed; the concentration of oxygen ($c_{O,g}$) entering the GDL at the GDL / flow field channel interface ($X_{GDL} = 0$) is approximated by the ideal gas law (equation 19) and $c_{O,g}$ at the GDL / catalyst layer interface ($x_{GDL}= L_{GDL}$) is defined as c^* (equation 20).

$$x_{\mathrm{GDL}} = 0, \quad c_{\mathrm{O,g}} = \frac{P_{\mathrm{O}}}{RT} \tag{19}$$

$$x_{GDL} = L_{GDL}, \quad c_{O,g} = c^* \tag{20}$$

Solving the above equation, the concentration of O_2 entering the catalyst layer is

$$c_{\mathrm{O,g}}(x_{\mathrm{GDL}} = L^{+}_{\mathrm{GDL}}) = \frac{P_{\mathrm{O}}}{RT} - \frac{i}{4FD^{\mathrm{eff}}_{\mathrm{GDL}}} L_{\mathrm{GDL}} = c^* \tag{21}$$

2.2.2 *In the Agglomerate*

At the agglomerate surface, the gaseous oxygen in the catalyst layer dissolves in the electrolyte phase, diffuses to the reactive sites and undergoes oxygen reduction reaction. The dissolution process is considered to be a fast process. The local concentration of oxygen in the electrolyte (c_0^s) is assumed to be proportional to the gas-phase oxygen concentration ($c_{O,g}$) in the same local volume element according to Henry's law.

$$c_{\mathrm{O}}^{\mathrm{s}} = Hc_{\mathrm{O,g}} \tag{22}$$

The electrical conductivity within individual agglomerate is assumed high such that there is no ohmic loss (uniform potential). The rate of ORR (R_{orr}) is related to the effective O_2 diffusion coefficient in the agglomerate (D_a^{eff}), the distance from the agglomerate centre (r) and the concentration of dissolved O_2 ($c_{O,a}$) and is given by the expression for spherical diffusion[101]

$$D_{\mathrm{a}}^{\mathrm{eff}}\frac{1}{r^2}\frac{\mathrm{d}}{\mathrm{d}r}\left(r^2\frac{\mathrm{d}c_{\mathrm{O,a}}}{\mathrm{d}r}\right)=-R_{\mathrm{orr}} \tag{23}$$

R_{orr} can be related to the current density produced in the agglomerate (i_{a}) by Tafel equation[11] $-R_{orr}=A_a\frac{i_a}{nF}=A_a\frac{i_0}{nF}(\frac{c_{O,a}}{c_O^{ref}})\exp(\frac{\alpha_r F}{RT}\eta)$ (24)

where R, T, n and F are the ideal gas constant, temperature, number of electron transferred and the Faraday's constant, respectively. A_{a} and i_0 are the catalyst area per unit volume and the exchange current density, respectively. The reference concentration of O_2 ($c_{\mathrm{o}}^{\mathrm{ref}}$) is defined as the concentration of O_2 at the surface of an agglomerate in equilibrium with 1 atm. pressure at open circuit potential. $c_{\mathrm{o}}^{\mathrm{ref}}$ is independent of the location in the catalyst layer (x-direction).

$D_{\mathrm{a}}^{\mathrm{eff}}$ (equation 23) can be estimated from the O_2 diffusion coefficient in Nafion (D_{N}), agglomerate porosity (ε_{a}) and tortuosity factor (τ)

$$D_a^{eff}=D_N\frac{\varepsilon_a}{\tau} \tag{25}$$

In order to solve equation (23), two boundary conditions are employed which express the condition of zero O_2 flux at the centre of the agglomerate (equation 26) and the solubility of O_2 at the agglomerate surface (c_0^{s}) (equation 27):

$$r=0,\quad \frac{dc_O}{dr}=0 \tag{26}$$

$$r=R_a,\quad c_O=c_O^s \tag{27}$$

The analytical solution is given by[101]

$$c_{O,a} = c_O^s \frac{R_a}{r} \frac{\sinh(\phi r)}{\sinh(\phi R_a)} \tag{28}$$

where the dimensionless parameter ϕRa is commonly known as the Thiele modulus representing the ratio of surface reaction rate to internal diffusion rate of O_2 within the agglomerate. When the Thiele modulus is large, the reaction occurs mainly in the vicinity of agglomerate spherical surface.

$$\phi R_a = \sqrt{\frac{i_0}{nFD_a^{eff} c_0^{ref}}} R_a \exp(\frac{\alpha_r F}{2RT}\eta) \tag{29}$$

The expression for the current density produced in the agglomerate is obtained by substituting equation (28) into (24).

$$i_a = -4\pi nFR_a D_a^{eff} c_O^s \left[\phi R_a \coth(\phi R_a) - 1\right] \tag{30}$$

2.2.3 In the Catalyst Layer:

Oxygen is assumed to diffuse through the catalyst layer according to Fick's law

$$\frac{dc_{O,g}(x)}{dx_{CL}} = -\frac{N_O(x)}{D_{CL}^{eff}} \tag{31}$$

Since oxygen is consumed as it diffuses along the catalyst layer thickness (x-direction), $c_{O,g}$ and the flux (N_O) are position-dependent; i.e. $c_{O,g}(x)$ and $N_O(x)$. The latter is expressed as

$$N_O(x_{CL}) = \frac{j_p(x_{CL}) - i}{4F} \tag{32}$$

The local protonic current density, $j_p(x)$, is proportional to the local overpotential gradient, $d\eta(x)$ / dx_{CL}, and the migration of protons in the electrolyte phase can be described by Ohm's law

$$\frac{d\eta(x_{CL})}{dx_{CL}} = \frac{j_p(x_{CL})}{\sigma^{eff}} \tag{33}$$

σ^{eff} is the effective proton conductivity of the layer.

The local electrode potential, $E(x_{CL})$, can be calculated from the local electrode potential (metal phase, Pt/C), $\phi_m(x_{CL})$ and the electrolyte potential, $\phi_s(x_{CL})$.

$$E(x_{CL}) = \phi_m - \phi_s \tag{34}$$

The potential applied to the cathode, E_c, is fixed relative to the electrolyte potential at the catalyst layer/membrane interface[102], x_{CL} = L_{CL}, and the resulting boundary conditions are

$$x_{CL} = L_{CL}, \quad \phi_m = E_c \tag{35}$$

$$x_{CL} = 0, \quad \phi_s = 0 \tag{36}$$

The density of agglomerates (ρ_a) in the catalyst layer can be calculated by equation (37), and is used to derive the protonic mass balance (equation 38

$$\rho_a = \frac{1-\varepsilon_c}{\frac{4}{3}\pi R_a^3} \tag{37}$$

$$\frac{dj_p}{dx_{CL}} = \rho_a i_a \tag{38}$$

Combining the above equations yields

$$4FD_{\mathrm{CL}}^{\mathrm{eff}}\frac{\mathrm{d}^2c_{\mathrm{Og}}}{\mathrm{d}x_{\mathrm{CL}}{}^2}=-\rho_{\mathrm{a}}i_{\mathrm{a}} \tag{39}$$

Using the boundary conditions describing zero protonic flux at the GDL / catalyst layer interface (x_{CL} = 0) and the maximum protonic flux at catalyst layer / membrane interface, the solution of the non-linear differential equation is obtained numerically.

$$x_{CL}=0,\quad j_{\mathrm{p}}=0,\quad c_{\mathrm{O},g}=c^{*} \tag{40}$$

$$x_{\mathrm{CL}}=L,\quad j_{\mathrm{p}}=i,\quad \frac{\mathrm{d}c_{\mathrm{Og}}}{\mathrm{d}x_{\mathrm{CL}}}=0 \tag{41}$$

2.3 Obtaining Polarization Curves from the Model

In order to obtain a profile of current density generated in the catalyst layer (i) as a function of the electrode potential (E_c), the governing equations (32), (33) and (38), were solved using the boundary conditions described in equations (19), (35), (40) and (41). The fourth order Runge-Kutta numerical method, an iterative one-dimensional finite difference scheme, available in MATLAB software was employed. The electrode was divided into N grid points in the x-direction. For a given electrode potential at the membrane/catalyst layer interface (x_{CL} = L_{CL}) the values of $E(x_{CL})$, $c_{O,g}(x_{CL})$ and $j_p(x_{CL})$ were computed at each grid point. The iterative procedure involves the following steps:

1. The local electrode potential, $E(x)$, at each grid point was calculated from equation (33) using a given set of initial guess values.

2. The local protonic current density, $j_p(x_{CL})$, was calculated from equation (38).
3. The local oxygen concentration, $c_{O,g}(x_{CL})$, at each point was calculated by equation (39).

Steps (1) to (3) were repeated until convergence in the values of $j_p(x_{CL})$, $E(x_{CL})$ and $c_{O,g}(x_{CL})$ was achieved. The convergence was defined as a normalized local change in either $E(y)$, $c_{O,g}(y)$ or $j_p(y)$ between adjacent iterations (y_1 and y_2), and was set at 0.001 (or 0.1 %).

$$Convergence = \frac{|y_2 - y_1|}{|y_1|} \tag{42}$$

Lowering the convergence values to 1.0×10^{-4} did not change the extracted E, $c_{O,g}$ or j_p values. The number of grid, N, was set at 5. Increasing N to 50 has no significant effect on the computed values. The polarization curves for the electrode potential between 1.23 and 0.40 V were generated by taking $i = j_p$ and $E_c = E$, at the membrane/catalyst layer interface ($x_{CL} = L_{CL}$).

2.4 Simulation of Polarization Curves

Wthin the scope of this thesis, the influence of mass transport parameters (D_{GDL}^{eff}, D_{CL}^{eff}, c_o^{ref} and D_a^{ref}) on the catalyst layer performance is important (as will be discussed in Chapter 4 and Chapter 5). In addition to providing the mathematical description of the agglomerate model, polarization curves were computed in order to gain an insight into how the individual parameter affects the cathode performance. The base-case parameters (Table 2.1) were chosen from the values typically found in the literature for a cathode operating under room temperature and ambient pressure. For the purpose of illustrating the dependence of the cathode performance on $D_{\mathrm{GDL}}^{\mathrm{eff}}$ and $D_{\mathrm{CL}}^{\mathrm{eff}}$, the values were varied from 10^{-1} (bulk diffusion coefficient in gaseous phase) to 10^{-6} (bulk diffusion coefficient in liquid phase) $\mathrm{cm}^2\ \mathrm{s}^{-1}$, while other parameters were kept constant at the base-case values. For $D_{\mathrm{a}}^{\mathrm{ref}}$, the values were varied by $\pm$ 1 order of magnitude from its approximated value of ~ 10^{-6} $\mathrm{cm}^2\ \mathrm{s}^{-1}$. The agglomerate surface concentration of O_2 at the equilibrium to the gaseous phase O_2 in the catalyst layer, $c_{\mathrm{o}}^{\mathrm{ref}}$, was varied from 0.1 to 10 mmol l^{-1} (a typically range of variation for proton exchange membranes[82]). The simulated polarization curves are presented below.

Table 2.1: Base case parameters used for simulating polarization curves to illustrate their dependency on mass transport parameters

Parameter (Unit)	Value
Temperature, T (K)	298
Pressure of O_2, P (Pa)	1.01×10^5
Charge transfer coefficient of ORR, α_r	0.58
Agglomerate Radius, R_a (μm)	0.1
Thickness of catalyst Layer, L (μm)	30
Thickness of GDL, L_{GDL} (μm)	350
Proton conductivity of Membrane, σ (S cm^{-1})	0.08
Effective proton conductivity in CL, σ^{eff}_{CL} (S cm^{-1})	0.009
Exchange current density, i_0 (A cm^{-2})	1.0×10^{-7}
Reference concentration of O_2, c_O^{ref} (mmol L^{-1})	1.0
D_{CL}^{eff} (cm^2 s^{-1})	1.0×10^{-5}
D_{GDL}^{eff} (cm^2 s^{-1})	1.0×10^{-3}
Henry's constant, H	30

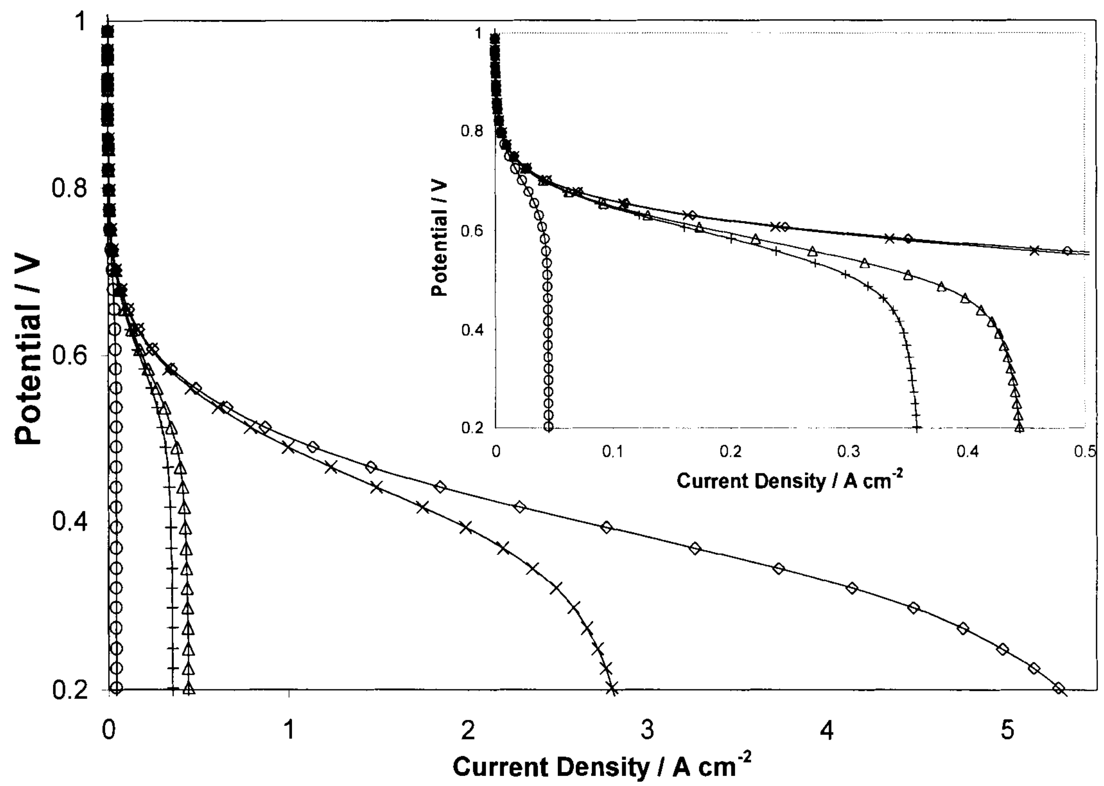

Figure 2.2: Dependence of cathode performance on the effective diffusion coefficient in the gas diffusion layer (D_{GDL}^{eff}); 0.1 (-◇-), 1 x 10^{-2} (-X-), 1 x 10^{-3} (-Δ-), 8 x 10^{-4} (-+-) and 1 x 10^{-4} (-0-) cm^2 s^{-1}.

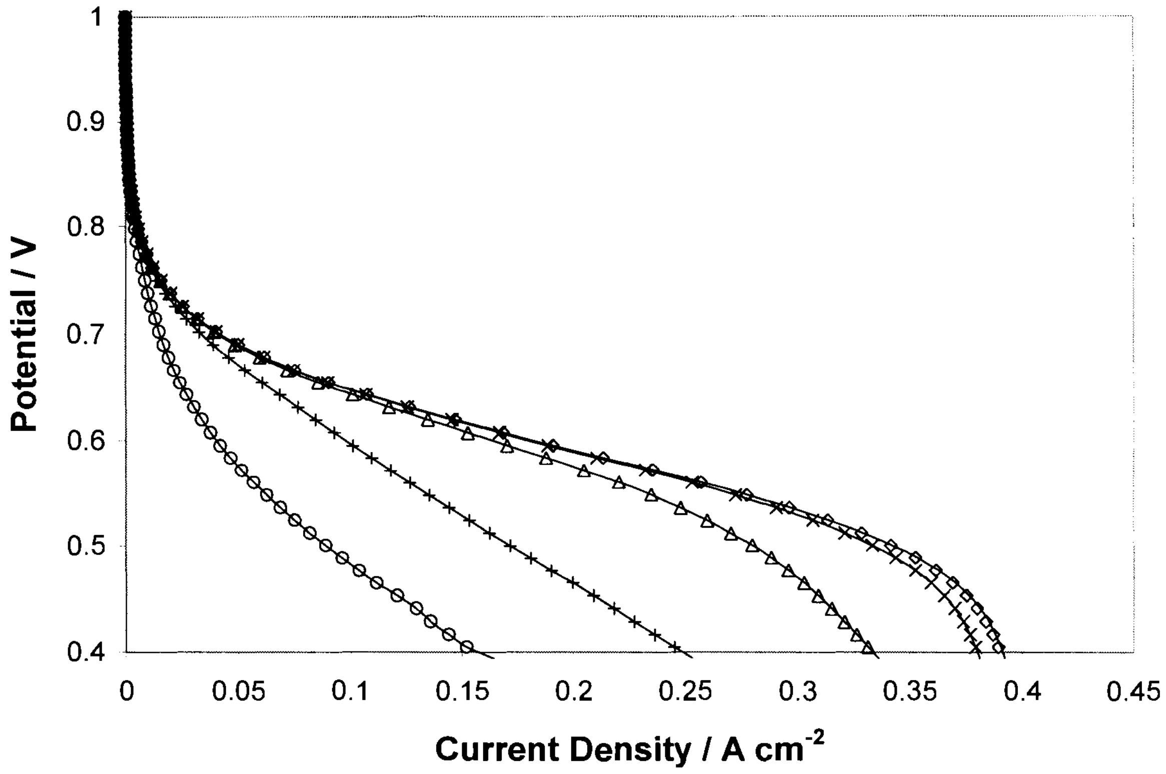

Figure 2.3: Dependence of cathode performance on the effective diffusion coefficient in the catalyst layer (D_{CL}^{eff}); 0.1 (—), 10^{-2} (◇), 10^{-3} (-X-), 10^{-4} (-Δ-), 10^{-5} (-+-) and 10^{-6} (-O-) cm^2 s^{-1}.

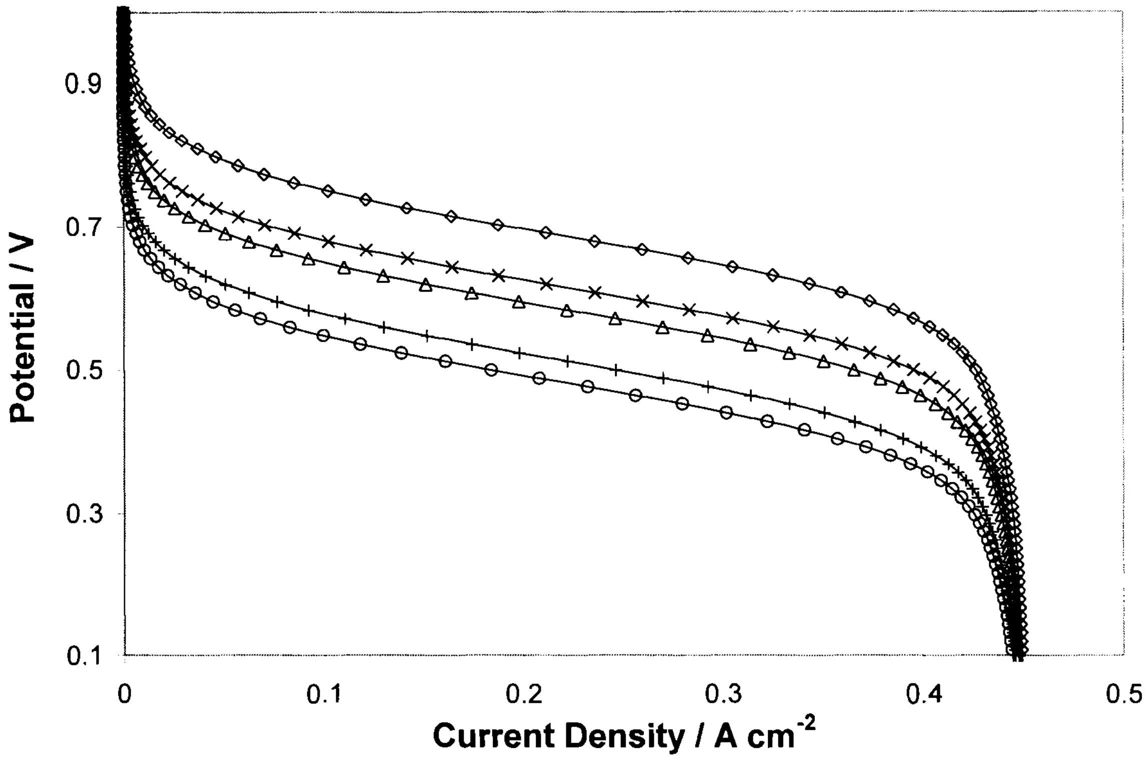

Figure 2.4: Dependence of cathode performance on the equilibrium concentration of oxygen in the catalyst layer (c_o^{ref}); 10 (-◊-), 5.0 (-X-), 1.0 (-Δ-), 0.5 (-+-) and 0.1 (-0-) mmol l^{-1}.

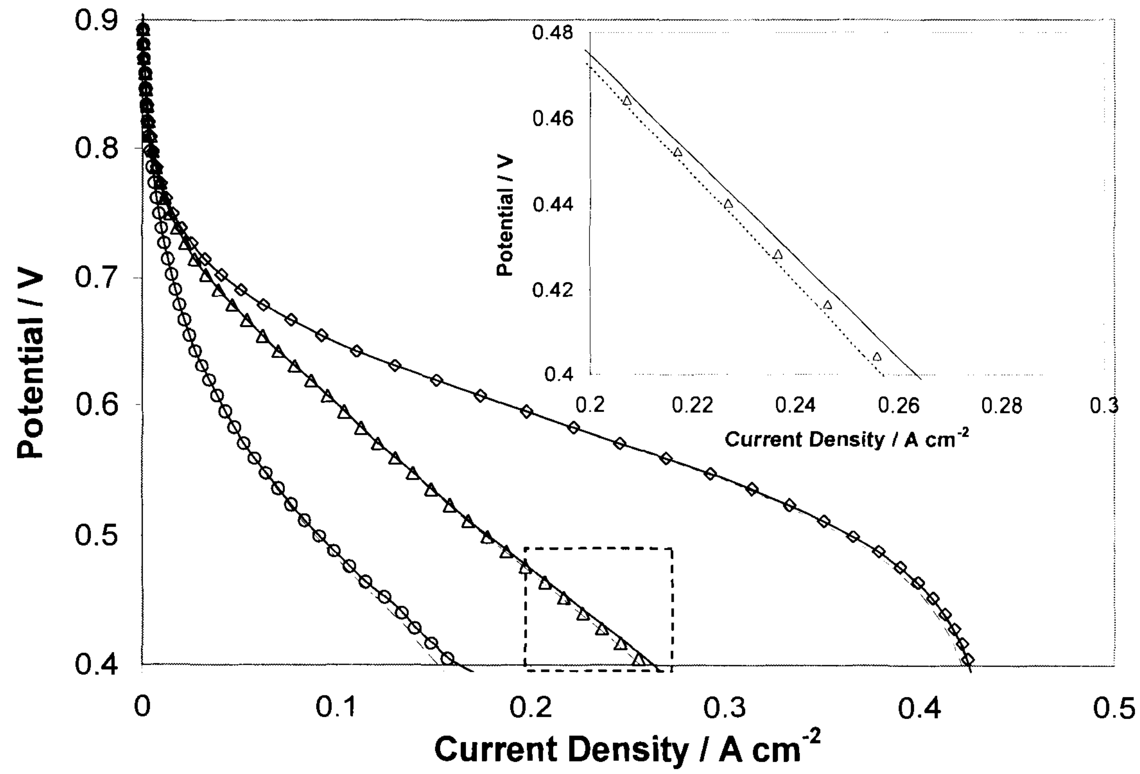

Figure 2.5: Dependence of cathode performance on the effective diffusion coefficient in an agglomerate (D_a^{ref}) when D_{CL}^{eff} is 1 x 10^{-6} (O), 1 x 10^{-5} (Δ), and 1 x 10^{-3} (◊) cm^2 s^{-1}. D_a^{ref} = 1 x 10^{-7} (---), 1 x 10^{-6} (O, Δ and ◊), and 1 x 10^{-5} (—) cm^2 s^{-1}. Inset: expanded plot from the dash square area.

The dependence of the cathode performance on D_{GDL}^{eff}, D_{CL}^{eff}, c_O^{ref} and D_a^{ref} are shown in Figure 2.2 to Figure 2.5, respectively. Within a mass transport controlled region the electrode overpotential is sufficiently high, providing a facile electrochemical conversion rate and therefore, the current density is limited by the rate of reactant supplied to the reactive sites. For a given D_{CL}^{eff}, the limiting current density observed at ~ 0.4 V is strongly affected by D_{GDL}^{eff} (Figure 2.2) – a small increase in D_{GDL}^{eff} yields a significant increase in the limiting current density. Arising from this observation, designing a gas diffusion electrode with

GDL containing hydrophobic/PTFE or well connected macroporous structure in order to improve D_{GDL}^{eff} would allow the electrode to attain higher limiting current density. When D_{GDL}^{eff} is higher than D_{CL}^{eff}, the mass transport limitation occurs predominantly in the catalyst layer. A decrease in D_{CL}^{eff} reduces the electrode performance at moderate (~ 0.7 V) and low (~ 0.4 V) potentials, see Figure 2.3. Comparing Figure 2.2 and Figure 2.3, the electrode performance is more sensitive to a change in D_{GDL}^{eff} than D_{CL}^{eff}. The agglomerate surface oxygen concentration, c_o^{ref}, affects the kinetically controlled regions (Figure 2.4). An increase in c_o^{ref} causes the polarization curve to shift upward along the potential axis, while the gradient of the linear region remains constant. The latter indicates that c_o^{ref} does not affect the Ohmic region. A variation of the effective diffusion coefficient in an agglomerate, D_a^{ref}, by two orders of magnitude (10^{-7} to 10^{-5} cm^2 s^{-1}) shows very small influence on the electrode performance (Figure 2.5 inset). The base-case operating conditions yielded high values of Thiele modulus, which facilitates reaction to occur in the vicinity of agglomerate surface, and thus, the performance is weakly dependent on the diffusion inside the agglomerate. Comparing Figure 2.4 to Figure 2.5 reveals that, for some operating conditions, a development of the impregnated membrane material may be most beneficial by improving its oxygen concentration.

The knowledge of the sensitivity of cathode performance on the individual mass transport parameter may be beneficial for the GDE development. When used as a designing tool, it provides a research direction which focuses on a strategic modification of material properties that could produce the most significant improvement of performance. Outside the scope of this thesis, the agglomerate model was employed to investigate two different design options for the cathode; functionally graded cathode catalyst layer possessing a gradient of Nafion content and a gradient of agglomerate size. These co-authored reports have been published elsewhere[87,103].

Chapter 3 : Materials, Electrodes and Instrumentation

3.1 Membranes

3.1.1 Preparation Overview:

A series of radiation-grafted tetrafluoroethylene-g-polystyrene sulfonic acid membranes (ETFE-g-PSSA) having different ion exchange capacity were employed. These membranes were prepared by J. Horsfall and K. Lovell at Cranfield University, and was published elsewhere[63]. These polymers were prepared by post-irradiation, where styrene was grafted onto ETFE, followed by subsequent sulfonation. A brief description of the membrane preparation is given. An ETFE film (50 μm thick, DuPont) was irradiated by exposing it to cobalt 60 gamma radiation in air at 23 °C with a 30 kGy dosage. This produced a finite number of peroxy radicals on the ETFE. This irradiated film was immersed in a vessel containing a deoxygenated solution of styrene, and heated to 40-60 °C. Upon heating, the peroxy radicals on the ETFE decompose[6] to form reactive radicals on the polymer backbone. These radicals initiate polymerization of

---

[6] Storage of the irradiated polymer at -18 °C for up to 430 days has shown no loss of radical activity

styrene to form grafts. Copolymers with different degrees of grafting were obtained by terminating the polymerization at specific time intervals, by removing the grafted polymer from the vessel and washing with toluene. The grafted polymers were dried at 70 ^{0}C to constant weight. The extent of grafting was quantified by weight after grafting, and is depicted in equation (43),

$$\text{Degree of Grafting [wt.\%]} = \frac{(W_g - W_0)}{W_g} \times 100 \tag{43}$$

where W_0 and W_g are the weight of the film before and after grafting, respectively. In addition to the grafting time, the degree of grafting was controlled by changing the total radiation dose, the styrene concentration, and the grafting temperature.

In order to function as a proton exchange membrane, the grafted copolymers were sulfonated. This was carried out by immersing the copolymer in 5 vol% of chlorosulfonic acid dissolved in dichloromethane for 2 hours at ambient temperature and pressure, after which they were washed in hot de-ionized water and dried in air. A thermal annealing process was performed on the sulfonated graft-copolymers by heating in deionized water at 95 °C for 1 hour and oven dried at 40 °C. This process increased the hydrophilicity of the membrane possibly due to the acidic groups realigning themselves within the polymer structure[63].

3.1.2 Pretreatment of Membranes

All membranes used in this research were boiled in 1.0 M H_2SO_4 for 1 hour, in de-ionized water (Millipore) for 10 minutes and subsequently rinsed and stored in de-ionized water for 24 hours prior to use.

3.1.3 *Measurement of Ion Exchange Capacity*

Ion Exchange Capacity (IEC) of the membranes were measured according to a reported procedure[75]. The pre-treated membranes in their fully protonated form were immersed in 50 ml of NaCl (2.0 M) solution for 2 hours to exchange H^+ in the membrane for Na^+ ions. The solution was titrated with NaOH (0.025 M) to a phenolphthalein end point. Following titration, the membranes were protonated in 0.1 M HCl for 1 hour rinsed with de-ionized water and dried under vacuum at 80 ^{0}C to obtain constant dry weight (m_{dry}). The IEC [mmol g^{-1}] is calculated from m_{dry}, the volume (V_{NaOH}) and concentration (c_{NaOH}) of NaOH as follows:

$$IEC = \frac{V_{NaOH}\ c_{NaOH}}{m_{dry}} \tag{44}$$

3.1.4 *Measurement of Proton Conductivity*

Proton conductivity measurements were performed at 25 ^{0}C using a two Pt electrode in-plane apparatus similar to that described in the published literature[104]. A sample of membrane (1.5 x 1 cm^2) was placed between two parallel Pt-sheet electrodes having a 1 cm gap in a test fixture constructed from PTFE/glass composite (Delrin®, Dupont). The assembly was compressed to minimize membrane/electrode contact resistance and immersed in de-ionized water. The membrane resistance was measured by electrochemical impedance spectroscopy (EIS) using a frequency response analyzer (Solartron 1260, Solarton Analytical Inc.) controlled by Z-plot® data acquisition software (Scribner Associates, Inc). Alternating perturbation potentials having an amplitude of 5 mV was applied to the cell at the frequency range from 20 MHz to 10 Hz, where the amplitude and the phase shift of the resultant current were recorded.

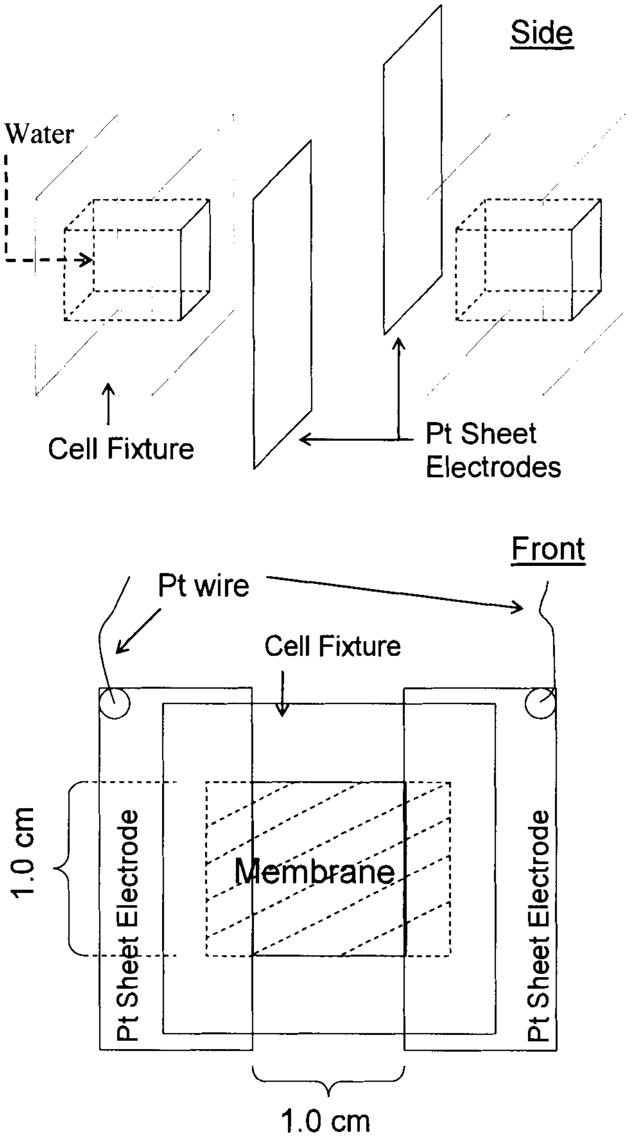

Figure 3.1: Schematic diagram of the apparatus for measuring proton conductivity of membranes: the overall cell assembly (side view) and the measurement dimensions (front view).

According to the theory of electrochemical impedance spectroscopy (EIS)[105], the membrane resistance (R_m) can be extracted from the Nyquist plot (the real impedance against the imaginary impedance) by assuming a simplified equivalent circuit for ionic resistance[106-108] (shown as the inset of Figure 3.2). The values of the contact resistance (R_c) and the geometric capacitance of the membrane (c_m) are dependent on the apparatus arrangement. On the other hand, R_m varies significantly depending on the membrane and its thickness[83]. A simulation of the equivalent circuit produces a theoretical EIS spectrum, as qualitatively shown by the dash line in Figure 3.2.

The proton conductivity of the bulk membrane (σ_b) can be calculated from R_m, the measured thickness (t), the width (w) and the conduction length (l) of the membrane according to Ohm's law

$$\sigma_b = \frac{l}{R_m t w} \tag{45}$$

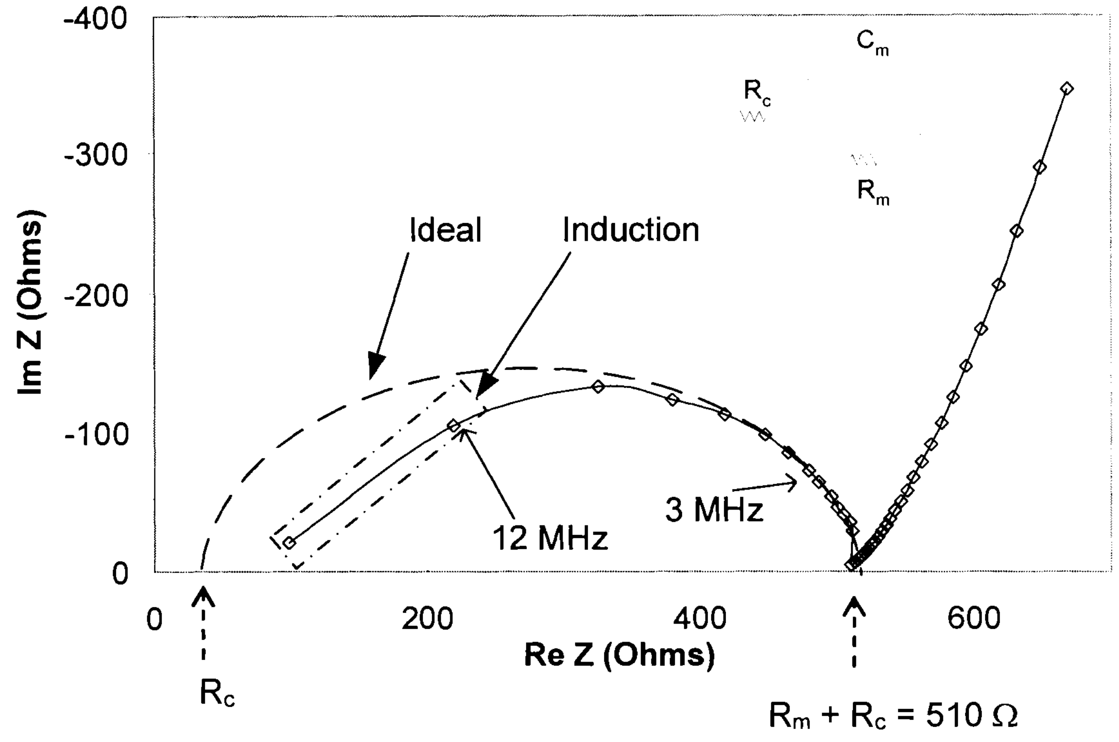

Figure 3.2: A Nyquist plot of Nafion 117 membrane measured at 25 ^{0}C (◊). Inset: the equivalent circuit used to describe high frequency intercepts, the membrane resistance (R_m) and the membrane/Pt sheet contact resistance (R_c). The ideal EIS response derived from the equivalent circuit (---).

Figure 3.2 shows a typical EIS response for proton conducting membranes measured by the conductivity apparatus. A strong deviation from the semi-circle response was observed at high frequencies (> 1 MHz). This type of behaviour has been reported in the literature [109] and was attributed to an interference from induction generated within the connecting cables. Attempts had been made to minimize the induction by using various cable grades and lengths. However, complete elimination was difficult. Consequently, the contact resistance (R_c) could not be directly determined. Nevertheless, the significance of R_c in the apparatus was be evaluated using Nafion 117 as a standard membrane since its conductivity is known to be ~ 0.08 to 0.07 S cm^{-1} when fully hydrated at 25 °C [58,83], R_m for Nafion was calculated from Equation (50) (with measured dimensions of 1.0 mm long x 1.2 mm wide x 198 μm thick) to be between 520 and 590 Ω. This value was close to the high frequency intercept on the real impedance axis ($R_m + R_c = 510\ \Omega$), and provides clear evidence that the impedance data is dominated by the membrane resistance. Therefore, R_c is assumed negligible in this apparatus.

3.2 Gas Diffusion Electrodes

3.2.1 Specification of GDEs

Conventionally, GDEs are specified by three parameters: (i) Pt loading, (ii) wt% Pt-on-C, and (iii) wt% of Nafion impregnated in the catalyst layer. These parameters are defined as

$$\text{Pt loading} = \frac{m_{\text{Pt}}}{m_{\text{Pt}} + m_{\text{C}}} \qquad (46)$$

$$\text{wt\% Pt/C} = \frac{m_{\text{Pt}}}{m_{\text{C}}} \times 100 \qquad (47)$$

$$\text{wt\% Nafion} = \frac{m_{\text{N}}}{m_{\text{Pt}} + m_{\text{C}} + m_{\text{N}}} \times 100 \qquad (48)$$

where m_{Pt}, m_{C} and m_{N} are the mass of Pt, carbon and Nafion, respectively.

3.2.2 Fabrication Procedure:

Two-layered gas diffusion electrodes, containing a gas diffusion layer substrate and a catalyst layer, were prepared using carbon supported Pt (20 wt%

Pt on Vulcan XC-72, ElectroChem Inc.), Nafion solution (5 wt% in water/alcohol, Aldrich) and carbon cloth substrate (type A plain weave, 0.35 mm thick, 10 wt% wet-proofed, ETEK). Electrodes were fabricated in-house using the colloidal dispersion of Nafion approach[94,110]. The Pt/C was dispersed in butyl acetate and homogenized at 50 °C for 30 minutes. A large amount of butyl acetate was added to the Nafion solution until the mixture yielded a pale blue liquid indicating scattered light in the presence of colloids. The Nafion suspension was added drop-wise to the Pt catalyst suspension while stirring. The mixture was stirred for 1 hour. The catalyst ink was brush-painted onto a carbon cloth substrate to obtain a gas diffusion electrode. During successive painting, the deposited ink was heated gently with a heat gun to accelerate evaporation of butyl acetate (boiling point 125 °C). The electrode was dried in an oven at 80 °C overnight to remove traces of the dispersion medium. The surface of the catalyst layer obtained from this procedure was visibly smooth.

3.2.3 Evaluation of Homogeneity of Catalyst Particles Distribution

In order to evaluate the homogeneity of catalyst particles distribution on a GDE, circular buttons (2.1 cm diameter) were cut from various locations and hot-pressed with Nafion membrane at 220 kg cm^{-2} and 150 °C for 90 s forming half-membrane electrode assemblies (HMEAs). Using the half-fuel cell apparatus, cyclic voltammograms in N_2-saturated 1.0 M H_2SO_4 and ORR polarization curves of the HMEAs were compared. Figure 3.3 compares three HMEAs with GDEs cut from various locations of the electrode discussed in Chapter 4 having specification of 0.78 mg Pt cm^{-2} (20 wt% Pt on Vulcan XC-72) and 20 wt% Nafion content. The area under the H-adsorption and desorption curves, for the three batches provided similar electrochemically active surface areas (±5 %). ORR polarization curves of the electrodes in the half-fuel cell apparatus were also similar, with a ±6 % variation in current density. It is noteworthy that when the reproducibility tests were performed using GDEs without forming HMEAs, the catalyst powder surface was not physically protected by a membrane, and was observed to partially dissociate into the electrolyte. The extent of Pt loss was difficult to estimate, and therefore reproducibility tests were performed using HMEAs.

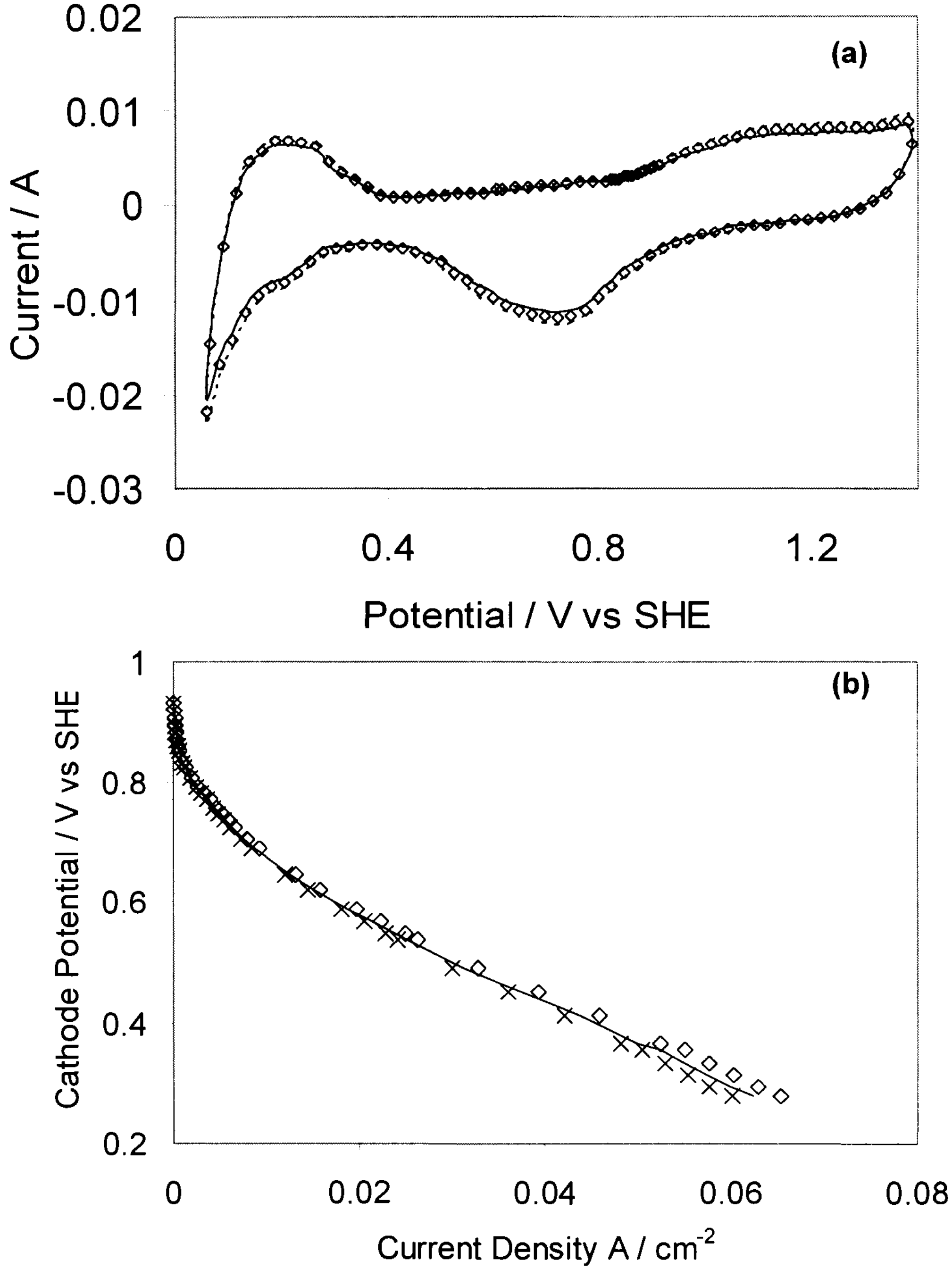

Figure 3.3: (a) Cyclic voltammograms and (b) oxygen reduction polarization curves of three HMEAs containing Nafion 117 and GDEs cut from various locations of the same batch of GDE. Scan rate = 10 mV s^{-1}.

3.3 Half-Fuel Cells

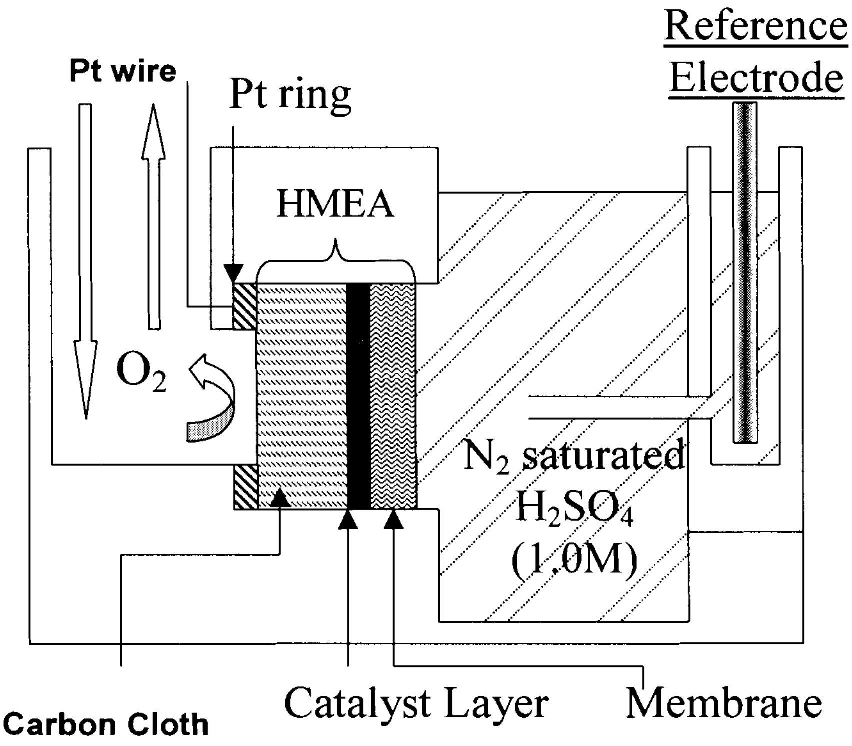

Figure 3.4: Schematic diagram of the half-fuel cell apparatus. Working electrode: the half-membrane electrode assembly (1.76 cm^2). Reference electrode: standard calomel in sat. KCl, Counter electrode: Pt gauze (not shown).

Half-Fuel Cell Setup: The half-fuel cell electrochemical apparatus was constructed from a PTFE / glass composite material (Delrin®, DuPont). The arrangement of the half-fuel cell was adapted from the previously published design[47,92,111,112]. The working electrode, a half-membrane electrode assembly (HMEA), was held vertically in a chamber filled with 1.0 M H_2SO_4. O_2 was supplied to the carbon cloth and the membrane side of the HMEA was exposed to H_2SO_4 (Figure 3.4). During ORR measurements, the flow rate of O_2

was kept constant at 45 ml min^{-1}. A Pt ring provided the electrical contact to the gas diffusion layer of HMEA. A Luggin capillary was positioned approximately 4 ±1 mm from the HMEA. The reference electrode was a saturated KCl Calomel electrode, 0.242 V vs standard hydrogen electrode (SHE). In this thesis, all potentials are reported with respect to SHE. The counter electrode was a large surface area Pt gauze.

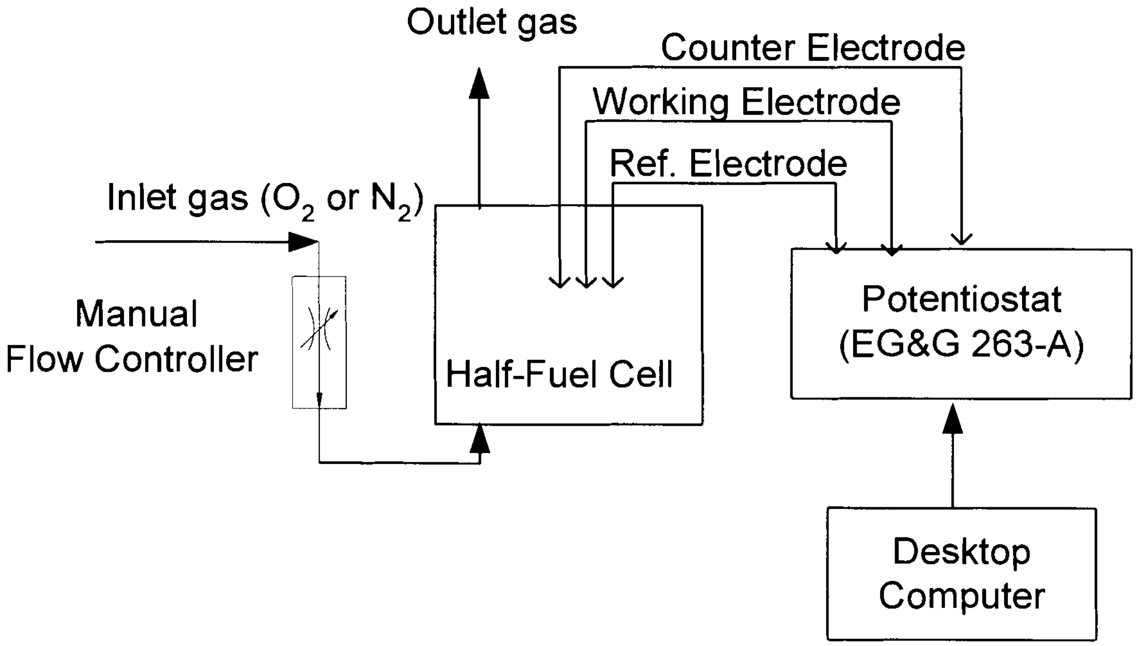

Figure 3.5: Schematic diagram of the half-fuel cell system.

An overview of the half-fuel cell system is shown in Figure 3.5. The flow rate of the inlet gas is controlled by a manual flow controller consisting of a flow meter and a needle valve for flow adjustment. The potential of the working electrode relative to the reference electrode was controlled by a potentiostat (Model 263-A, EG&G) communicating with a personal computer via a GPIB-PCI communication card (IEEE 488-1978, National Instruments). PowerCV (EG&G)

data acquisition software was used to control the potentiostat and to provide a semi-automation capability.

3.4 Fuel Cells

A 5 cm^2 fuel cell with serpentine flow-pattern (ElectroChem. Inc) was employed. A schematic diagram of the fuel cell is shown in Figure 3.6. The flow channels has a 1 mm width and 1 mm depth. The cell temperature was heated by two heating pads located at the back of current collect plates, and cooled by an external fan. Since the active area was surrounded by large graphite block functioning as a heat sink, the heat dissipation was assumed to be rapid and an isothermal condition for the cell was assumed.

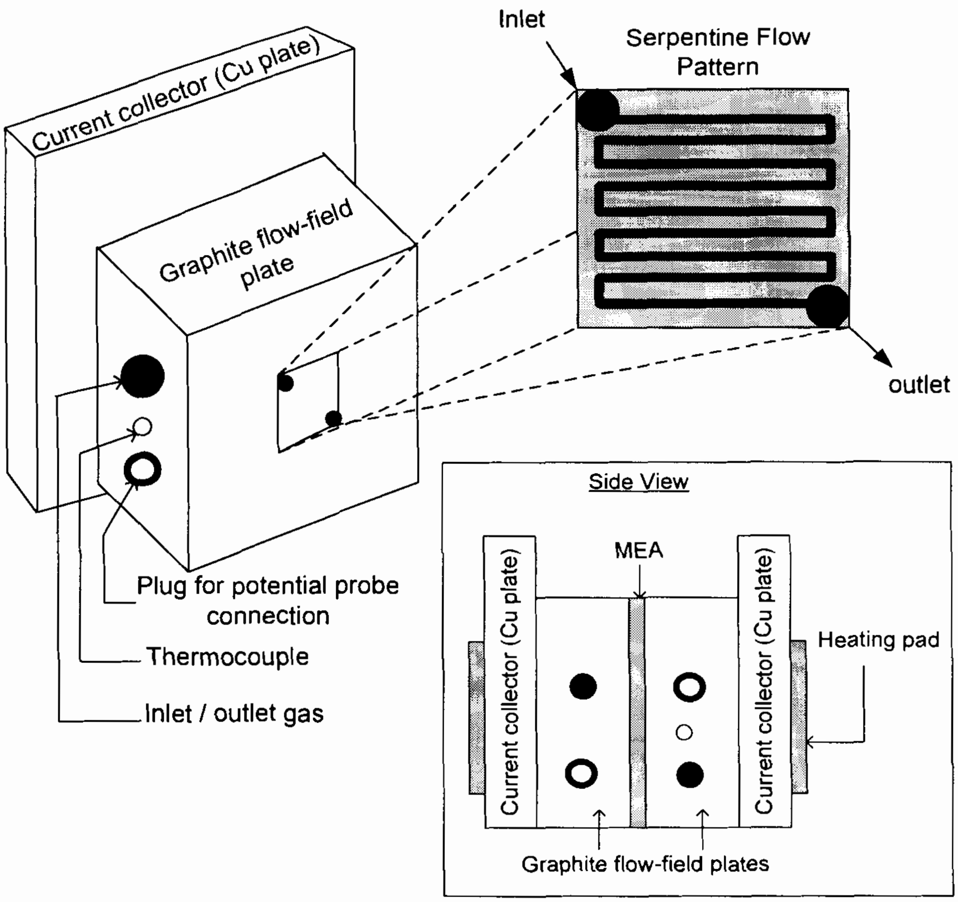

Figure 3.6: Schematic diagram of a fuel cell with serpentine flow pattern.

The fuel cell was connected to a test station consisting of a gas humidification unit (Globetech Inc) and a loadbank electronic controller (Scribner 890B, Scribner Associates Inc.). A simplified diagram of the fuel cell system is illustrated in Figure 3.7. All gases were supplied from the pressurized cylinders. The inlet pressure was reduced to 40 psi., and the flow rates were regulated by two electronically-controlled flow meters. The gases were passed into the humidification bottles before being fed into the cell. The cell temperature, the output current, the electrode potential and the flow rates were controlled by the electronic loadbank, which was driven by FuelCell® data acquisition software

(Scribner Associates Inc). A capability to perform the electrochemical impedance spectroscopy (EIS) was achieved by integrating the loadbank controllers to a frequency response analyzer (FRA) (Solartron 1250, Solartron Analytical). Z-Plot® (Scribner Associates Inc.) data acquisition software was used to control the FRA.

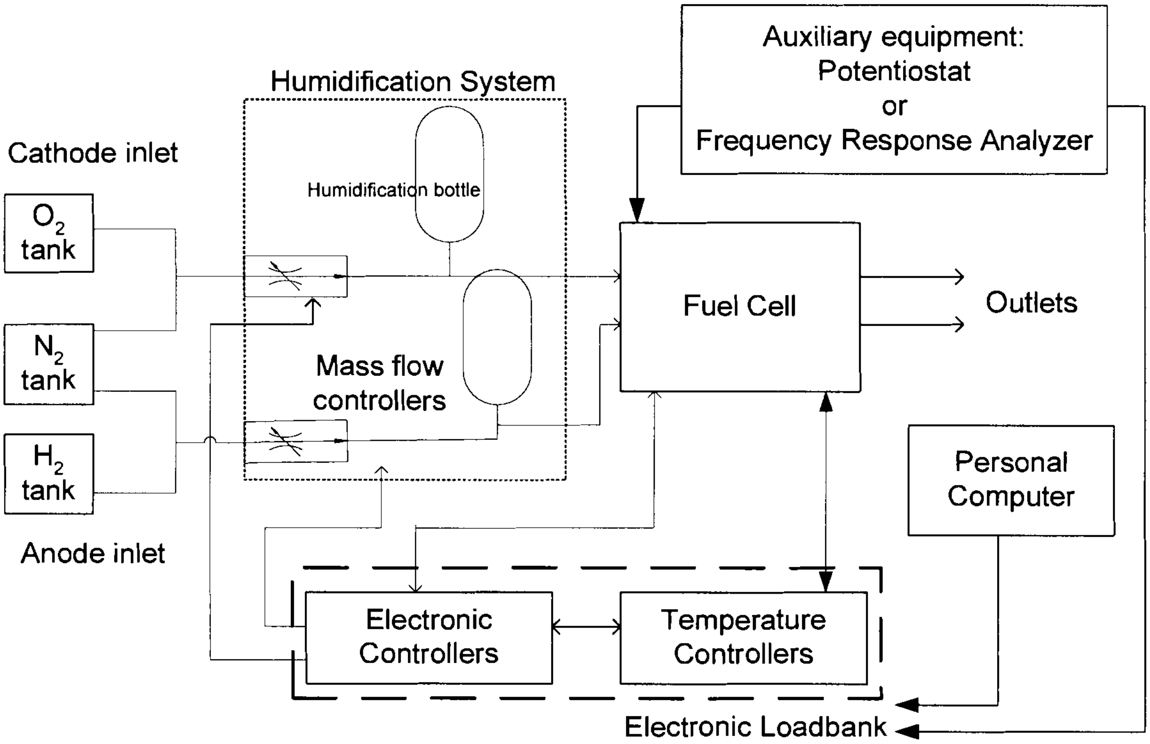

Figure 3.7: Simplified schematic diagram of a fuel cell system.

Chapter 4 : The Role of Ion Exchange Capacity on Membrane / Gas Diffusion Electrode Interfaces: A Half-Fuel Cell Study

4.1 Abstract:

The effect of ion exchange capacity (IEC) of tetrafluoroethylene-g-polystyrene sulfonic acid membranes (ETFE-g-PSSA) on the electrochemical oxygen reduction reaction at the membrane/catalyst layer interface is investigated. In the half-fuel cell system the catalyst layer is hot-pressed to a ETFE-g-PSSA membrane forming a half membrane electrode assembly (HMEA). The working electrode is exposed to liquid electrolyte at the membrane side and to O_2 gas at the gas diffusion layer side. Measurement of electrochemically active surface area by CO stripping reveals that membranes with higher IEC result in higher active surface area of the electrode. In contrast, they exhibit lower oxygen reduction performance. The experimental results are analyzed using the agglomerate model for PEMFC cathode. The extracted effective diffusion coefficients of oxygen (0.62 - 1.25 x 10^{-5} cm^2 s^{-1}) and O_2 solubility (2.03 - 2.80 mmol l^{-1}) in the catalyst layers are close to the corresponding values found in fully

hydrated ETFE-g-PSSA bulk membranes and H_2SO_4. A simple model of percolation for gas-pores used to estimate the extent of flooding reveals that ~67-70% of void space in the catalyst layer is filled with water. The membrane's IEC regulates the extent of flooding in the cathode, which in turn affects its electrochemical characteristics.

4.2 Introduction:

Development of gas diffusion electrode and proton conducting membrane materials has gained much interest in the past decade. The influence of Nafion and poly(tetrafluoroethylene) (PTFE) in the catalyst layer have recently been investigated. Giorgi *et. al.* investigated the influence of PTFE content in gas diffusion electrodes (GDE) on the kinetics of the oxygen reduction reaction (ORR) using an ex-situ electrochemical half-fuel cell approach[91]. They showed that optimal ORR kinetics were obtained for a PTFE content of 10 wt%. Higher PTFE content resulted in a decrease in the total porosity of the electrode, a decrease in active Pt catalyst area, and hence, a decrease in catalyst utilization. However, for catalyst layers with less than 10 wt% PTFE content are less hydrophobic, exhibit a higher propensity to electrode flooding, and are characterized by a decrease in ORR performance. In complementary studies, Antolini *et. al.* investigated the influence of Nafion loading in GDEs, also using an electrochemical half-fuel cell approach [47]. They found two opposing effects: while increasing the Nafion content increased the active catalyst area, by providing a larger contact area with electrolyte, gas diffusion channels became increasingly restrictive thereby diminishing ORR kinetics. A Nafion loading of 0.67 mg cm^{-2} was reported to provide an optimum performance.

With the exception of ionic resistance, the role of the proton conducting membrane on the electrochemical properties of the membrane-GDE interface is not clear; although it is well established, using Pt microelectrodes, that physicochemical properties of proton conducting membranes exert a strong influence on the ORR[50,51,58,75,81,82]. The membrane's role is not only to support proton conduction, but also to regulate the balance between water and reactant gases at the membrane/electrode interface. It has been demonstrated by Basura *et. al.*[49,58,83], Buchi *et. al.*[50], and Chuy *et. al.*[82] that the fluorocarbon matrix of Nafion enhances O_2 solubility. The membrane acts as an O_2 reservoir and improves ORR kinetics. For a given class of membrane, those with lower ion exchange capacity (IEC) contain less water, are more hydrophobic, dissolve more O_2, and enhance ORR in the kinetically controlled region. In contrast, they lead to a smaller mass transport limited current because of the lower rate of O_2 diffusion and lower O_2 permeability.

Despite the clear indication that the nature of the proton conducting membrane affects the ORR, to the best of our knowledge there are no reports describing the role of a membrane's IEC on the ORR, active catalyst area, and catalyst utilization for membrane/GDE interfaces. In order to investigate these relationships a series of partially fluorinated, radiation grafted proton conducting membranes based on tetrafluoroethylene-*g*-polystyrene sulfonic acid (ETFE-g-PSSA) are evaluated using the electrochemical half-fuel cell technique. The experimental results were analyzed by the agglomerate model for PEMFC cathodes. The validity and applicability of this work to PEMFC systems is discussed.

4.3 Experimental:

4.3.1 Membranes

Four ETFE-*g*-PSSA membranes (M1 to M4) having different graft weights (32 to 46 wt%) were used in this study. These membranes were chosen because their IECs, water contents, proton conductivities and mass transport properties had been determined in a previous investigation using a Pt-microelectrode technique [75], and therefore their influence on the electrochemical properties of the catalyst layer under half-fuel cell conditions can be correlated. Nafion 117 (DuPont) membrane was also used for comparison. All membranes were pretreated (Section 3.1.2). The membrane's IEC, water content and proton conductivity are listed in Table 4.1.

Table 4.1: Physicochemical properties of ETFE-g-PSSA (M1-M4) and Nafion 117 membranes. (*) data reported in ref[75].

Membrane	IEC* (mmol g^{-1})	Water content* (wt%)	Proton conductivity* (S cm^{-1})	Thickness (μm)
M1	3.27	62	0.30 ± 0.02	60 ± 3
M2	2.56	52	0.22 ± 0.01	62 ± 3
M3	2.45	49	0.20 ± 0.01	61 ± 2
M4	2.13	45	0.19 ± 0.01	59 ± 3
N117	0.91	19	0.07 ± 0.01	172 ± 4

4.3.2 Gas Diffusion Electrodes:

In order to keep the GDE composition constant in the experiments, a large piece of GDE (12 x 15 cm^2) was fabricated and small pieces (2.1 cm diameter) were cut. A GDE containing 0.78 mg Pt cm^{-2} (20wt% Pt/Vulcan XC-72) and 20 wt% impregnated Nafion was fabricated following the described procedure (section 3.2.2). The homogeneity of catalyst particles distribution on the large piece of GDE was evaluation in section 3.2.3. Small electrodes cut from different locations of the GDE displayed a small variation of electroactivity.

4.3.3 Fabrication of Half-Membrane Electrode Assemblies (HMEA):

ETFE-*g*-PSSA membranes (M1, M2, M3 and M4) with different IEC (3.27, 2.56, 2.45 and 2.13 mmol g^{-1}, respectively) and Nafion 117 (0.91 mmol g^{-1}) were used to fabricate HMEA-1, HMEA-2, HMEA-3, HMEA-4 and HMEA-N, respectively. Individual membranes were placed on top of the electrocatalyst side of the GDE and the membrane/electrode unit was hot-pressed at 220 kg cm^{-2} and 150 °C for 90 seconds. Circular buttons (2.1 cm diameter) were cut from the HMEA and equilibrated in water at 60 °C for 10 minutes before assembling into the half-fuel cell test apparatus.

4.3.4 Measurement of Electrochemically Active Surface Area

The most widely used technique for measuring surface area of carbon supported Pt electrocatalyst for PEMFC are adsorption methods, which can be classified into (i) physical adsorption for Van der Waals molecular interactions and (ii) chemical adsorption associated with chemical bond formation. The physical adsorption method based on the principle of gas adsorption on solid surface was developed by Brunauer, Emmett and Teller (BET)[113]. The technique is useful for measuring surface area and pore size distribution, which may lead to understanding in transport phenomena in the electrodes of PEMFC. However, arising from Van der Waals interactions the adsorbate gas forms a layer irrespective of the adsorbent. This non-selectivity of the physical adsorption approach is unsuitable for measuring Pt surface area in the presence of carbon support. On the other hand, the chemisorption approach can yield selectivity in the adsorbate to adsorbent interactions and hence deconvolution of Pt surface from carbon support is possible. For this reason, electrochemical chemisorption techniques, which can be performed in-situ in the half-fuel cell and the fuel cell environment, are employed in this study.

Cyclic voltammetry was used to obtain the columbic charges associated with hydrogen adsorption[114-118] and CO oxidation[117,119] on Pt surface. Prior to the measurements, the electrode's potential was cycled 20 - 25 times at 30 mV s^{-1} to remove trace O_2 in the porous electrode, and to obtain reproducible voltammograms. For CO voltammetric stripping, the HMEA's potential was held at 0.125 V for 2 minutes while CO gas was supplied at 30 ml min^{-1} to the electrode. Following CO adsorption, the working chamber was purged with N_2 at 100 ml min^{-1} for 1 min, and the electrode cycled 3 times between 0.05 and 1.40 V at 10 mV s^{-1}. The CO and hydrogen adsorption charges were calculated from the voltammograms in the potential range of 0.75 - 1.10 V, and 0.05 – 0.40 V, respectively. The approximate conversion factors[12] of 0.21 μC cm^{-2} for hydrogen adsorption and 0.42 μC cm^{-2} for CO oxidation were assumed for conversion of adsorption charges to the electrochemically active surface area of Pt (ESA).

4.3.5 *Measurement of Uncompensated Resistance*

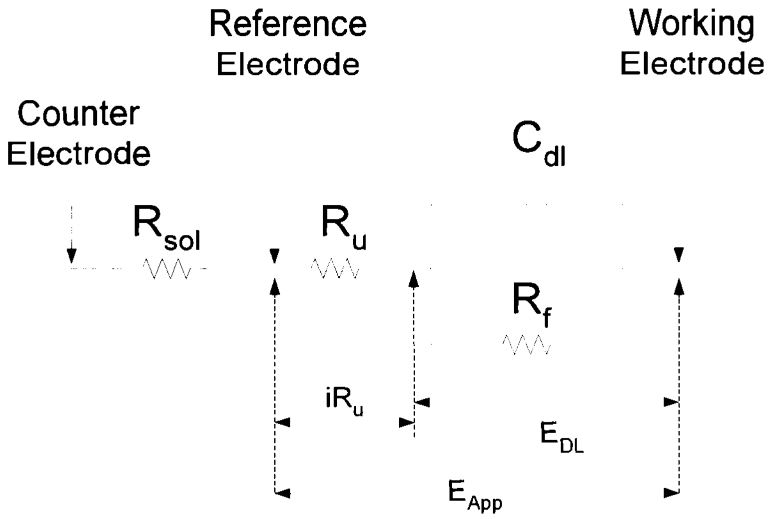

Figure 4.1: A simplified electrical model for a three-electrode electrochemical cell.

In a simple model for the electrical connection in a three-electrode electrochemical cell (Figure 4.1), the faradaic processes at the working electrode can be represented by a parallel RC circuit consisting of a faradaic resistance (R_f) and a double layer capacitance (C_{dl})[120,121]. A potentiostat controls and measures the potential of the working electrode with respect to the reference electrode. The applied potential of the potentiostat (E_{app}) is often not equal to the double layer potential of the working electrode (E_{DL}) because an ionic resistance in the electrolyte and an electronic resistance in the electrode are present. The sum of these resistances is often referred to as an uncompensated resistance (R_u) [122]. If the potential loss due to iR_u is significant, the accuracy in measuring E_{DL} is compromised. This problem can be overcome by compensating E_{app} by an amount equal to iR_u (Equation 49). The iR_u compensated potential (E'_{app}) represents E_{DL}, which is the key parameter driving an electrochemical reaction.

$$E_{\text{app}} = E_{\text{DL}} - i \cdot R_{\text{u}} \tag{49}$$

$$E'_{\text{app}} = E_{\text{app}} + iR_{\text{u}} = E_{\text{DL}} \tag{50}$$

R_u can be determined by the current interruption technique or by measuring the high frequency electrode impedance using electrochemical impedance spectroscopy (EIS). Both of these techniques exploit the difference between the fast response time of R_u and the slow faradaic R_fC_{dl} time constant. Suitable for a galvanostatic measurement, the former technique was employed in the fuel cell experiments and is described in Chapter 5. For a measurement in the potentiostatic mode, the latter technique was used and its description is given below.

When the electrical circuit between the working and the reference electrode (Figure 4.1) is probed by alternating potentials, the impedance of the capacitor ($1/\omega C$) varies with frequency. At low frequencies (< 1Hz), the capacitance has high impedance and may act as an open circuit. The current can pass through R_f and R_u, and the electrode impedance is equal to $R_f + R_u$. On the other hand, at high frequencies (~10^4 Hz), the capacitor acts as a close circuit allowing current to pass through. The potential drop only occurs at R_u. Consequently, the electrode impedance represents R_u. This principle is illustrated in Figure 4.2.

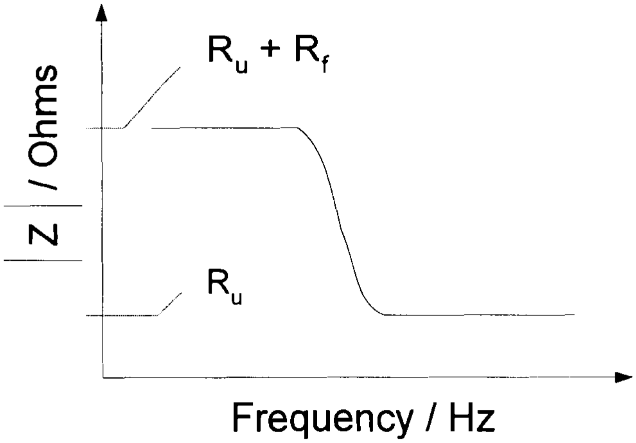

Figure 4.2: Application of high frequency impedance measurement to differentiate uncompensated resistance (*R_u*) from faradaic resistance (*R_f*).

Determination of R_u by measuring high frequency electrode impedance was performed using a lock-in amplifier (Princeton Applied Research 5210) connecting to a potentiostat (263A, Princeton Applied Research) and controlled by PowerSine® data acquisition software (Princeton Applied Research). The perturbation potential was set at 5 mV (r.m.s.) and the frequency was varied from 5mHz to 10 kHz. For each HMEA, the measurements were performed at open circuit potential, 0.80, 0.60 and 0.40 V bias potentials to determine a variation of R_u with the operating potential. iR_u compensation were performed by the positive feedback technique available in PowerCV software. The measured value of R_u for individual experiment was continuously compensated to the applied electrode potential, E_{app}, by an amount $\gamma \cdot i \cdot R_u$ where γ was the user specified percentage of compensation. In most experiments involving potential scanning, 100% compensation would result in severe distortion of the current response[121], which was generally believed to originate from the intrinsic electronic design of potentiostat. Consequently, the compensation was set at 85% for all experiments and the remaining 15% was mathematically compensated for.

4.3.6 Experimental Protocol:

Since many parameters have the potential to significantly affect the current-potential response, the nature of the measurements requires consistent control of experimental conditions. The following experimental protocol was devised: (1) After hot pressing, half membrane electrode assemblies (HMEAs) were equilibrated in warm water (60 °C) for 10 min, and assembled into the half-cell apparatus containing H_2SO_4 purged with N_2; (2) Oxygen (45 ml min^{-1}) was passed through the reaction chamber, in direct contact with the backside of the carbon cloth substrate, and slow-sweep voltammetry performed at 5mV s^{-1} between 1.30 and 0.40 V. The current-potential response became steady and reproducible after 2-3 potential cycles. (3) R_u was determined by measuring electrode impedance at high frequencies ($10^3 - 10^4$ Hz) and (4) R_u compensation was set to 85% of the experimentally-determined R_u and slow-sweep voltammetry carried out. (5) Cyclic voltammetry was then carried out under N_2-saturated conditions by replacing O_2 with N_2. The electrode's potential was cycled 20-25 times at 30 mV s^{-1} to remove trace O_2 in the porous electrode, and to obtain reproducible voltammograms. (6) The electrochemically active surface was determined using the CO voltammetric stripping. The HMEA's potential was held at 0.125 V for 2 minutes while CO gas was supplied at 30 ml min^{-1} to the carbon cloth side of the electrode. Following CO adsorption, the working chamber was purged with N_2 at 100 ml min^{-1} for 1 min, and the electrode cycled 3 times between 0.05 and 1.40 V at 10 mV s^{-1}.

4.3.7 Fitting the Agglomerate Model to the Experimental Data:

The agglomerate model, adapted from the earlier works by Perry *et al.* [89] and Jaouen *et al.*[100], is described in section 2.2. The fourth order Runge-Kutta method using MATLAB software was used to solve the model. The total current density, proton current density and O_2 concentration distribution were computed between 1.229 and 0.400 V using the base-case conditions listed in

Table 4.2. These base-case parameters were kept constant throughout fitting of the model to the different HMEAs experimental data. The HMEA-dependent constants, the exchange current density (i_o) and the active surface area per unit volume of the catalyst layer (A_a), were calculated from individual Tafel plots and the electrochemically active surface area, respectively. The reference solubility of oxygen (c_o^{ref}), which is defined as the position independent concentration of oxygen dissolved at the surface of the agglomerate in equilibrium with 1 atm pressure of gaseous O_2 in the catalyst layer at open circuit potential, the effective diffusion coefficient of O_2 in the gas diffusion layer (D_{GDL}^{eff}) and the effective O_2 diffusion coefficient in the catalyst layer (D_{CL}^{eff}) were variable parameters. It is noteworthy that attempts to fit the agglomerate model to the experimental results using D_{GDL}^{eff} and D_{CL}^{eff} as the only two variable parameters were unsatisfactory. The three variable functions (D_{GDL}^{eff}, D_{CL}^{eff} and c_o^{ref}) were adjusted using the non-linear least squares fitting method.

Table 4.2: Base-case parameters of the agglomerate model.

Parameters	Value
Cell temperature (T)	298 K
Cathode oxygen pressure (P)	1 atm
Cathode transfer coefficient (α_r)	0.58
Diffusion coefficient of O_2 in Nafion [75] (D_N)	0.6×10^{-5} cm^2 s^{-1}
Oxygen Henry's constant (K) [75]	14
Proton bulk conductivity (σ)	0.07 S cm^{-1}
Active layer thickness (L)	50 μm
Active layer porosity (ε_c)	0.55
Agglomerate radius (R_a)	0.25 μm
Gas phase diffusion coefficient of O_2 (D_g)	0.227 cm^2 s^{-1}
Gas diffusion layer thickness (L_{GDL})	350 μm
Exchange Current Density (i_0)*	1.58, 1.27, 1.66, 3.54 and 3.12 mA m^{-2}

4.4 Results and Discussion:

4.4.1 Electrochemically Active Surface Area (ESA)

A typical cyclic voltammogram following CO adsorption onto the Pt for a HMEA is shown in Figure 4.3a. Adsorbed CO is oxidized and removed during the first potential cycle, as indicated by the anodic peak at 0.85V. Subsequent cycles show no trace of CO oxidation. The electrochemically active area was determined by integration of the anodic Faradaic current peak for CO oxidation using 420 μC cm^{-2} as the conversion factor for charge to area[12]. Similarly, the area under the hydrogen adsorption peaks between 0.4 and 0.05V were converted to active catalyst area using 210 μC cm^{-2}. The electrochemically active surface areas are listed in Table 4.3. A difference in the active area calculated from the two methods is usually observed[123]. In the hydrogen adsorption method, the presence of Nafion in the catalyst layer causes a poorly defined adsorption peaks, which renders determination of the lower integration limit (~50 mV) difficult. In addition, there is an error associated with a displacement in the electrode potential due to uncompensated resistance. These factors can contribute to uncertainties in the active area calculation. For this reason, the well-defined CO oxidation peak is used in this work.

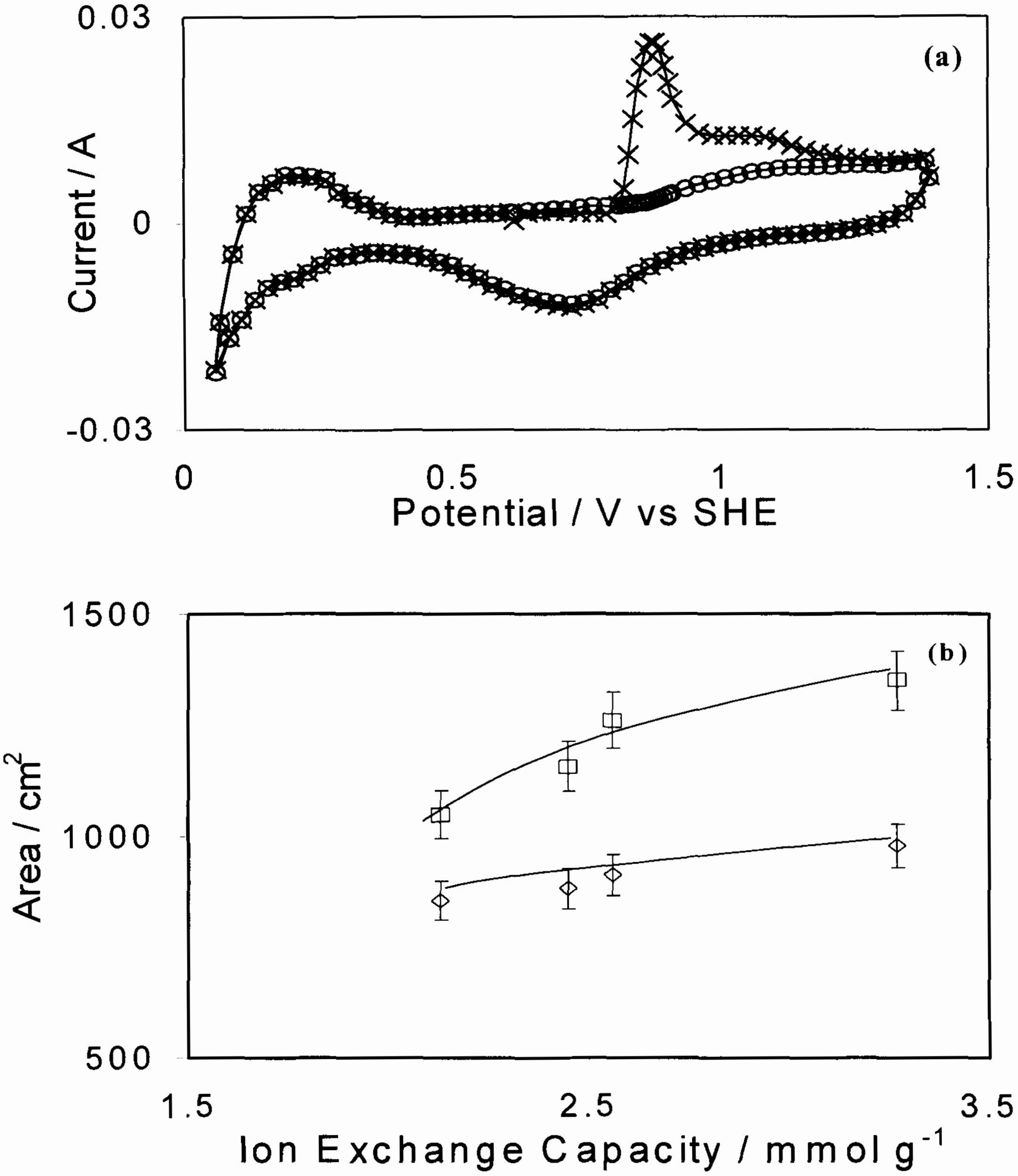

Figure 4.3: (a) Cyclic voltammogram of HMEA-B to determine the electrochemically active surface area under conditions of 20 °C and N_2 sat. 1.0 M H_2SO_4. After CO adsorption, first potential sweep at 0.60 V (-x-) and subsequent cycle (-O-). Scan rate = 10 mV/s. (b) Plot of electrochemically active surface area in the HMEA versus IEC of the constituent membrane. Active area obtained from the charge under CO desorption (□) or hydrogen adsorption (◊).

The electrochemically active area determined by adsorption-desorption of CO and hydrogen corresponds to the surface area of Pt that is in direct contact with electrolyte. The active area of ETFE-*g*-PSSA – based HMEAs can be seen to increase with increasing IEC of the membrane. The higher the IEC, the larger its water content in the water-swollen state[75]. This influences the membrane/electrode interface by facilitating “wetting”. The Nafion-based electrode, HMEA-N, which is relatively hydrophobic, possesses a lower electrochemically active surface area. Thus, preliminary evidence indicates the membrane exerts a direct influence on the electrochemistry of the HMEA.

Table 4.3: Properties of half-membrane electrode assemblies with different membrane's IEC; electrochemically active surface area (ESA) obtained from the charge under the CO desorption and H adsorption regions; uncompensated resistance (R_u) determined from high frequency impedance measurements.

Half-Membrane Electrode Assembly (IEC)	ESA (cm^2)		R_u / Ω (± 0.03)
	H	CO	
HMEA-1 (3.27)	980	1350	2.49
HMEA-2 (2.56)	910	1260	2.18
HMEA-3 (2.45)	880	1150	2.12
HMEA-4 (2.13)	860	1050	1.70
HMEA-N (0.91)	630	860	2.42

4.4.2 Steady-State Polarization

The potentiodynamic steady state polarization curves of HMEAs prepared with different ETFE-*g*-PSSA membranes are shown in Figure 4.4a. In the kinetically-controlled region (E more positive than +0.90 V), the ORR curves are very similar. At potentials more negative than +0.70 V the current density at a given potential increases with *decreasing* IEC of the membrane. This difference is readily discernable at potentials more negative of +0.55V.

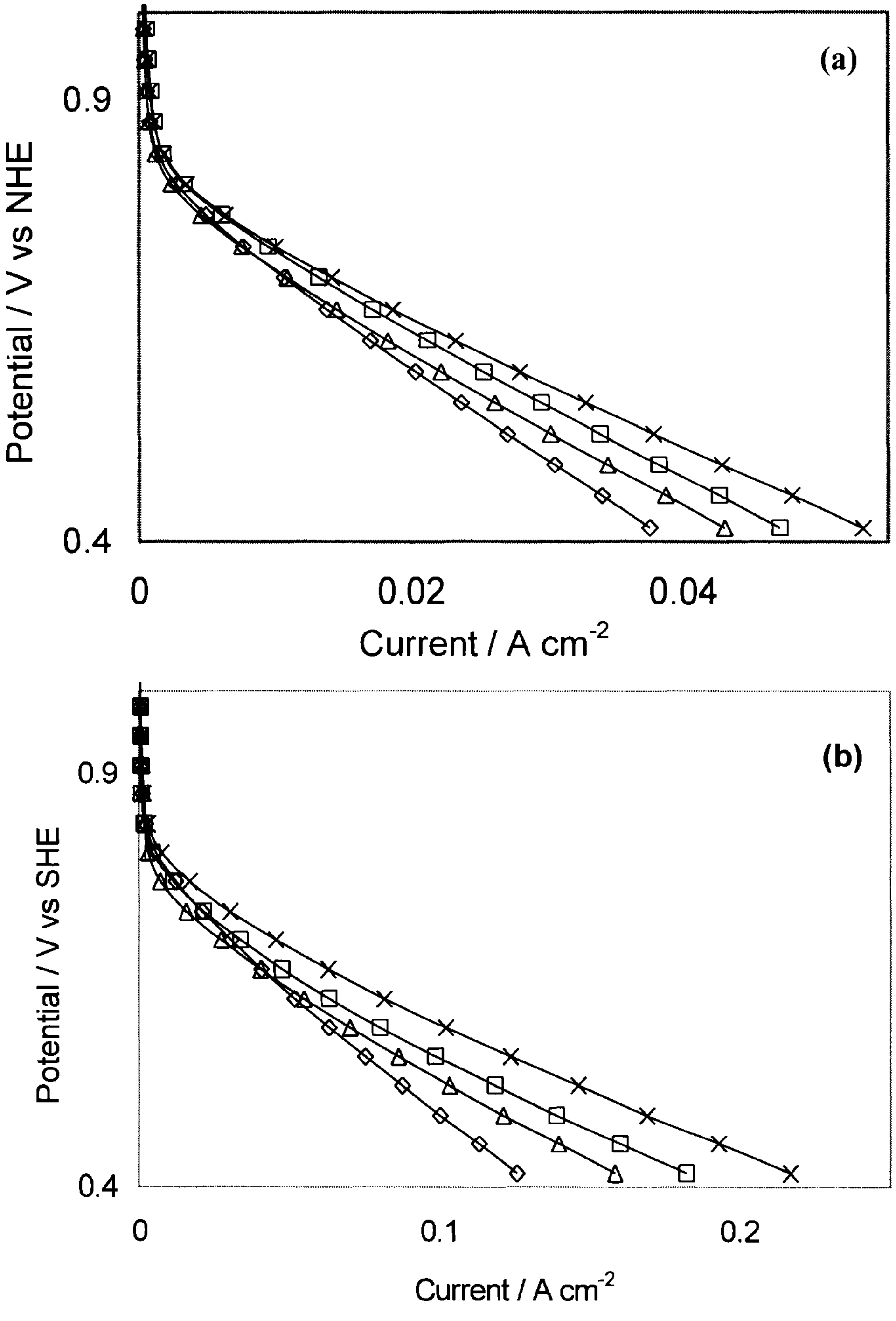

Figure 4.4: Oxygen reduction polarizations (a) without iR_u compensation and (b) iR_u compensation of different HMEAs under flow rate of 45 mL O_2 /min, 20 C, ambient pressure. HMEA-1 (--◇--), HMEA-2 (--△--), HMEA-3 (--□--), HMEA-4 (--×--). Scan rate = 5 mV s^{-1}.

The actual potential at the HMEA differs from the applied potential by the quantity iR_u. The values of R_u for all HMEAs were estimated from the impedance plot, shown in Figure 4.5. For each HMEA, the values of $|Z|$ between 10^3 and 10^4 Hz were averaged and the R_u values for all HMEAs are listed in Table 4.3. When the applied bias potential of the electrodes were varied from OCP to 0.40 V, no significant changes in the values of R_u were observed (see Figure 4.6). It is noteworthy that a decrease of the electrode impedance at low frequencies (< 1 Hz) was due to a decrease in the kinetically controlled charge-transfer resistance as a result of increasing electrode overpotential.

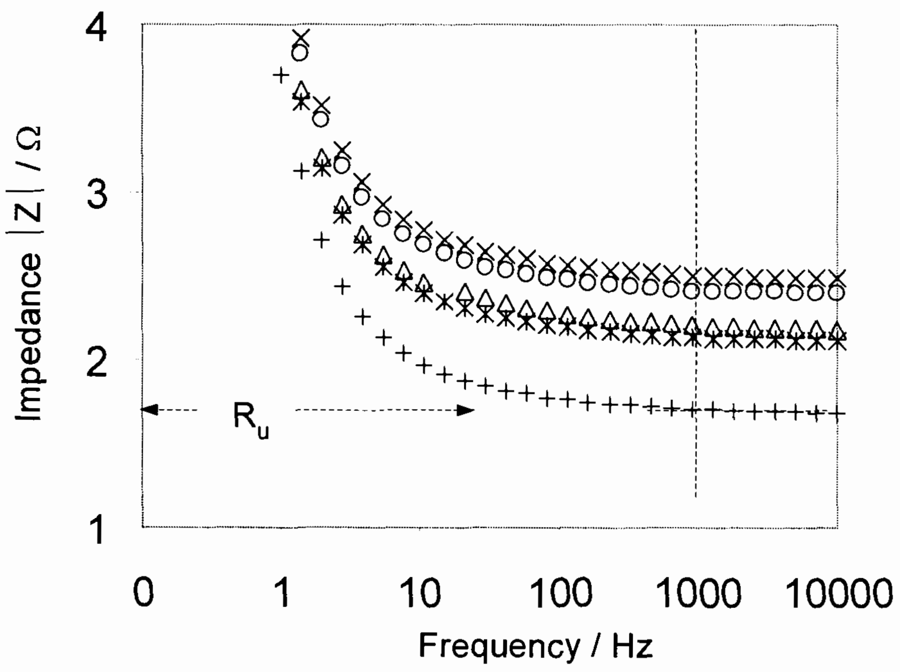

Figure 4.5: Impedance spectra at open circuit potential for (X) HMEA-1, (Δ) HMEA-2, (★) HMEA-3, (+) HMEA-4 and (O) HMEA-N to determine the uncompensated resistance.

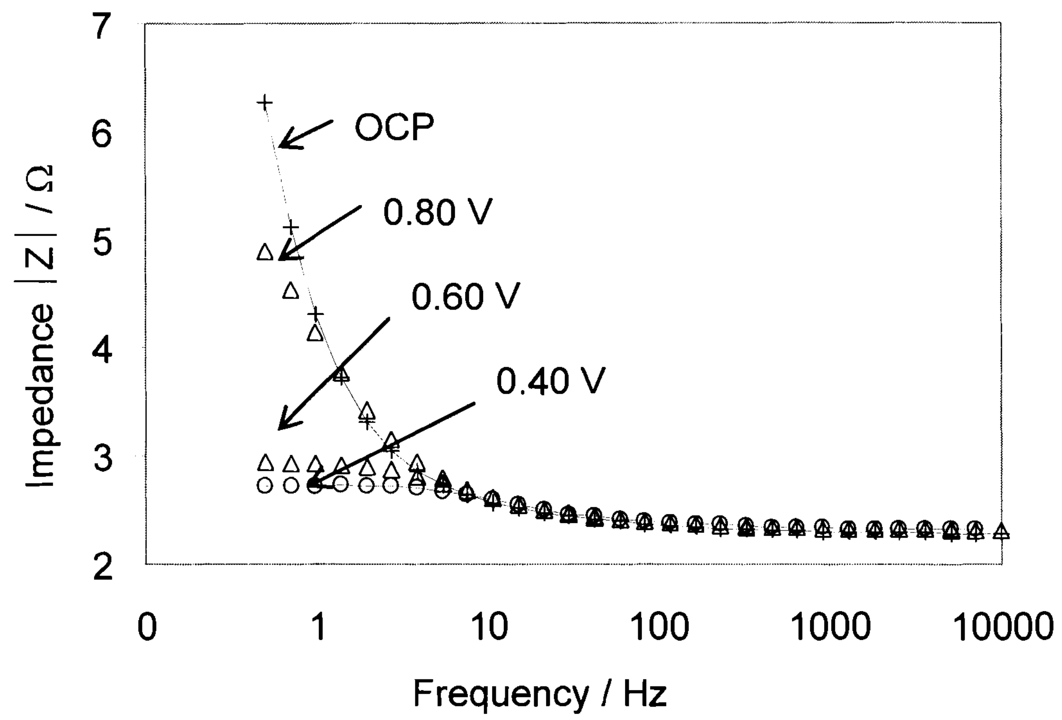

Figure 4.6: Electrochemical impedance spectra of HMEA-N at different bias potential.

From Table 4.3, despite proton conductivity of ETFE-g-PSSA membranes increasing with IEC, R_u is observed to increase with IEC. The trend may be attributed to an increase in electronic resistance due to an increase swelling of the membrane. The catalyst layer in the conventional fuel cell is under mechanical compression. This significantly reduces the electronic resistance to almost negligible. In the half-fuel cell apparatus, mechanical compression only takes place around the rim of HMEA. The majority of the catalyst layer area is not under compression. This potentially leads to a significant electronic resistance. For the trend observed, dealing first with the ETFE based HMEAs, the higher the IEC, the higher the ESA, and presumably the higher the water content. The catalyst layers of higher IEC-HMEA may be slightly more electronically resistive due to swelling. This may lead to an increase in the contact resistance between particles (Pt/C). The HMEA containing Nafion has a high resistance. This could be attributed to the thickness of Nafion being three times higher than ETFE-g-PSSA membranes, and the ionic resistance correspondingly so. If the thickness difference is corrected for, the Nafion HMEA has the lowest resistance.

Clearly, the variation in R_u is not due to differences in proton conductivity of the membrane. Furthermore, iR_u compensated polarization curves of all HMEAs should be superimposable if the role of the bulk membrane was simply to transport protons, i.e. the faradaic contribution of ORR with Pt catalyst should be the same. Figure 4.4b depicts iR_u compensated polarization curves for all HMEAs. iR_u compensation accentuates the differences between HMEAs indicating factors other than proton conductivity are affecting the polarization curves. The rate of ORR increases with decreasing IEC of the membrane. A correlation of ORR kinetics with electrochemically active surface area was dismissed because HMEA1, which possessed the largest electrochemically active surface area, gave the lowest ORR performance. This led to the consideration that the membrane exerts an influence on the polarization curves by regulating the balance between gas and liquid in the GDE.

4.4.3 Fitting the Agglomerate Model:

The agglomerate model was employed in order to explain the role of the membrane on ORR kinetics at HMEAs. Mass-transport properties in the HMEAs were extracted by fitting this model to experimental results, and these are presented in Table 4.4. Comparison between the best-fit simulation and experimental results are shown in Figure 4.7. The reference concentration (c_0^{ref}), which corresponds to the O_2 concentration at the agglomerate surface, is calculated to be between 2.0 and 2.8 mmol l^{-1}. The agglomerate model assumes the carbon supported catalyst and impregnated Nafion ionomer are well mixed such that individual agglomerates are homogeneous. c_0^{ref} is, by definition, equivalent to the solubility of oxygen at the Pt-membrane interface. In a recent Pt microelectrode/ETFE-g-PSSA membrane investigation, Chuy et. al. [75] determined c_{O2} in fully hydrated membranes at 3 atm. pressure to be 9.2 mmol l^{-1} for Nafion 117 and between 4.1 and 5.1 mmol l^{-1} for ETFE-g-PSSA. The latter are similar in value to O_2 dissolved in 1M H_2SO_4 (5.0 mmol l^{-1}). In this work, c_0^{ref} are 1/4 to 1/2 the values determined by the microelectrode technique. This can be attributed to the different O_2 pressure used in the two techniques (3 atm. vs 1atm O_2) and the fact that the percentage volume fraction of Nafion in the catalyst layer is less than 100 % due to the presence of Pt/C. As indicated in Table 4.4, c_0^{ref} increases slightly with a decrease in the membrane's IEC. The same trend observed in the Pt microelectrode investigations[75] and was attributed to an increase in hydrophobicity.

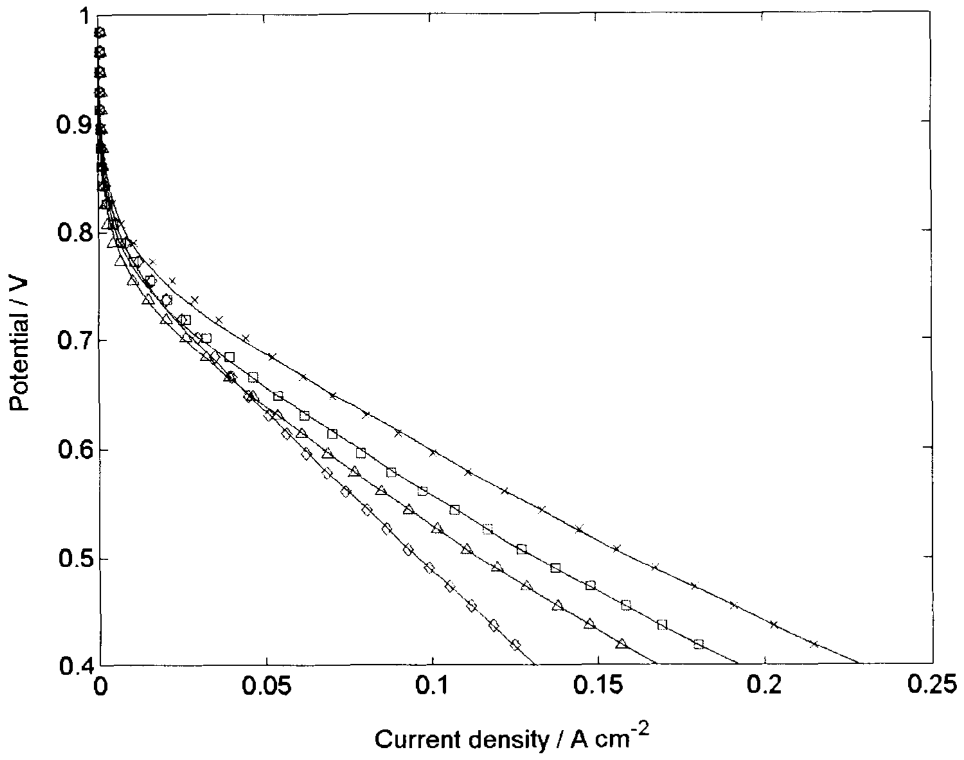

Figure 4.7: Best fitted simulation results (solid lines) to the experimental data (symbols) for ETFE-g-PSSA HMEAs, HMEA-1 (◇), HMEA-2 (△), HMEA-3 (□), HMEA-4 (×).

The effective diffusion coefficient of oxygen in the CL and in the GDL decreases with increasing IEC of the membrane. It is proposed that this is due to an increase in their water content of the HMEA, which reduces the electrode porosity and restricts gaseous O_2 mass transport within CL and GDL. It is important to point out this is a manifestation of the half-fuel cell apparatus, in which the HMEA is immersed in liquid electrolyte, thus rendering the electrode more susceptible to flooding.

Table 4.4: List of parameters obtained from best-fit agglomerate model to the experimental results

	D_{GDL}^{eff} ($cm^2/10^{-3}$ s)	D_{CL}^{eff} ($cm^2/10^{-5}$ s)	c_o^{ref} (mmol l^{-1})	Error* (10^{-3})
HMEA-1	0.58	0.63	2.03	5.7
HMEA-2	1.00	0.81	2.34	8.2
HMEA-3	1.16	0.95	2.25	6.9
HMEA-4	1.24	1.25	2.80	4.8
HMEA-N	1.02	0.74	3.08	1.5

* Error of fitting the current density determined by non-linear least square fitting method.

The effective diffusion coefficient of the catalyst layers (D_{CL}^{eff}) are the same order of magnitude as the diffusion coefficient of O_2 in fully hydrated Nafion 117 (0.6 x 10^{-5} cm^2 s^{-1}), ETFE-g-PSSA (0.44 – 1.15 x 10^{-5} cm^2 s^{-1}) and liquid water (2.4 x 10^{-5} cm^2 s^{-1}, [124]) - all determined by the Pt microelectrode technique[51,75]. This clearly indicates that transport of O_2 in the catalyst layer is mainly by diffusion through liquid and/or fully hydrated polymer phase, and not gaseous diffusion through void space. The effective diffusion coefficients in the gas diffusion layer (D_{GDL}^{eff}) are two orders of magnitude higher than D_{CL}^{eff} , which indicates gaseous diffusion through void space – an expected result since the GDL is wet-proofed. It is noteworthy that the hydrophobicity of the PTFE coated GDL is adequate to prevent the liquid electrolyte from penetrating through it.

There was no significant accumulation of liquid electrolyte observed at the back of gas diffusion layer during measurements. If the liquid electrolyte did penetrate the GDL, the electrochemical response would be extremely unstable due to the formation of gas bubbles between the electrolyte and the inlet gas. This also was not observed.

4.4.4 Diffusion of Oxygen

Two predominant modes of O_2 transport may contribute to the supply of O_2 to the reactive sites within the catalyst layer. Where reactive sites are located in mesopores[7] (or primary pores, 10-40 nm diameters as determined by Uchida et. al.[94]) inside agglomerates surrounded by liquid electrolyte, Knudsen diffusion and diffusion in the electrolyte phase is expected to dominant mechanism. When the reactive sites are accessible via macropores (secondary pores, 40-300 nm), O_2 transport is dominated by gas phase molecular diffusion, which has a much higher diffusion coefficient. In real systems, both modes of transport may contribute.

Oxygen is assumed to move in the catalyst layer via coexisting pathways of gas and liquid diffusion. The effective diffusion constant D_{CL}^{eff} consists of a gaseous phase diffusion component (D_g) and a residual diffusion (D_r), which represents diffusion in liquid water and hydrated polymer network. For oxygen diffusion in pores filled with liquid in the catalyst layer, gaseous oxygen inlet in the gas diffusion layer must first dissolve in the liquid phase at the catalyst layer

---

[7] According to the IUPAC classification, mesopores correspond to pores with a diameter of between 2 and 50 nm, and macropores correspond to pores with a diameter > 50 nm.

interface before it diffuses in liquid phase. The flux of oxygen is proportional to its solubility (Henry's constant) in the liquid. For a hypothetical diffusion of oxygen in the coexisting parallel pathways of gaseous phase (D'$_g$) and liquid phase (D'$_l$), both pathways have equal volume, the effective diffusion coefficient of oxygen (D$^{'eff}$) in such system can be derived from a mass balance equation (see Appendix 4.7.1) to be

$$D^{'eff} = D_g^{'} + D_l^{'}H \tag{51}$$

where $D_l^{'}H$ represents residual diffusion term. This general expression will be used later to develop a simple estimation of the extent of flooding in the catalyst layer.

4.4.5 Simple Model of Percolation in the Gas-Pore Space

A simple model of percolation in the gas-pore space is used to calculate the degree of flooding in the void space in the catalyst layer. According to percolation theory, diffusion in the gas phase is related to the volume fraction of gas space and the coordination of pore space arrangement in the catalyst layer. The same argument applies in the case of diffusion in the liquid phase. Using the concept of parallel co-existing pathways described above, the effective diffusion coefficient can be expressed as

$$D_{CL}^{eff} = D_e(v_g - v_p)^t \Theta\left(v_g - v_p\right) + D_l H (v_l - v_p)^t \Theta\left(v_l - v_p\right) \tag{52}$$

where,

$$D_r = D_l H (v_l - v_p)^t \tag{53}$$

and

$$v_g = 1 - v_{Pt} - v_C - v_N - v_l \tag{54}$$

The first term on the right hand side of Equation (52) represents the contribution from gas phase molecular diffusion, where the critical exponent, t, has been demonstrated to be a universal value and independent of the composite structure, but dependent on the system dimensionality[125]. In three dimensions, t is ~2. The percolation threshold for O_2 transport in the catalyst layer, v_p, is assumed to be 0.12; this represents highly coordinated pore space arrangement[126]. The value of the Heaviside-step function, Θ, is either 0 or 1 when v_g-v_p is negative or positive, respectively. This function ensures that when the volume fraction of the gas pores is less than the percolation threshold, there is no contribution from gas phase diffusion. However, in finite (thin) catalyst layers, there exists a finite probability that the gas pores percolate the catalyst layer when $v_g \leq v_p$. The void volume fraction (v_v) in a dry catalyst layer can be calculated by

$$v_v = 1 - v_{Pt} - v_C - v_N \tag{55}$$

v_v can be occupied by gas and liquid such that

$$v_v = v_l + v_g \tag{56}$$

Here the volume fraction of Nafion (v_N ~ 0.104) is assumed fully expanded, 15 vol% higher than its dry volume. The void volume fraction (v_v) in a dry catalyst layer is calculated from the volume fractions of Pt (v_{Pt}), C (v_C) and Nafion (v_N), which are derived from the known electrode composition (20wt %

Pt/C, 0.75 mg Pt cm^{-2} and 20 wt% Nafion ionomer) and its thickness (50 μm) assuming density for Pt[124], C[127] and Nafion[128] to be 21.5, 1.8 and 2.0, respectively. The volume fractions were calculated, and are listed in Table 4.5.

Table 4.5: Volume fractions calculated from the catalyst layer composition and its dimension (3.46 cm^2 and ~50 μm thick)

Composition (dry)	Pt	C	Nafion	Void	Total
Volume Fraction	0.01	0.43	0.10	0.46	1.00

The second term on Equation (52) represents the contribution from liquid phase diffusion where D_l is the diffusion coefficient of oxygen in water[124] (~ 2.4 x 10^{-5} cm^2 s^{-1}). The Henry constant (H) takes into account the physical process of O_2 gas dissolving into the liquid phase at the liquid/gas interface. H is defined as the ratio of oxygen concentration in liquid phase to oxygen concentration in gas phase. For oxygen, H is[124] ~ 1/30. The dissolution process of oxygen reduces the contribution of D_l by ~ 2 orders of magnitude. Using Equation (53) and assuming the void fraction is totally flooded with liquid, i.e. v_l = 0.55 (Table 4.5), the upper limit of D_r is estimated to be ~ 1.5 x 10^{-7} cm^2 s^{-1}. This gives a negligible contribution (less than ~2 %) to D_{CL}^{eff} (10^{-5} – 10^{-6} cm^2 s^{-1}). It is, therefore, justifiable to neglect any contribution from diffusion in liquid and polymer phase in the catalyst layer, unless it is prepared very thin. The effective diffusion coefficient given in Equation (52) is, thus, simplified to

$$D_{CL}^{eff} = D_e(v_g - v_p)^2 \qquad (57)$$

D_e is the "average" gaseous phase diffusion coefficient in straight cylindrical pores (not explicitly taking into account effects of pore size distribution), which is estimated from Satterfield and Sherwood relation[129]

$$\frac{1}{D_{\mathrm{e}}}=\left(\frac{1}{D_{\mathrm{g}}}+\frac{1}{D_{\mathrm{K}}}\right) \tag{58}$$

where D_g is the molecular diffusion coefficient of O_2 (~ 0.189 $cm^2\ s^{-1}$ [124]), determined by molecule-molecule collisions. D_K is the Knudsen diffusion coefficient for gas diffusion in micropores, in which molecule-pore wall collisions prevail. It is estimated using[130]

$$D_{\mathrm{K}}=\frac{1}{3}d_{\mathrm{o}}\sqrt{\frac{8RT}{\pi m}} \tag{59}$$

where m is the molar mass of oxygen and d_0 is the pore diameter. When pore diameters are smaller than the mean free path of molecules between collisions, diffusive transport is controlled by Knudsen diffusion. The mean free path of O_2, estimated at 1 atm. using the kinetic theory of gases, is ~60 nm. Knudsen diffusion prevails in pores with diameters smaller than this value. Pore sizes in PEMFC catalyst layers are distributed in the range of 10 - 40 nm, as determined by Uchida et al.[94]. The lower value of 10 nm is assumed for d_0.

The quantity of interest in this simple model is the volumetric ratio of liquid electrolyte to void space, v_l / v_v. This ratio represents the "*extent of flooding*" in the void space, and can be explicitly expressed by combining Equation (57) and (56).

$$\frac{v_l}{v_v} = 1 - \frac{1}{v_v}\left(v_c + \sqrt{\frac{D_{\mathrm{CL}}^{\mathrm{eff}}}{D_{\mathrm{e}}}}\right) \qquad (60)$$

Using Equation (60), v_l / v_v is solved for all HMEAs, and their values are listed in Table 4.6. The extent of flooding varies from ~0.70 (HMEA-1) to ~0.67 (HMEA-4). The difference and the trend of increasing v_l / v_v with an increase in the IEC can account qualitatively for the experimental observation (see Discussion). However, the low sensitivity of these values is noted. More refined theoretical analysis would be required to quantitatively relate these values to the experimental results. This would be based on more detailed characterizations of pore space (pore size distribution and wetting properties of the pores). Nevertheless, for the purpose of this study, the trend can provide insights into the experimental analysis.

Table 4.6: The extent of flooding estimated from the simple model of percolation in gas-pore space

Sample (IEC)	Extent of Flooding (v_l / v_v)*
HMEA-1 (3.27)	0.70
HMEA-2 (2.56)	0.69
HMEA-3 (2.45)	0.68
HMEA-4 (2.13)	0.67
HMEA-N (0.91)	0.69

* The ratio of the volume fraction of liquid (v_l) to the void fraction (v_v) is the extent of flooding (v_l / v_v).

4.5 Discussion

4.5.1 Interpretation of the Agglomerate Model and the Simple Percolation Model

From Table 4.4, it is clear that the values of D_{CL}^{eff} (0.6 - 1.3 x 10^{-5} cm^2 s^{-1}) for all HMEAs lie between the diffusion coefficients of O_2 in bulk Nafion® and liquid electrolyte, i.e. $D_N < D_{CL}^{eff} < D_l$. This may appear, at first glance, that diffusion in the catalyst layer is predominantly in the liquid phase. Complete flooding of the catalyst layer was considered. In this scenario, all Pt particles located in the fully flooded catalyst layer are electrochemically active, and hence values of ESA are the same for all HMEAs. However, the experimental values shown in Table 4.3 clearly contradict this: ESA increases with the membrane IEC. Hence, the catalyst layer is not fully flooded. A further reason to support this conclusion arises when diffusion of oxygen in the catalyst layer is considered to occur via coexisting pathways of gas and liquid diffusion, and the latter is shown in Section 4.4.5 to be a negligible contribution to D_{CL}^{eff}.

Since the gas phase molecular diffusion coefficient, $D_{O2,g}$ (~10^{-1} cm^2 s^{-1}) is five orders of magnitude higher than D_r (~10^{-6} cm^2 s^{-1}), it is justifiable to assume that the gas space within the secondary pores (40-300 nm) but they do not form a percolation network in the catalyst layer, and hence do not participate in O_2 transport (otherwise D_{CL}^{eff} would be at least one order of magnitude higher).

From the arguments above the most likely scenario is that the gas space in mesopores (10-40 nm) percolates the catalyst layer and contributes to O_2

transport. Micropores (<0.2 nm diam.) are likely to be completely flooded because the capillary pressure and, thus, not further considered. Under the half-fuel cell conditions, gas space within the mesopores may be expected since the carbon support in the agglomerate is the relatively hydrophobic (contact angle ~ 82^{O} for carbon black Vulcan-XC72 [131]). The simple model of percolation indicates that the gas phase percolates the catalyst layer. The Knudsen diffusion coefficient term in Equation (59) accounts for confinement effects of gas diffusion in the mesopores.

The D_{CL}^{eff} decreases with increasing IEC of the membrane (Table 4.4). This is readily explained by an increase in the extent of flooding, which in turn increases the "wetted" Pt surface area – the latter being confirmed by the increase in ESA with IEC of the membrane (Table 4.3). The volume fraction of gas space in the catalyst layer decreases when the membrane's IEC increases; this accounts for the overall decrease in D_{CL}^{eff}, and subsequently the decrease in ORR performance. The proposed hypothesis that mesopores percolate the catalyst layer is consistent with experimental observations.

The simple percolation model provides evidence that the liquid electrolyte penetrates the catalyst layer but does not completely flood it. The extent of flooding depends on the membrane's IEC.

4.5.2 Influence of IEC

The increase in the electrochemically active surface area of HMEAs with membranes of increasing IEC is due to the increased water content in the catalyst layer, and thereby an increase in the "wetted" catalyst area. More specifically, it is shown by the simple percolation model that the membrane regulates the water content in the catalyst layer. An enhancement in ESA, which is beneficial in improving current density of ORR, is offset by the accompanying negative impact of reduced O_2 mass transport due to the filling of mesopores in the catalyst layer with liquid. In the half-fuel cell conditions the catalyst layer is largely flooded and O_2 is transported predominantly via Knudsen diffusion within the mesopores. This is the limiting factor of ORR in the half-fuel cell system.

Earlier work by Giorgi et. al. reported an increase in electrochemically active area (H_2-adsorption on Pt) when the hydrophobicity of the membrane/electrode interface was decreased[91] by incremental lowering of the PTFE content in the catalyst layer from 60 to 10 wt%. Our results are consistent with this observation. Furthermore, Giorgi et. al. observed that when the PTFE content is increased, the ORR performance is decreased. This is in contrast to the present work, where the rate of ORR increases with increasing hydrophobicity of the ETFE-g-PSSA membrane. This can be explained in terms of different limiting factors of the ORR in the two systems: In Giorgi's et al. work, the limitation of the ORR in gas diffusion electrodes with high PTFE content is due to inadequate proton conduction. In this work, the limitation of the ORR using higher IEC membranes is O_2 mass transport due to reduced gas phase diffusion.

Antolini et al.[47] investigated the variation of Nafion content in the catalyst layer. Their work covered both limiting cases of proton conduction and O_2 mass transport in the ORR in half-fuel cells. The Nafion content in the catalyst layer was varied between 0.00 and 1.46 mg cm^{-2}, having optimal performance at

0.67 mg cm^{-2}. With a lower Nafion content than optimal the ORR was limited by proton conduction; with a higher Nafion content, ORR was limited by O_2 mass transport. This agrees with our observations using ETFE-g-PSSA - based HMEAs.

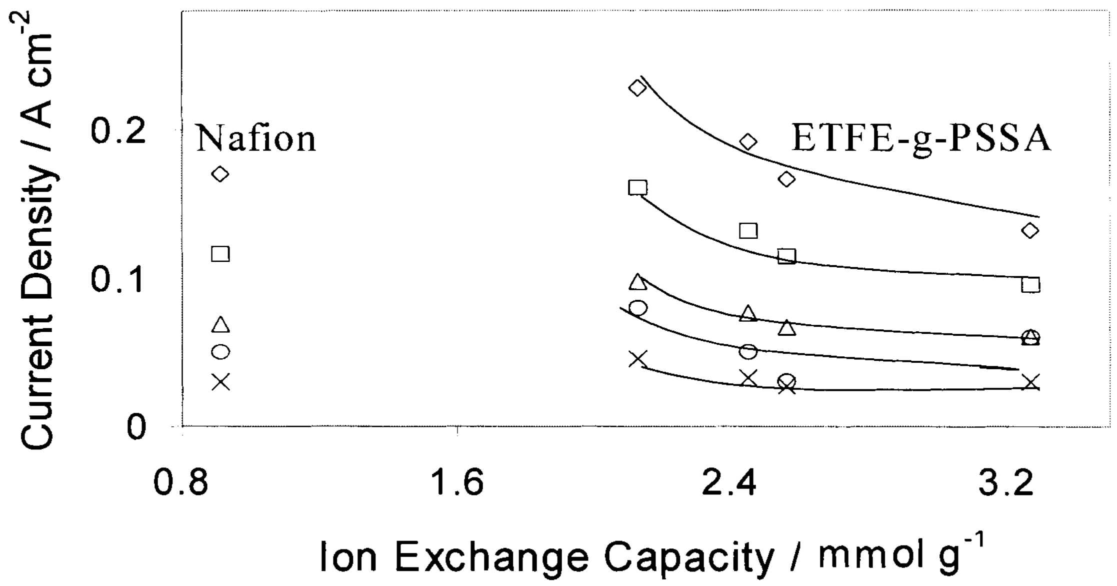

Figure 4.8: Plot of current density at different electrode potential versus HMEA with different membrane's IEC; iR_u compensated HMEA potential at 0.80 V (X), 0.70 V (O), 0.60V (Δ), 0.50 V (◇) and 0.40 V (◊).

The ORR current density, as a function of the membrane's IEC, under different applied potential is compared to HMEA-N and shown in Figure 4.8. HMEA-N yields a comparable ORR current density to those of ETFE-g-PSSA based HMEAs, despite its significantly lower proton conductivity (Table 4.1). This is attributed to its hydrophobic, perfluorinated backbone which enhances O_2 mass transport in the catalyst layer.

Relevance to Fuel Cell Research –The PEM membrane can influence the properties of the catalyst layer. The catalyst layers in the half-fuel cell arrangement possess significant volumes of water and may be considered "semi-flooded". The gas phase molecular diffusion contribution, which is the predominant mode of O_2 transport in fuel cell, is suppressed by flooding. Because of this, the half-fuel cell is unsuitable for mass transport investigations under "real" PEM fuel cell operation. However, the measurement of electrochemically active surface area in the half-fuel cells may provide the maximum accessible electrochemically active area of the electrode. Furthermore, half-fuel cell systems allow for the simulation of fuel cells under flooded conditions and provide information on mass transport parameters under these extreme conditions. Comparison of ESA measured in half-fuel cells and single cells (in-situ) should provide insight into the state of hydration and effective use of Pt in the catalyst layer. These are investigated in Chapter 5.

4.6 Conclusion:

Half fuel cell systems simulate fuel cells under flooded (or semi-flooded) conditions and provide valuable information on available ESA. The nature of the proton exchange membrane influences the catalyst layer and plays a role in the ORR. The electrochemically active surface area of HMEAs increases with increasing IEC of the membrane due to increased wetting of the catalyst. However, catalyst layer porosity and O_2 mass transport is reduced because of the higher water content. Consequently, the higher the IEC, the lower the rate of ORR.

4.7 Appendix

4.7.1 *Derivation of Effective Diffusion Coefficient in a Hypothetical Parallel Gas – Liquid Pathways of Equal Volume.*

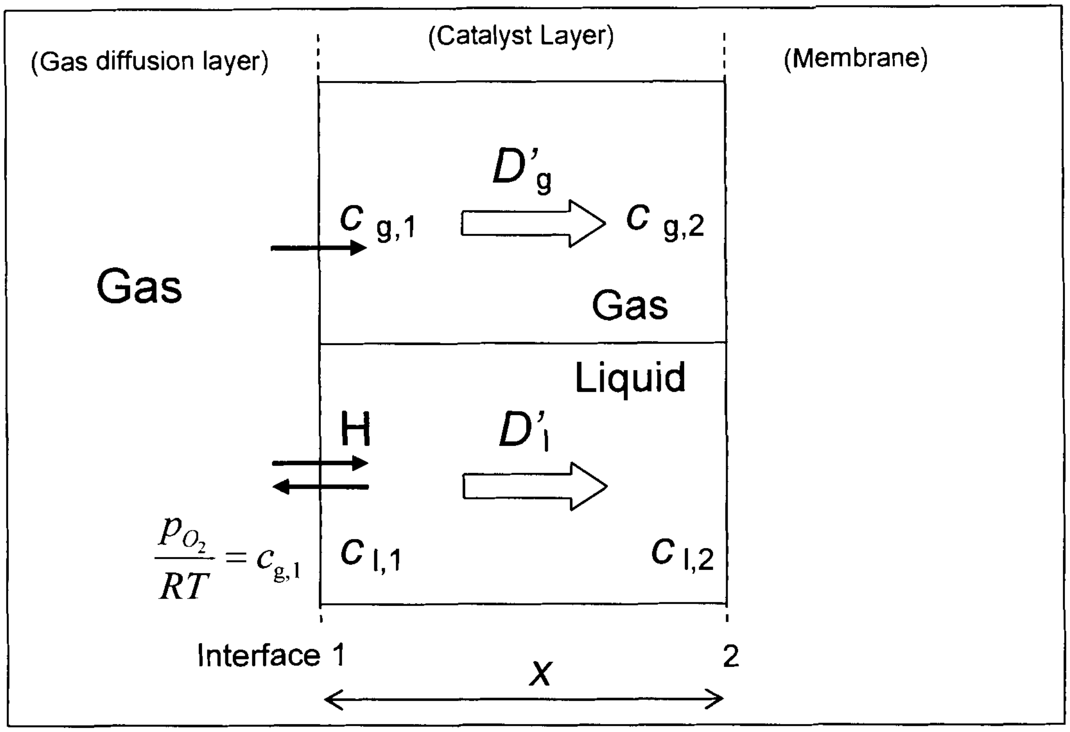

Figure 4.9: Scheme of parallel gas-liquid diffusion pathways.

The flux of oxygen in gaseous phase, liquid phase and total effective flux can be expressed using Fick's law:

$$N_g = -D'_g \frac{dc_g}{dx} \quad (61)$$

$$N_l = -D'_l \frac{dc_l}{dx} \quad (62)$$

$$N_T = -D'^{eff} \frac{dc_g}{dx} \quad (63)$$

The concentration of oxygen is determined from the inlet pressure (Figure 4.9), which can be controlled experimentally. Dissolution of gas at interface 1 is represented by Henry's law.

$$c_l = Hc_g \tag{64}$$

Substituting Equation (A5) into (A3) gives

$$N_l = -D_l^{'} H \frac{\mathrm{d}c_g}{\mathrm{d}x} \tag{65}$$

Total flux is the sum of fluxes in liquid and gas phase

$$N_T = N_g + N_l \tag{66}$$

Solving equation (A7) yields

$$D^{'eff} = D_g^{'} + D_l^{'} H \tag{67}$$

Chapter 5 : Influence of Membrane Ion Exchange Capacity on the Catalyst Layer Performance in an Operating PEM Fuel Cell

5.1 Abstract

The effect of ion exchange capacity (IEC) of polymer electrolyte membranes (PEM) on cathode catalyst layer operation is investigated using a hydrogen/oxygen proton exchange membrane fuel cell (PEMFC) and a series of tetrafluoroethylene-g-polystyrene sulfonic acid (ETFE-g-PSSA) membranes. Analysis of uncompensated resistances in the fuel cell provides information on the state of membrane hydration and catalyst layer operation. Using the agglomerate model, relevant parameters of catalyst layer operation were determined. The steady state beginning-of-life polarization curves show an increase in fuel cell performance with increased IEC. The electrochemically active surface area (ESA) of the catalyst layer reveals a slight dependence on IEC. The latter trend is consistent with previous results for a half-fuel cell system. It is attributed to the membrane determining the extent of wetting in the catalyst layer. The membrane's IEC, controlling morphology and water distribution in it,

regulates the water balance in the complete MEA. This influence is most significant in the cathode catalyst layer, where it affects mass transport and electrochemical characteristics. Comparing half fuel cell and fuel cell systems reveals that the ESA in the latter is lower as a result of reduced wetting of the catalyst layer but this is offset by an order of magnitude improvement of the effective O_2 diffusion. Consequently oxygen reduction reaction (orr) performance is higher in the fuel cell system. The balance between electroosmotic flux and hydraulic counterflux in the membrane is employed to explain the distinct effects of IEC in half fuel cell and fuel cell systems. The two types of measurements, thus, provide a convenient tool to study the interplay of different mechanisms of water flux in the membrane.

5.2 Introduction

Research activities in PEMFC have gained much momentum during the past decade. One particular focus is the development and understanding of proton conducting membrane materials. Although Nafion membranes are widely used and accepted as the industry standard, novel membranes are being developed which provide control and systematic understanding of complex relationships between chemical structure, morphology, physicochemical properties, and electrochemical kinetics. One such class of novel membrane is obtained by radiation-induced polymerization of styrene monomer onto commercial membranes, such as fluorinated ethylene propylene (FEP), poly(vinylidene fluoride) (PVDF) and ethylene tetrafluoroethylene (ETFE), with subsequent sulfonation of polystyrene. Several radiation-grafted membranes have been characterized and evaluated in PEMFC[16,62,65,75-77].

In the membrane electrode assembly (MEA), the proton conducting membrane is sandwiched between two gas diffusion electrodes (GDE). The membrane material must satisfy the following functional requirements: high proton conductivity, good separation of gases between the cathode and the anode, negligible electronic conductivity, and stability. In previous studies[49,50,61,75], it has been demonstrated that, in addition to supporting these requirements, the physicochemical properties of the membrane exert a strong influence on fuel cell electrochemical kinetics.

In recent studies of the oxygen reduction reaction (orr) at Pt microelectrode/membrane interfaces, it has been demonstrated that the fluorocarbon matrix of the membrane enhances solubility of O_2 and improves orr kinetics. The role of the membrane's IEC in this regard has been investigated[75]: for a given class of membrane, decreasing the ion exchange capacity (IEC) results in an increase in hydrophobicity, decrease in water content, higher O_2 solubility, and consequently an increase in orr current in the kinetically controlled region. On the other hand, decreasing the membrane's IEC leads to a reduction in mass transport limited current due to a decrease in O_2 diffusion coefficient and decrease in O_2 permeability.

The role of a membrane's IEC on catalyst layer operation has previously been studied under half-fuel cell conditions[61], an experimental arrangement which simplifies complicating parameters associated with fuel cell studies. It has been shown that in addition to affecting O_2 solubility and mass transport properties, the membrane regulates the water balance and, thereby, the transport of reactant gases in the catalyst layer.

Under the semi-flooded conditions of the half-fuel cell, where the cathode void space is largely filled with liquid H_2SO_4 electrolyte, O_2 diffusion becomes critical for performance. With increasing IEC the ESA slightly increases because of increased "wetting". The slight enhancement in ESA is however offset by the negative impact of reduced O_2 mass transport due to filled pores. Consequently, in the mass transport controlled regime the orr current density decreases with increasing IEC of the membrane. The applicability of these correlations, observed under semi-flooded conditions, to fuel cell research needs further experimental validation.

This work provides a deeper understanding of the role of the membrane's IEC on catalyst layer operation under actual fuel cell conditions. A series of partially fluorinated, radiation-grafted proton conducting membranes based on tetrafluoroethylene-g-polystyrene sulfonic acid (ETFE-g-PSSA) is employed. Relationships between the membrane's physicochemical properties and their influence on fuel cell electrochemical kinetics are discussed. A comparison between electrochemical parameters extracted under half-fuel cell[61] and fuel cell conditions (this work) provides insight into the state of hydration of the catalyst layer and effective use of Pt in MEAs. The advantages and disadvantages of the two electroanalytical approaches are discussed. Different trends for the effect of IEC on orr polarization are observed under half fuel cell and fuel cell conditions. This apparent discrepancy can be resolved considering the interplay between electroosmotic drag and hydraulic counterflux in the membrane. In fact, it will be shown, how the combination of half-fuel cell and fuel cell measurements can be used to discriminate the different mechanisms of water flow in the membrane.

5.3 Experimental

5.3.1 Membranes

Five ETFE-*g*-PSSA membranes (E1 to E5) having different graft weights (26.4 to 46 wt%) were used. These membranes were similar to those used in the previous chapter (membranes M1 to M4) but were obtained from different batches. Thus, they were assigned with different sample names. Measurements of IEC, proton conductivity and water content were performed in this investigation using the procedure described in section 3.1.3 and 3.1.4. Nafion® 117 membrane (DuPont) was used for comparison. All membranes were pretreated (section 3.1.2).

5.3.2 Gas Diffusion Electrodes

In order to directly compare the roles of membrane's IEC under half-fuel cell and fuel cell conditions, GDEs of similar specification to those used in the half-fuel cell study were required. A GDE containing 0.75 mg Pt cm^{-2} (20wt% Pt/Vulcan XC-72) and 20 wt% impregnated Nafion was fabricated following the procedure in Section 3.2.2. Using this procedure, catalyst particles are distributed homogeneously on the electrode as shown in section 3.2.3.

The fabricated GDE has slightly lower Pt loading than those used in the half-fuel cell investigation (0.78 mg Pt cm^{-3}). It is noted, however, that because many factors interplay during fabrication of GDE, reproducibility between batches to the precision better than ± 0.03 mg Pt cm^{-2} was difficult to achieve when performed manually. A large piece of GDE (12 x 15 cm^2) was fabricated and small pieces (2.3 x 2.2 cm^2) used for making MEAs were cut.

5.3.3 Fabrication of MEAs

The series of ETFE-g-PSSA membranes (E1, E2, E3, E4 and E5) with different IEC (3.22, 2.73, 2.38, 1.95 and 0.75 mmol g^{-1}) and Nafion 117 (N, 0.91 mmol g^{-1}) were used to fabricate MEAs. The gas diffusion electrodes (2.2 x 2.3 cm^2) were cut from the same batch. Individual membranes were placed between the electrocatalyst side of two GDEs and the membrane/electrode/membrane unit was hot-pressed at 220 kg cm^{-2} and 150 C for 90 seconds. Prior to assembling into the fuel cell apparatus, MEAs were equilibrated in water at 60°C for 10 minutes. It is noteworthy that the equilibration step serves two purposes. Firstly, the hydration process accelerates membrane equilibration and MEA conditioning in the fuel cell. This has recently been reported by Qi and Kaufman[132]. Secondly, the equilibration process enables the membrane to expand prior to assemblage. For many novel membrane materials, where optimization of mechanical strength is not fully considered, the equilibration process minimizes the risk of membrane rupture in the fuel cell due to rapid expansion when the MEA is humidified. The membranes used in this study exhibit considerably higher water uptake and mechanical expansion than Nafion, and thus, the equilibration step was essential.

5.3.4 Fuel Cell

MEAs were tested in 5 cm^2 serpentine pattern flow single cell hardware connecting to a test station, as described in section 3.4. The fuel cell was operated at 25 °C and ambient pressure. The anode and the cathode were fully humidified at 40 °C (~ 95% R.H.). Flow rates were set variably at 20 ml min^{-1} A^{-1} in addition to a base flow rate of 30 ml min^{-1}. These rates corresponded to variable stoichiometries of close to 14 - 1.8 for H_2 and 28 - 3.6 for O_2 when the cell is operated at a current density of 0.2 to 1.0 A cm^{-2}. The current-dependent flow rate (20 ml min^{-1} A^{-1}) was used to minimize excessive stoichiometric flow at low current density, which could potentially cause dehydration of the membrane[133]. After assembly, the cell's open circuit potential (OCP) was monitored for ~30 minutes until the response became stable. Galvanostatic steady state polarization was performed between the potential range ~ 1.05 V (OCP) to 0.30 V. After each change of current, a period of 45 seconds was allowed for the cell to stabilize. It was found that for a 5 cm^2 cell, the stabilization times of 30, 45, 60 and 90 seconds did not produce significantly different polarization results ($\pm$ 2%). The polarization measurement was repeated 3-4 times to ensure that the polarization data represents steady state beginning of life (BOL) performance.

The electrochemically active surface area was measured by CO adsorption followed by CO oxidation. The cathode was purged with N_2 and the potential was cycled (30 - 50 cycles) between 1.30 and 0.05 V at 30 mV s^{-1} until a steady response was obtained. The flow of N_2 gas was stopped and CO gas was fed to the cathode at a constant flow rate of 50 ml min^{-1} and the potential was held at 0.125 V for 3 minutes to allow CO adsorption onto Pt site. The cathode was purged with N_2 for 5 minutes to remove excess CO and the potential cycled between 0.05 to 1.30 V at 5 mV s^{-1} for 3 cycles.

5.3.5 Current Interruption

During a fuel cell operation, the potential loss due to the uncompensated resistance (R_u) can be measured by the current interruption technique. At a given electrode potential, when the current is interrupted by rapidly disconnecting the electronic load, the potential transient consists of a fast decay component (iR_u) and a slow electrochemical component (E_{DL}), as described in section 4.3.5. An ideal response of a potential transient after a current interruption is illustrated in Figure 5.1. The iR_u component, whose decay time is estimated to be less than 1 ns [134], vanishes almost immediately, whereas the relaxation of E_{DL} occurs at a considerably slower rate (1 – 30 μs). iR_u can be measured from the difference between the electrode potential immediately before and after the interruption.

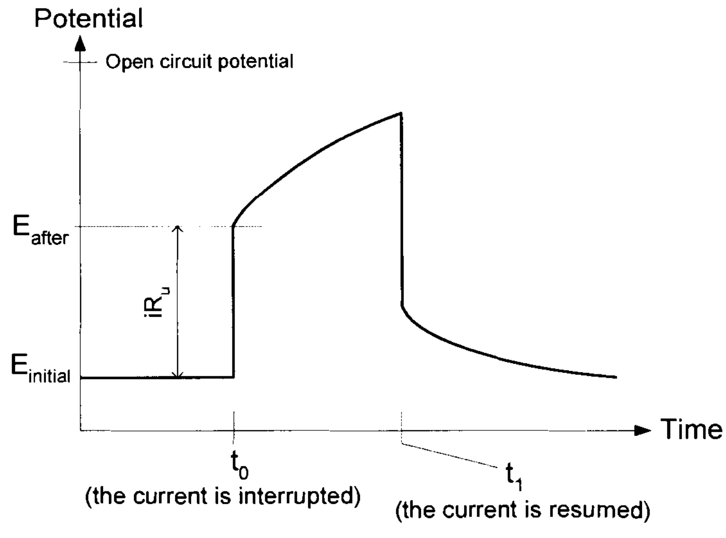

Figure 5.1: An ideal potential transient response after a current interruption. Before an interruption, the cell is operated at a constant current. iR_u is determined from the electrode potential before ($E_{initial}$) and after (E_{after}) an interruption.

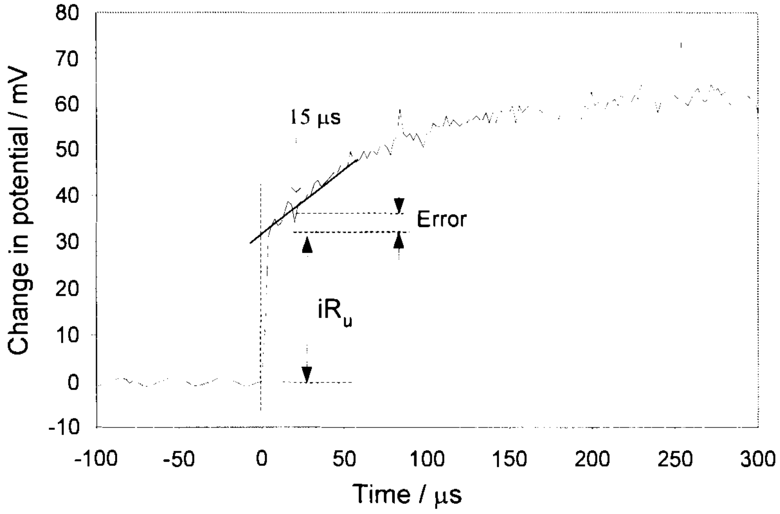

Figure 5.2: A typical current interruption profile. Data shown is from MEA-1 operated in a fuel cell at 25 ^{0}C, 0.67 V and 0.52 A. Resolution = 2 μs (the effect of potential overshoot at t < 200 ns is not shown).

In practice, the potential transient recorded from fuel cells exhibit non idealized features[134]. Immediately after the current interruption, a potential overshoot takes place ($0 < t < 200$ ns [134]), followed by oscillations ($0 < t < 5$ μs [135]). These effects are thought to originate from the inductance and some interferential noises from the electrical circuitry[86,134,136]. Because of these effects, selecting the sampling time for measuring E_{after} requires some considerations. If E_{after} is measured too early (< 5 μs), the accuracy is compromised because of the overshoot and the oscillations. Measuring it too late leads to a systematic overestimation because the electrochemical relaxation has already begun. Alternatively, instead of using a single potential point, the accuracy may be improved by measuring two potential points between t_0 and t_1, and linearly extrapolating the data to obtain E_{after} at t_0. A typical current interruption profile captured by using a digital oscilloscope (TDS-320, Tektronix) is illustrated in Figure 5.2.

In this investigation, the uncompensated resistance, R_u, was estimated using a built-in current interrupter circuitry in the electronic loadbank (Scribner Associates 890B) controlled by FuelCell® data acquisition software (Scribner Associate Inc). During the fuel cell operation, the software continuously determined the values of iR_u by measuring $E_{initial}$ and E_{after}. The potential overshoot and oscillations, which were the characteristics of the electronic circuitry and the experimental setup, were found to be minimal at 10 - 15 μs after a current interruption. In order to minimize the interference of the overshoot and oscillation effects, E_{after} was measured at 15 μs. By repetition of experiments at various conditions, it has been reported that the E_{after} determined at 15 μs contained ~10% overestimation when compared to E_{after} obtained from the extrapolation method[135]. The overestimation was corrected for by the software. For a given potential point, multiple values of iR_{u} were determined and the average value was reported.

5.3.6 Fitting of Electrochemical Data to the Agglomerate Model

The agglomerate model used for analyzing PEMFC cathodes was adapted from the earlier works of Perry *et al.*[89] and Jaouen *et al.*[90], and has been reported in ref.[61] and [88]. The fourth order Runge-Kutta method using MATLAB software was used to solve the model. The cathode potential is assumed to be the same as the iR_{u}-corrected cell potential. This is based on the assumption that the anode overpotential is negligible compared to the cathode overpotential. This assumption may no longer be valid at high current densities when anode dehydration of some MEAs is significant (see section 5.4.4). For this reason, only polarization data in the low current density region (< 50 mA cm^{-2} and in the potential range between OCP and 0.75 V) were used for curve fitting. For MEA-1, MEA-2 and MEA-N, it is quite clear that the dehydration of membrane, and thus, of the anode was not significant within this region (see section 5.4.3 below). This supports the assumption of negligible anode overpotential. For MEA-3, MEA-4 and MEA-5, on the other hand these trends are slightly impaired by effects of anode and membrane dehydration, i.e. the anode overpotential may not be negligible. The use of a stable reference electrode setup was not available to verify our assumption. Nevertheless, the contributions of the anode overpotential in the low current density region are assumed to be small compared to the cathode overpotential. The real cathode overpotentials, including effects of anode dehydration, will be slightly smaller than the values considered here.

The base-case conditions listed in Table 5.1 were used to compute the total current density, protonic current density and O_2 concentration distribution. These base-case parameters were kept constant throughout fitting of the model to the experimental data. The reference solubility of oxygen (c_o^{ref}), defined as the position independent concentration of oxygen dissolved at the surface of the agglomerate in equilibrium with 1 atm pressure of gaseous O_2 in the catalyst layer at open circuit potential; the effective diffusion coefficient of O_2 in the gas diffusion layer (D_{GDL}^{eff}); and the effective O_2 diffusion coefficient in the catalyst layer (D_{CL}^{eff}) were variable parameters. Attempts to fit the agglomerate model to the experimental results using D_{GDL}^{eff} and D_{CL}^{eff} as the only two variable parameters were unsatisfactory. The three variable functions (D_{GDL}^{eff}, D_{CL}^{eff} and c_o^{ref}) were adjusted using the non-linear least squares fitting method.

Table 5.1: Base-case parameters of the agglomerate model for fitting the fuel cell iR_u compensated polarization curves

Input parameters	Value
Cell temperature (T)	298 K
Cathode oxygen pressure (P)	1 atm
Cathode transfer coefficient (α_r)	0.58
Diffusion coefficient of O_2 in Nafion®[7] (D_N)	0.6×10^{-5} cm^2 s^{-1}
Oxygen Henry's constant (K)[7]	14
Proton bulk conductivity (σ_b)	0.07 S cm^{-1}
Active layer thickness (L)	50 μm
Active layer porosity (ε_c)	0.55
Agglomerate radius (R_a)	2.5 μm
Gas phase diffusion coefficient of O_2 ($D_{O_2,g}$)	0.227 cm^2 s^{-1}
Gas diffusion layer thickness (L_{GDL})	350 μm
Exchange current density (i_o)*	3.0, 0.2, 1.0, 0.8, 0.4 and 0.5 mA m^{-2}

* Listed value for MEA-1, MEA-2, MEA-3, MEA-4, MEA-5 and MEA-N, respectively.

5.4 Results

The physicochemical properties of ETFE-g-PSSA and Nafion membranes used are listed in Table 5.2. As previously reported[75], proton conductivity increases with IEC, water content and $[H_2O]/[SO_3^-]$ (λ) ratio. The electrochemical kinetics of MEAs prepared using these membranes are discussed below.

Table 5.2: Physicochemical properties of ETFE-g-PSSA (E1-E5) and Nafion 117 membranes

Membrane	IEC (mmol g^{-1})	Water content (wt%)	$[H_2O]/[SO_3^-]$	σ_b (S cm^{-1})	Wet thickness (μm)
E1	3.22	60	28	0.19 + 0.01	127 + 4
E2	2.73	53	24	0.16 + 0.01	115 + 3
E3	2.38	48	21	0.14 + 0.01	93 + 4
E4	1.95	42	19	0.12 + 0.02	85 + 5
E5	0.75	17	10	0.03 + 0.01	68 + 3
N117	0.91	19	13	0.08 + 0.01	200 + 3

5.4.1 Electrochemically Active Surface Area (ESA)

A typical cyclic voltammogram following CO adsorption onto Pt for an MEA is shown in Figure 5.3. A well-defined CO oxidation peak at ~ 0.80 V is observed. Adsorbed CO is oxidized and removed during the first potential cycle. Subsequent cycles show no trace of CO oxidation. The electrochemically active area was determined by integration of the anodic faradaic current peak for CO oxidation using 420 μC cm-2 Pt as the conversion factor[12]. The electrochemically active surface areas of all MEAs are listed in Table 5.3 and plotted in Figure 5.4. The measurements were repeated 3-4 times and the errors for all MEA samples were estimated to be + 7-10 %. This is shown as the error bars in Figure 5.4. The estimated uncertainty is typical for the ESA measurements[137].

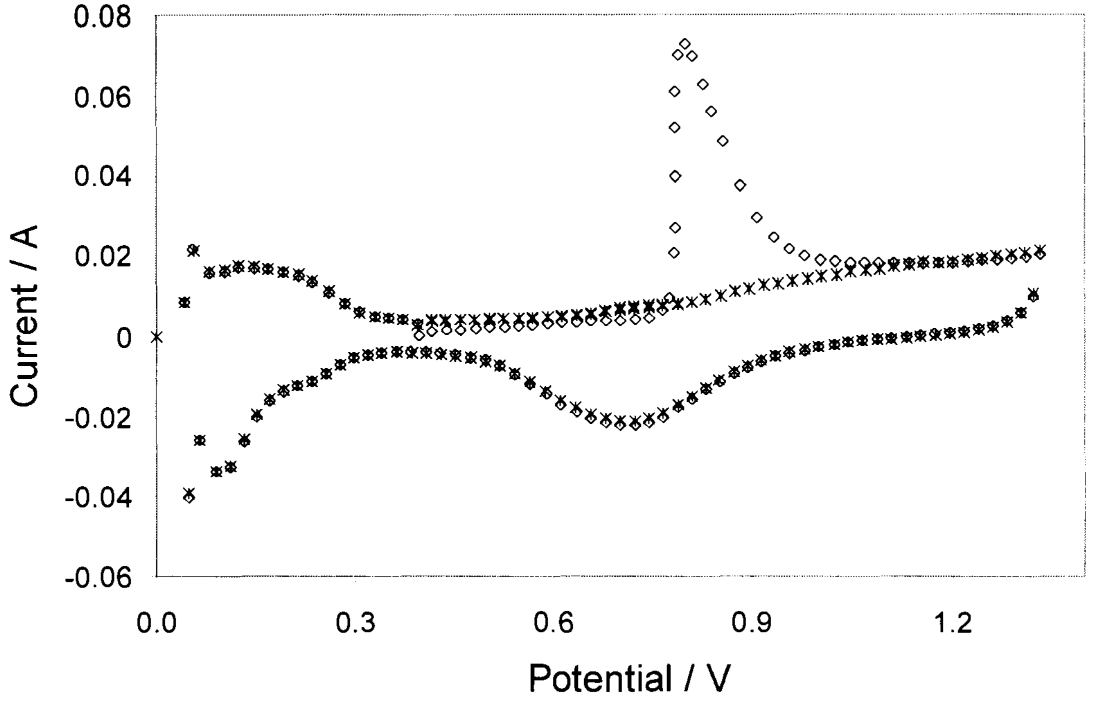

Figure 5.3: Cyclic voltammogram of MEA-B at 25°C and ambient pressure. Fully humidified N_2 and H_2 flow rates of 30 ml min^{-1} to the cathode and the anode, respectively.

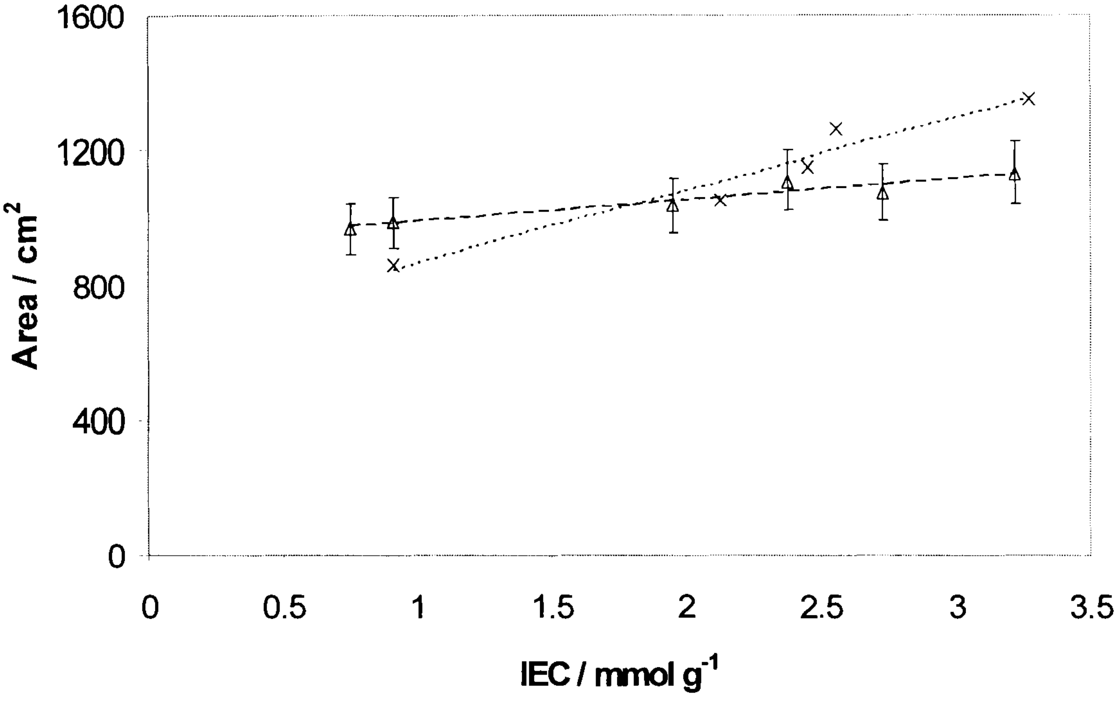

Figure 5.4: Plot of the electrochemically active surface area (cm^2) determined by CO-oxidation versus membrane's IEC for all MEA samples. ESA measured in the fuel cell (Δ, this work) and the half-fuel cell (X, data taken from Chapter 4). The dash lines indicate the best linear fits for fuel cell (70 cm^2 g mmol^{-1}) and half-fuel cell (250 cm^2 g mmol^{-1}) data.

Table 5.3: Electrochemically active surface areas and Pt utilization for MEAs

Sample (IEC / mmol g^{-1})	ESA (cm^2)	Pt Utilization	Sample* (IEC / mmol g^{-1})	ESA* (cm^2)	Pt Utilization
MEA-1 (3.22)	1130	0.30	HMEA-1 (3.27)	1350	0.50
MEA-2 (2.73)	1075	0.28	HMEA-2 (2.56)	1260	0.47
MEA-3 (2.38)	1109	0.29	HMEA-3 (2.45)	1150	0.43
MEA-4 (1.95)	1035	0.27	HMEA-4 (2.13)	1050	0.39
MEA-5 (0.75)	964	0.25	-		
MEA-N (0.91)	984	0.26	HMEA-N (0.91)	860	0.32

* Half-membrane electrode assembly (HMEA) data are obtained in half-fuel cells, ref.[61].

The active surface area determined by adsorption-desorption of CO corresponds to the surface area of Pt that is in direct contact with the electrolyte. Under the fuel cell operating conditions, the “wetted Pt surface area” is influenced by many factors, namely the cell design, operating conditions, composition of the catalyst layer and water content of the bulk membrane since it is in direct contact with the ionomer impregnated catalyst layer. As shown in Figure 5.4, a slight increase in ESA and Pt utilization is observed with an increase in the membrane’s IEC. The dependence of ESA on IEC is quantified, by fitting a linear slope, to be 70 cm^2 g mmol^{-1}. In contrast, a much stronger dependency of 250 cm^2 g mmol^{-1} was found when measured under half-fuel cell conditions[61].

Pt utilization values listed in Table 5.3 were calculated by normalizing the ESA by a factor of 3795 cm^2 Pt per GDE (0.75 mg Pt cm^{-2} loading times 5.06 cm^2 GDE area times 1000 cm^2 mg^{-1} approximate specific surface area for 20 wt% Pt/Vulcan XC-72 [43,133]). Pt utilizations of MEAs containing ETFE-g-PSSA vary between 25-30 %, which is significantly lower than measured in half-fuel cell apparatus (39-50%). This indicates that the extent of flooding of the catalyst layer in the fuel cell should be lower than in the half-fuel cell (> 70% of void space is filled with water[61]). This effect is likely to be manifested by an increase in the gas transport rates to the reactive sites for fuel cell MEAs compared to the half-MEAs studied in half-fuel cells.

5.4.2 Polarization Curves

The galvanostatic steady state polarization curves for all MEAs are shown in Figure 5.5. The open circuit potential (OCP), listed in Table 5.4, were recorded at zero flow rates while H_2 and O_2 are trapped in the cell. The OCP for all MEAs are in the range 0.90 to 1.0V, which indicates no significant fuel crossover through the MEA[16]. For MEAs containing ETFE-g-PSSA membranes, a clear trend of increasing polarization performance with increasing membrane IEC is observed. The trend is most apparent in the potential range corresponding to the Ohmic and mass transport controlled regions (0.40 - 0.70V). The higher proton conductivity of the higher IEC membranes may partly explain this trend. However, MEA-N displays a higher performance than most of the MEAs despite Nafion 117 possessing much lower proton conductivity than ETFE-g-PSSA (with the exception of E5). Thus other factors play a significant role in determining the observed fuel cell performance. Current interruption method and EIS techniques are employed in order to subtract voltage losses in the membrane from the overall performance of the fuel cell.

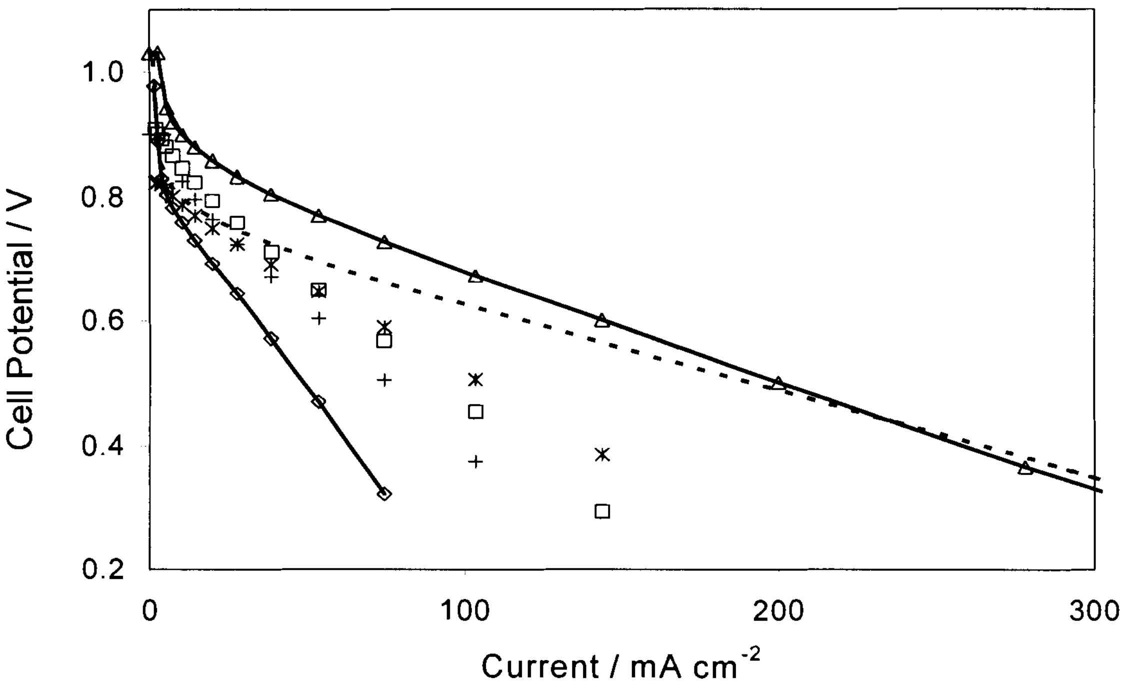

Figure 5.5: Steady state fuel cell polarization curves without iR_u compensation, operated at 25 °C, ambient pressure and 40 °C humidification temperature for the cathode and the anode. MEA-1 (△), MEA-2 (✳), MEA-3 (□), MEA-4 (+), MEA-5 (◇) and MEA-N (---).

Table 5.4: Electrochemical properties of MEAs [(a)]

Sample (IEC / mmol g-1)	OCP / V	R_u / Ω cm^2	R_m / Ω cm^2	R_i / Ω cm^2
MEA-1 (3.22)	1.034	0.302	0.066	0.236
MEA-2 (2.73)	0.962	0.592	0.074	0.518
MEA-3 (2.38)	0.948	0.965	0.064	0.901
MEA-4 (1.95)	0.919	1.010	0.064	0.946
MEA-5 (0.75)	0.978	1.280	0.267	1.013
MEA-N (0.91)	1.021	0.247	0.242	0.005

(a) Open circuit potential (OCP), uncompensated resistance (R_u) measured at 20 mA cm^{-2}, membrane protonic resistance (R_m) and calculated interfacial resistance (R_i).

5.4.3 Uncompensated Resistance

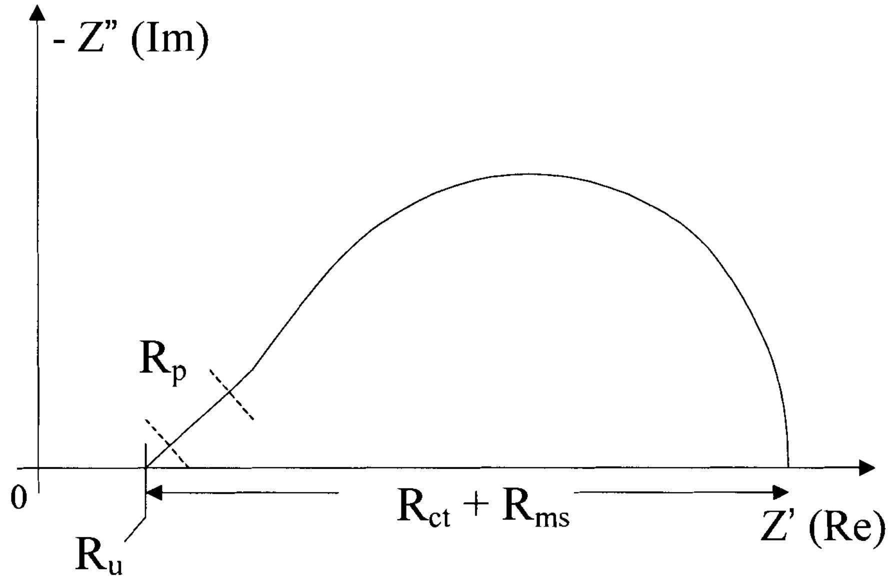

Figure 5.6: A schematic diagram of a simplified Nyquist plot for a PEMFC cathode derived from an equivalent circuit in ref. [138]. Uncompensated resistance (R_u), proton resistance in the impregnated ionomer (R_p), charge transfer resistance (R_{ct}) and mass transport resistance (R_{ms}).

A typical EIS Nyquist plot, depicted in Figure 5.6 contains a fast potential response component (pure resistor type behaviour) and a slow response (resistive capacitance, RC-type behaviour). The high frequency intercept on the real axis (Z') corresponds to uncompensated resistance, R_u. The slower response components, containing contributions from the proton resistance in the catalyst layer (R_p), the charge transfer resistance (R_{ct}) and the mass transport resistance (R_{ms}), give rise to the characteristic semi-circle. Note that although the EIS technique can be employed to measure R_u (as described in Section 4.3.5), the current interruption method is preferred because the measurements may be performed simultaneously with the polarization measurements. It was found that R_u obtained from the two methods were in reasonable agreement ($\pm$10 %), which supports the recently reported comparison of the current interruption and EIS techniques by Andreaus et. al.[86].

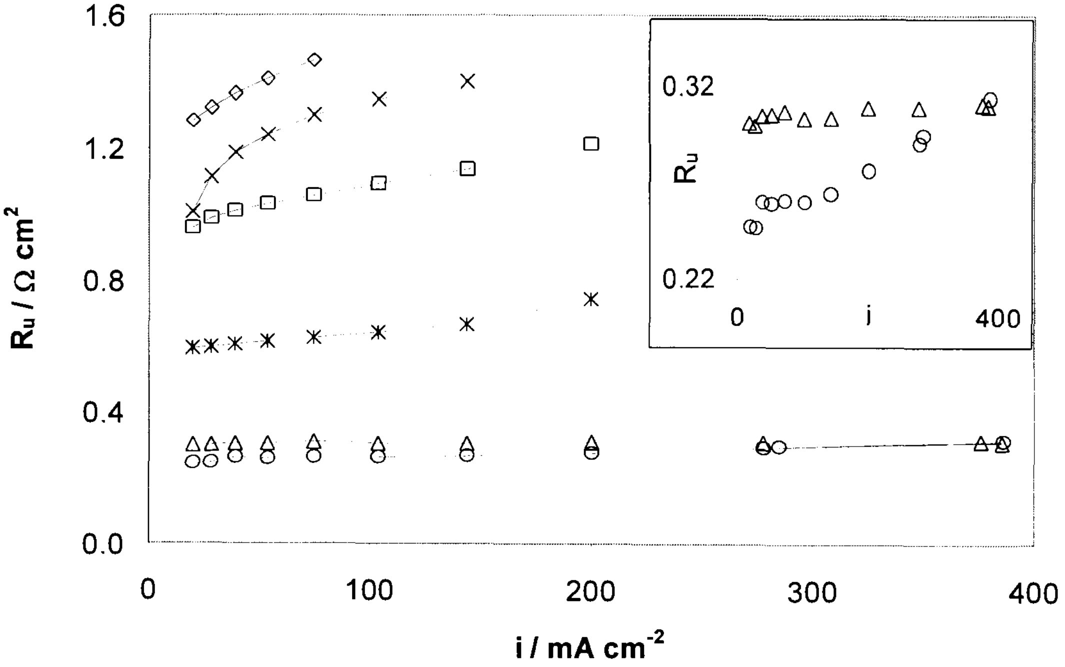

Figure 5.7: Plot of uncompensated resistance versus current density at 25 °C, ambient pressure and 40 °C humidification temperature for the cathode and the anode. MEA-1 (△), MEA-2 (✳), MEA-3 (□), MEA-4 (X), MEA-5 (◇) and MEA-N (O). Inset: expanded plot for MEA-1 and MEA-N.

In order to gain further insights into the anomalous performance of MEA-N observed in the polarization curves, R_u for all MEAs obtained at various current densities are plotted in Figure 5.7. R_u consists of the bulk membrane proton resistance (R_m) and the contact resistance in the MEA (R_c), as indicated in equation 68.

$$R_u = R_m + R_c \qquad (68)$$

When the current density increases, R_u is observed to increase slightly (see inset of Figure 5.7). This observation has been observed previously[86] for Nafion based MEAs and is attributed to a decrease in the membrane hydration as a result of increasing electro-osmotic drag with increasing current density.

5.4.4 Effect of Membrane Dehydration

MEAs containing ETFE-g-PSSA membranes show an increase in R_u with decreasing IEC. For MEA-N, and MEA-1, R_u is relatively constant throughout the current range. In contrast, MEA-2, MEA-3, MEA-4 and MEA-5 show a significant increase in R_u at high current densities. The dependency of R_u on current density has been observed by Horsfall and Lovell[62] for MEAs operating at 80°C. In ref. [62], it is reported that a MEA containing ETFE-g-PSSA membrane (IEC = 2.235 mmol g^{-1}) showed no significant change in its resistance at high current density of up to 1.8 A cm^{-2}. They also observed, in the case of a MEA-containing Nafion 115, a steady increase in R_u with increasing current density, which was attributed to membrane dehydration. Andreaus et. al. investigated the dependency of R_u on current density[86,109] and concluded that, for higher current density, the water content on the anode side of the electrolyte decreases due to dehydration – a problem compounded by electroosmotic drag and poor backtransport of water to the anode. In this work, the increase in R_u with increasing current density supports previous hypotheses that MEAs containing lower IEC membranes have less effective backtransport of water. This leads to membrane dehydration. When the anode hydration was increased by increasing humidification temperature from 40 to 50 °C, significant performance improvements were observed for MEA-4 and MEA-5, see Figure 5.8. Providing more water at the anode improves the membrane's proton conductivity and reduces anode overpotential. No significant performance changes were observed for other MEAs. It is noteworthy that all MEAs operated at higher cathode humidification temperature (50 °C), i.e. providing more water to the cathode, did not show significant improvements in performance.

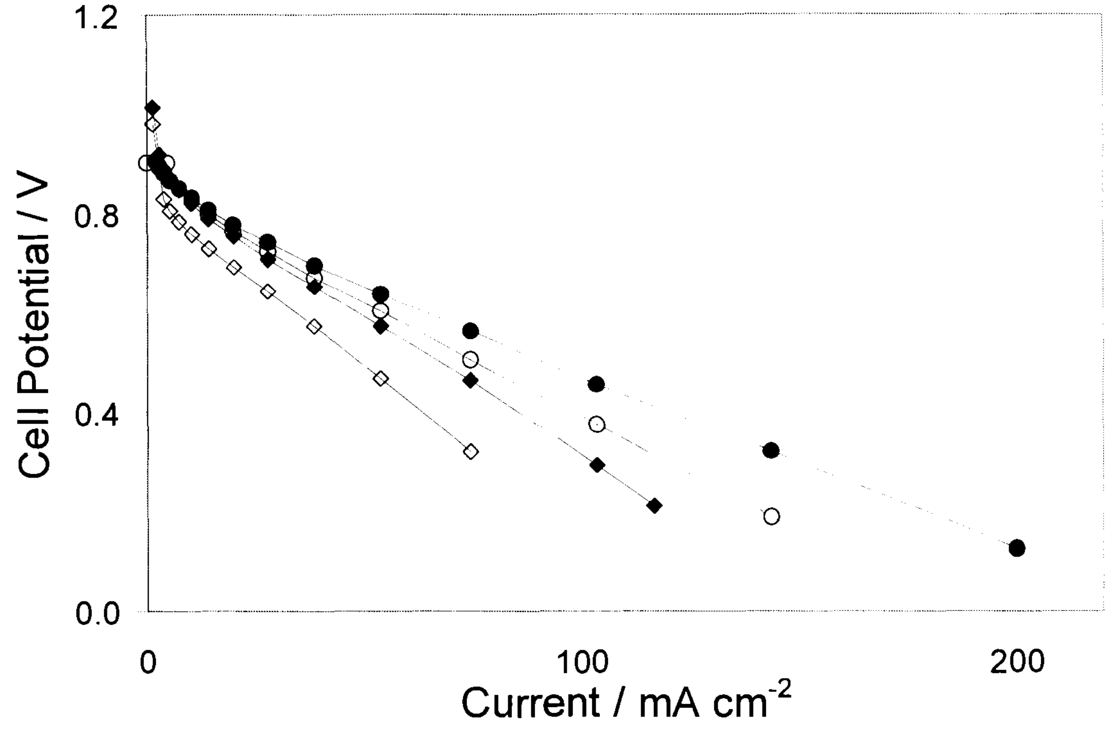

Figure 5.8: Effect of increasing anode hydration by increasing the humidification temperature of anode from 40 (MEA-4 (O) and MEA-5 (◇)) to 50 °C (MEA-4 (•) and MEA-5 (♦)). The fuel cell was operated at 25 °C and ambient pressure.

5.4.5 Effect of Interfacial Resistance

For MEA-N, R_u (~ 0.24 Ω cm^2) is almost the same as the protonic resistance of hydrated Nafion 117 (~0.25 Ω cm^2), hence there is no significant contact resistance. Under conditions of low current density, no significant membrane dehydration is expected. Nevertheless, R_u for ETFE-g-PSSA based MEAs are significantly higher than the calculated membrane resistance, R_m, as shown in Table 5.4. Contact resistance is, thus, considered to be the predominant contribution to R_u. R_c consists of two components: an electronic contact resistance (R_e) and a protonic membrane/catalyst interfacial contact resistance (R_i),

$$R_c = R_e + R_i \tag{69}$$

The composition of the GDEs and compression of the fuel cell fixtures, two critical parameters determining R_e, were the same for all MEAs. Furthermore, R_e for MEA-N is calculated to be negligible. Therefore, R_e for all MEAs should be negligible.

The protonic interfacial contact resistance (R_i) represents the resistance of proton transfer at the interface between the catalyst layer, impregnated Nafion ionomer, and the bulk membrane. R_i is thought to originate from a weak physical or chemical interfacial contact. In the case of MEA-N where R_i is negligible, bonding of Nafion ionomer and Nafion bulk membrane is chemically favourable. Hot-pressing at 150°C, which corresponds to the processing temperature of Nafion, facilitates formation of good interfacial adhesion. Experimentally, this is supported by the observation that the membrane / GDE interface remains intact after extensive testing in a fuel cell. In the case of ETFE-g-PSSA based MEAs, where R_i is significant, incompatibility between the impregnated Nafion ionomer and the ETFE-g-PSSA membranes has been reported[62,76].

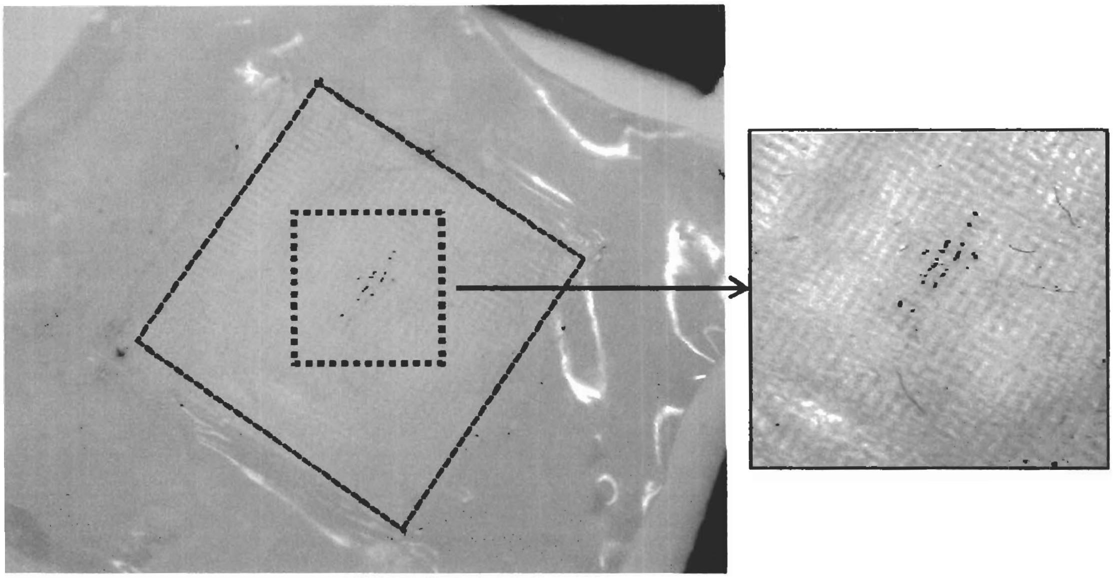

Figure 5.9: Photographic illustration of complete delamination of MEA-4 illustrating the membrane / GDE adhesion failure mode occurs at the membrane / catalyst layer interface. The membrane / GDE contact area (outlined center) shows imprinting of carbon cloth pattern on the membrane.

In the present work, ETFE-g-PSSA based MEAs, when disassembled after ~ 48 hours of fuel cell testing were found to delaminate. Delamination occurred mostly around the perimeter of the GDEs. Upon drying, all ETFE-g-PSSA based MEAs delaminated completely. Delamination occurred at the membrane/catalyst layer interface -the catalyst layer remained well bonded to the GDE, as shown in Figure 5.9. From Table 5.4, R_i is observed to decrease with increasing IEC of the membrane. It is believed that the increase in hydrophilicity due to higher IEC provides better interfacial contact with the catalyst layer and consequently improves adhesion. The MEA fabrication technique, originally optimized for Nafion membranes, may not be optimal for the ETFE-g-PSSA membranes and a modification of MEA fabrication conditions may improve membrane / catalyst layer adhesion. However, modifying the MEA fabrication conditions to suit individual membranes would introduce additional experimental variables; for the purpose of this study we simply compensate for differences in R_i mathematically (see section 5.4.6). After eliminating R_u from our polarization data we can focus on the evaluation of mass transport and electrochemistry in the catalyst layer, having excluded effects of the membrane resistance, membrane dehydration and interfacial contact resistance.

5.4.6 iR_u Compensated Polarization

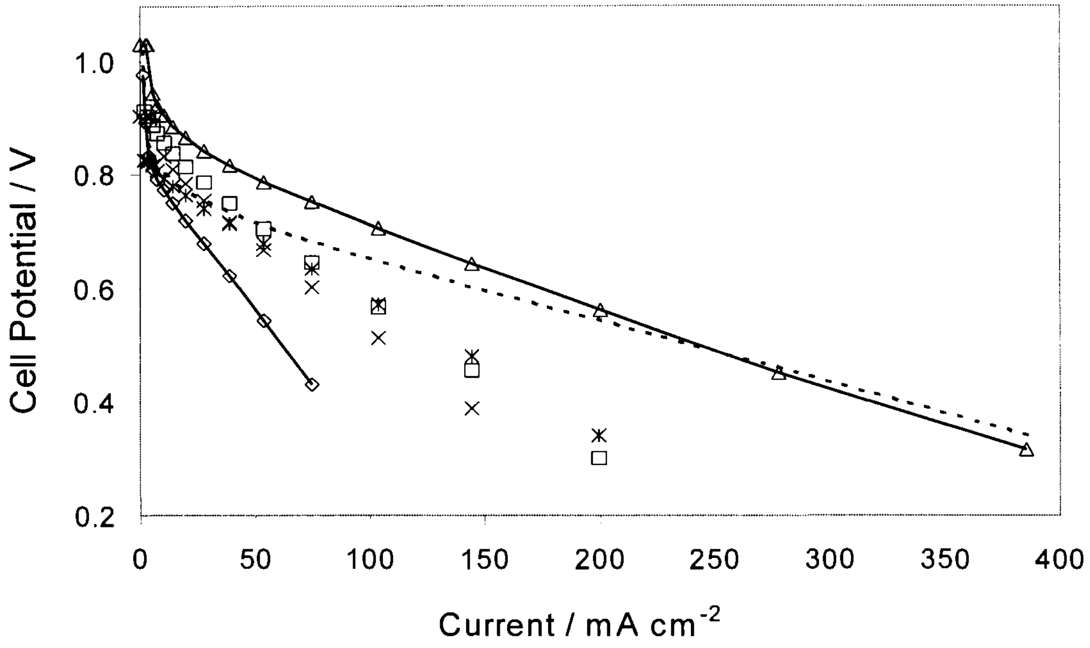

Figure 5.10: Steady state fuel cell polarization curves with iR_u compensation, operated at 25 °C, ambient pressure and 40 °C humidification temperature for the cathode and the anode. MEA-1 (△), MEA-2 (✳), MEA-3 (□), MEA-4 (+), MEA-5 (◇) and MEA-N (---).

iR_u compensated polarization curves, shown in Figure 5.10, represent polarization data that are free of membrane and contact resistances. The trend of increasing fuel cell performance with increasing IEC of the membrane is observed and MEA-N is again an anomalously good performer if IEC alone is considered. This provides further evidence that the slow potential response component in EIS, which consists of charge transfer resistance (R_{ct}), proton transport resistance in the catalyst layer (R_p) and mass transport resistance (R_{ms}), is the reason for the higher performance of Nafion. EIS theory applied to the PEMFC cathodes[138] is used to estimate R_p. A description of the calculation is provided in Section 5.7.1 and the values of R_p for all MEAs, are listed in Table 5.5. R_p is calculated to be very similar for all MEAs (0.56 + 0.07 Ω cm^2). This is an expected result since all catalyst layers contain the same amount of Nafion with similar humidification. It is therefore justifiable to rule out R_p as a cause of the trend observed in Figure 5.10.

Table 5.5: Electrode capacitance (C_{dl}), proton resistance in the catalyst layer (R_p) and effective proton conductivity in the catalyst layer (σ^{eff}) for various MEAs

	slope $\left(\sqrt{\frac{R_p}{C_{dl}}}\right)$ (a)	C_{dl} (mF cm^{-2}) (b)	R_p (Ω cm^2) (c)	σ^{eff} (mS cm^{-1}) (d)
MEA-1 (3.22)	0.362	91	0.60	8.3
MEA-2 (2.73)	0.352	90	0.56	8.9
MEA-3 (2.38)	0.370	88	0.61	8.2
MEA-4 (1.95)	0.353	86	0.54	9.3
MEA-5 (0.75)	0.363	83	0.56	9.0
MEA-N (0.91)	0.358	77	0.50	10.1

(a) Obtained by plotting $|Z|$ against $\omega^{-1/2}$. *(b)* Determined by cyclic voltammetry. *(c)* Estimated from the measured slope ($\sqrt{\frac{R_p}{C_{dl}}}$). *(d)* Calculated form R_p.

The effective proton conductivity in the catalyst layer (σ^{eff}), calculated from R_p lies between 8.2 and 10.1 mS cm^{-1}, which is ~10% of the conductivity of bulk Nafion membrane (80 mS cm^{-1}). This is a reasonable result since the 20 wt%

Nafion content in the catalyst layer accounts for 0.10 volume fraction in the catalyst layer. The result is also in good agreement with the experimentally measured value reported by Springer et. al.[97].

The increase in iR_u-compensated polarization performance with increasing IEC of the membrane is considered to be influenced by charge transfer and mass transport resistances in the cathode catalyst layer. The IEC controls the water balance in the catalyst layer. The ability of the membrane with high IEC to facilitate water backtransport helps remove water more effectively from the cathode thus improving O_2 mass transport. The influence of the membrane on performance of the catalyst layer is further discussed in section 5.5.3.

5.5 Discussion

5.5.1 Mass Transport Parameters in the Catalyst Layer

Mass-transport properties extracted by fitting the agglomerate model for the cathode to the experimental results are reported in Table 5.6. The reference concentration (c_o^{ref}), which corresponds to the O_2 concentration at the agglomerate surface, is calculated to be between 2.0 and 3.9 mmol l^{-1} for all MEAs. c_o^{ref} is by definition equivalent to the solubility of oxygen at the Pt-membrane interface. The values of c_o^{ref} are in good agreement with those obtained from the recently reported work using half-fuel cells [9] and are 1/4 to 1/2 the solubility of oxygen dissolved in the ETFE-g-PSSA as determined by the Pt-microelectrode technique[75]. The difference is attributed to lower volume fraction of Nafion in the catalyst layer due to the presence of Pt/C compared to the bulk membrane.

The effective diffusion coefficient in the GDL is calculated to be ~ 10^{-3} cm^2 s^{-1}, which is two orders of magnitude lower than free gaseous diffusion (10^{-1} cm^2 s^{-1}); but two orders of magnitude higher than D_{CL}^{eff}. This indicates significant gaseous diffusion through mesoporous and macroporous void space – an expected result since the GDL is wet-proofed. The D_{GDL}^{eff} values obtained from the fuel cell are approximately the same as those obtained from the half-fuel cells.

Table 5.6: List of parameters derived from fitting the agglomerate model (a) and percolation theory (b) to the experimental results

Sample (IEC)	$10^{-3}\ D_{\mathrm{GDL}}^{\mathrm{eff}}$ ($cm^2\ s^{-1}$)	$10^{-5}\ D_{\mathrm{CL}}^{\mathrm{eff}}$ ($cm^2\ s^{-1}$)	$c_{\mathrm{o}}^{\mathrm{ref}}$ (mmol l^{-1})	10^3 Error(d)	V_l / v_v
MEA-1	1.2	7.86	2.31	2.4	0.58
MEA-2	1.0	5.32	2.16	5.3	0.61
MEA-3	1.1	4.43	2.07	6.5	0.62
MEA-4	1.0	2.48	2.09	4.7	0.65
MEA-5	0.4	1.05	1.98	8.4	0.68
MEA-N	1.4	5.08	3.82	1.7	0.61
HMEA-1	0.6	0.63	2.03	5.7	0.70
HMEA-2	1.0	0.81	2.34	8.2	0.69
HMEA-3	1.2	0.95	2.25	6.9	0.68
HMEA-4	1.2	1.25	2.80	4.8	0.67
HMEA-N	1.0	0.74	3.08	1.5	0.69

(a) The O_2 effective diffusion coefficient in the gas diffusion layer ($D_{\mathrm{GDL}}^{\mathrm{eff}}$), the O_2 effective diffusion coefficient in the catalyst layer ($D_{\mathrm{CL}}^{\mathrm{eff}}$) and the reference O_2 concentration at the agglomerate surface ($C^{\mathrm{ref}}_{\mathrm{o}}$). (b) The ratio of the volume fraction of liquid (v_l) to the void fraction (v_v) is the extent of flooding (v_l / v_v). (c) Half-membrane electrode assembly (HMEA) consists of a GDE and a membrane; for Nafion (MEA-N) and for ETFE-g-PSSA with 3.27, 2.56, 2.45 and 2.13 mmol g^{-1} (HMEA-1 to HMEA-4, respectively). Data for HMEAs are re-calculated from experimental results obtained under half-fuel cell conditions (ref. 9). (d) Least square fitting error of current density at potential between OCV and 0.75 V.

5.5.2 Diffusion of Oxygen

A simple model of percolation in the gas-pore space is used to calculate the extent of flooding in the void space in the catalyst layer. The description of this approach has been reported in section 4.4.5 of the previous chapter. Oxygen is assumed to move in the catalyst layer via coexisting pathways of gas and liquid diffusion. The effective diffusion constant D_{CL}^{eff} consists of a gaseous phase diffusion component (D_g) and a residual diffusion (D_r), which represents diffusion in liquid and hydrated polymer network. Because the electrode composition used in this work provides similar volume fraction of void space (0.46, see Table 5.7) to that used in the half-fuel cell study, the residual diffusion coefficient (D_r) calculated from Equation (53) to be ~ 1.5 x 10^{-7} cm^2 s^{-1} also indicates a negligible contribution (less than ~1 %) to D_{CL}^{eff} (10^{-5} – 10^{-6} cm^2 s^{-1}). It is justifiable to neglect the contribution from D_r. In fact, this demonstrates that liquid water diffusion alone could not sustain acceptable levels of fuel cell performance. It is, therefore, justifiable to neglect any contribution from diffusion in liquid and polymer phase in the catalyst layer, unless it is prepared very thin.

Table 5.7: Values of volume fraction calculated from the catalyst layer composition and its dimension (5.06 cm^2 and ~50 μm thick)

Composition (dry)	Pt	C	Nafion	Void	Total
Volume Fraction	0.01	0.42	0.11	0.46	1.00

The values of the extent of flooding ($\frac{V_l}{V_v}$) for the MEAs were calculated using the simple model of percolation in gas-pore space (Equation 60), and are listed in Table 5.6. For comparison, the values of $\frac{V_l}{V_v}$ for the HMEAs are included in Table 5.6. Under fuel cell conditions, the extent of flooding ranges from 58 to 65 %, increasing with IEC. Remarkably, the reverse trends are observed for the effect of IEC on the extent of flooding for the series of MEAs and HMEAs. For the MEAs $\frac{V_l}{V_v}$ increases with decreasing IEC, whereas for the HMEAs $\frac{V_l}{V_v}$ was found to decrease with decreasing IEC. This is partly attributed to the intrinsic differences between the half-fuel cell and the fuel cell conditions. The supply of water to the cathode from the membrane is limited under the fuel cell conditions, whereas excess liquid is supplied from bulk H_2SO_4 electrolyte in the half-fuel cell. This apparent discrepancy is thought to connect to the basic mechanisms of membrane operation, as it will be elaborated in the subsequent section.

5.5.3 Physical Model for the Influence of Membrane on Catalyst Layer Performance

The opposite trends in orr polarization and extent of flooding (Table 5.6) found in the MEA and HMEA series upon decreasing IEC can be explained by considering water transport in the two systems.

Transport of water in the membrane consists of electro-osmotic drag and backtransport by diffusion or hydraulic permeation. The net flux of water in the membrane can be expressed as[2]

$$N_w = n(\lambda) j_p - \frac{K(\lambda)}{\mu} \frac{dp}{dx} \tag{70}$$

The first term represents electro-osmotic drag, which is related to protonic current density (j_p) by the water content dependent drag coefficient (n). The second term is Darcy's law representing backtransport driven by hydraulic pressure gradient (dp/dx). In general, backtransport may consist of a diffusion and a permeation contributions[1]. Within this context, only the latter is considered. The essential properties in backtransport are the permeability (K), and viscosity (μ). These are characteristics of the water/membrane system determined by the morphology of the membrane, i.e. the water distribution and porous structure effects.

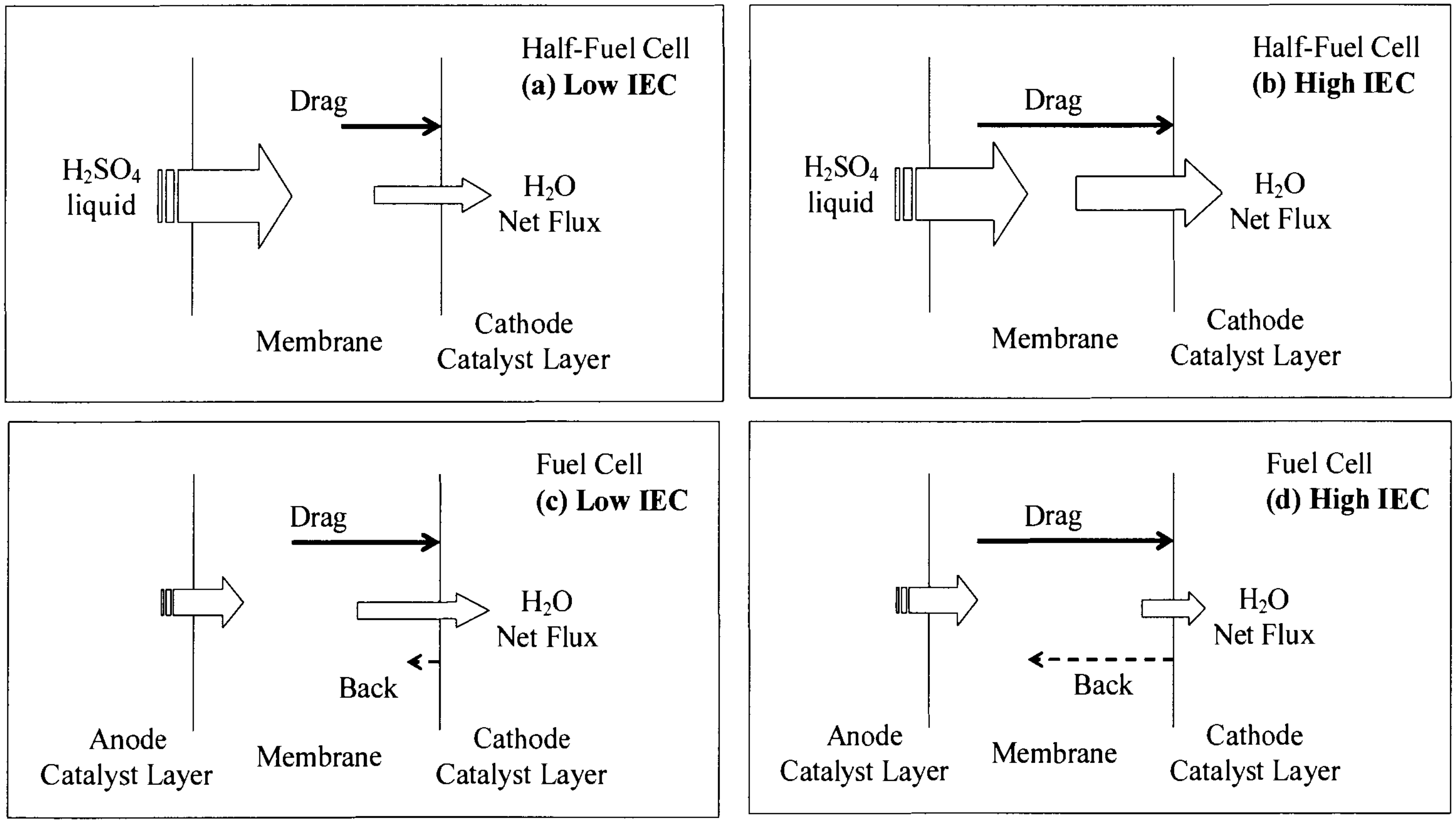

Figure 5.11: Schemes for the influence of membrane on water transport in half-fuel cell (a, b) and fuel cell conditions (c, d) containing low and high IEC membranes, respectively.

Under half-fuel cell conditions, the membrane is always completely wetted (saturated) due to excess liquid electrolyte supplied on the anode side. Therefore, backtransport can be considered negligible, because (d*p*/d*x*) is very small. Water transport from the membrane to the cathode is, thus, mainly controlled by electroosmotic drag, i.e. by $n(\lambda)$. Membranes with higher IEC possess larger saturation water contents (see, Figure 5.11) and correspondingly larger electro-osmotic drag coefficients. The net water transport to the cathode increases with IEC in the HMEA systems. Consequently, the extent of flooding in the cathode is higher and the orr polarization is lower. This explains experimental observations in the previous work[61].

Under fuel cell conditions (MEAs), the electro-osmotic and the backtransport interplay, c.f. Figure 5.11. The effect of IEC on electroosmotic drag will be similar as for the HMEAs. However, under fuel cell conditions no excess water supply from the anode side is provided. Therefore, (d*p*/d*x*) will be finite, generating a hydraulic backflow of water. Apparently, the effect of IEC on $n(\lambda)$ is overcompensated by the effect of IEC on permeability, $K(\lambda)$. Larger IEC corresponds to water uptake, larger mean pore radii and, thus, effectuates larger values of $K(\lambda)$. Consequently, the lower IEC increases the extent of flooding in the catalyst layer, reduces the oxygen transport and fuel cell performance. Overall, this deduction affirms that higher IEC facilitates membrane and catalyst layer water management in MEAs.

This simple line of reasoning demonstrates the capabilities half-fuel cell and fuel cell measurements. Used concertedly, they can be employed in order to discriminate effects of electro-osmotic drag and backtransport of water. Measurements performed under negligible backtransport, using half-fuel cell system, can be used to extract the drag coefficient if the water flux from the membrane to the cathode is known. This can be determined by measuring the water flux from the cathode gas diffusion layer. Once the drag coefficient is known, the permeation coefficient (*K*) can be extracted from the fuel cell measurements. Moreover, this study may have implications for the deliberate design of membranes with improved water management, in which electroosmotic drag and backtransport can be controlled independently.

5.6 Conclusion

In addition to fulfilling the primary requirements of proton conduction and gas separation in the PEMFCs, the physicochemical properties of the membrane affect the electrochemical performance and water management in the fuel cell. The IEC of the membrane affects catalyst layer hydration of the cathode, quality of the membrane / GDE interface and back-diffusion of water to the anode. The agglomerate model and percolation theory, used to analyse half-fuel cell and fuel cell data, indicate that under the fuel cell conditions employed more facile gas transport in the cathode is observed as a result of more facile water removal via the gas diffusion layer and/or backtransport through the membrane. Flooding of the cathode catalyst layer in the fuel cell is not as extensive as in the case of the half-fuel cell and the decrease in electrochemically active catalyst surface area, due to reduced wetting of the catalyst layer, is offset by increased O_2 mass transport kinetics. Opposite trends in effects of IEC on performance in fuel cell and half fuel cell systems were explained invoking the water balance in the membrane. In half fuel cells the effect of increasing electroosmotic drag with increasing IEC dominates, whereas under fuel cell conditions this effect is overcompensated by increasing permeability and, thus, increased water backtransport with increased IEC. Membranes with larger IEC improve fuel cell performance and they facilitate fuel cell water management.

5.7 Appendix

5.7.1 Estimation of the Effective Proton Conductivity in the Catalyst Layer.

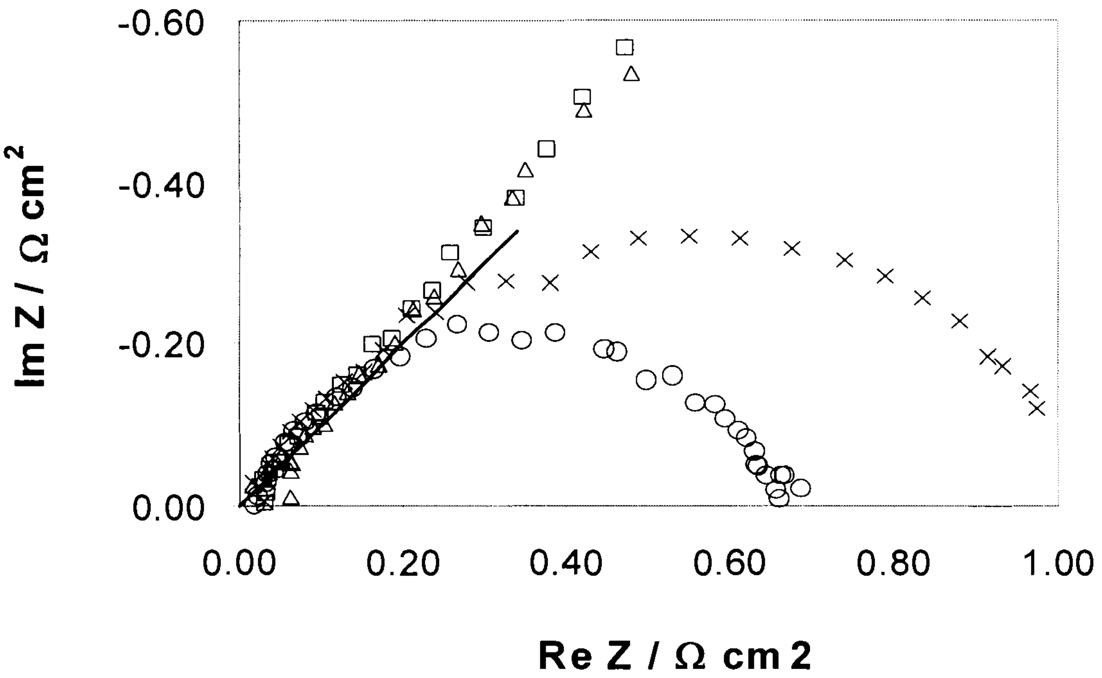

Figure 5.12: Ru corrected EIS spectra of MEA-1 measured from 0.1 to 2000 Hz and 5 mV perturbation amplitude. Bias potential 0.90 V (△), 0.70 V (X), 0.50 V (O) and open circuit potential (□). Solid line (—) represents the 45° gradient line.

The effective proton conductivity in the catalyst layer, σ^{eff}, is estimated from EIS spectra. A typical Nyquist plot of Z(Re) against Z(Im) is shown in

Figure 5.12 for MEA-1 under increasing polarization. For all MEAs the spectra showed a common linear feature at the high frequency limit. The gradient of the high frequency linear regime (~ 10^2 - 10^3 Hz) is 48 ± 4°, which is in good agreement with the theoretical value of 45° [23]. According to theory [23], in this high frequency regime double layer charging effects (C_{dl}) and proton transport resistance (R_p) dominate the overall electrode response. The linear feature corresponds to an electrode operating under a limiting proton transport case (i.e. either fast O_2 transport and slow proton conduction or slow O_2 and slow proton transport). The electrode EIS spectrum can be expressed by

$$|Z| = \sqrt{\frac{R_p}{C_{dl}}}\omega^{-1/2} \qquad (71)$$

where $|Z|$,ω and C_{dl} represent the magnitude of the impedance, the frequency of perturbation and the double layer capacitance of the electrode, respectively.

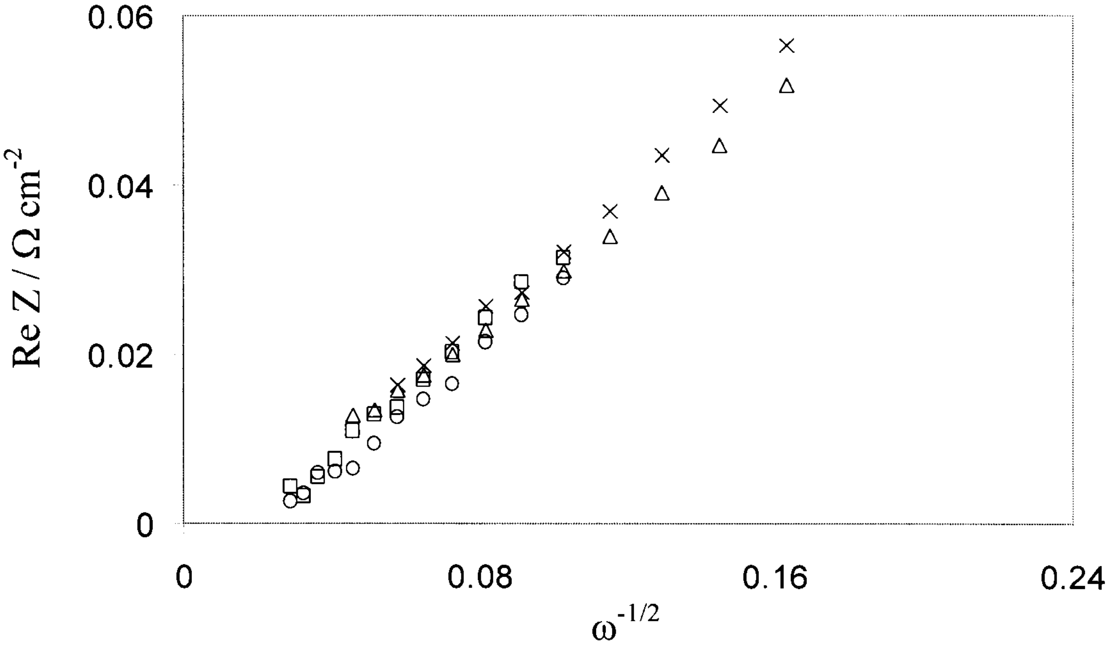

Figure 5.13: Linear plot of real imdepance (Z') against ω-1/2 at 0.90 V bias potential. MEA-1 (△), MEA-3 (□), MEA-4 (X), and MEA-N (O). MEA-2 and MEA-5 are omitted for clarity.

A plot of $|Z|$ against $\omega^{-1/2}$ for the MEAs, illustrated in Figure 5.13, shows a common linear region as predicted from theory. The slopes for all MEAs are very similar, possessing an average value of 0.361 ± 0.013. The integral capacitance (capacitance per unit area of electrode) is estimated from cyclic voltammetry (Figure 1) in the potential region 0.35 to 0.45 V and the values of R_p obtained from the slopes ($\sqrt{\frac{R_p}{C_{dl}}}$) are listed in Table 5.5. The integral capacitance, exhibiting an average value of ~ 85 mF cm^{-2}, shows a slight increase with increasing IEC of the membrane: this is consistent with the increase in ESA.

Chapter 6 : Summary and Future Work

In this thesis, the effect of ion exchange capacity (IEC) on the electrochemical oxygen reduction reaction in the catalyst layer was investigated under half-fuel cell and fuel cell conditions using a series of radiation-grafted tetrafluoroethylene-g-polystyrene sulfonic acid (ETFE-g-PSSA) membranes to provide a systematic variation of IEC. It was found that, in addition to controlling morphology and water distribution in the membrane, the IEC regulated the water balance in the complete MEA. This influence was most significant in the cathode catalyst layer, where it affected mass transport and electrochemical characteristics.

In the half-fuel cell system, the half-membrane electrode assemblies containing higher IEC yielded higher electrochemically active surface area. In contrast, they exhibited lower oxygen reduction performance. The membrane influenced the catalyst layer by facilitating wetting. Using the agglomerate model for a PEMFC cathode and a simple model of percolation for gas-pores, it was estimated that 67 to 70% (increasing with IEC) of void space in the catalyst layer was filled with water. The IEC regulated the extent of flooding in the cathode, which in turn affected its electrochemical characteristics.

Under hydrogen/oxygen fuel cell conditions, the beginning-of-life polarization curves showed an increase in performance with increasing IEC – a contradicting trend to that observed under the half-fuel cell system. This was explained in terms of the interplay between electroosmotic flux and hydraulic counterflux of water in the membrane. The higher IEC, which corresponded to higher water uptake and larger mean pore radii, effectuated larger backtransport of water and found to reduce a likelihood of membrane dehydration. During fuel cell operation, an increase in the electroosmotic flux was overcompensated by the backtransport counterflux. Consequently, the higher IEC reduced the extent of flooding in the catalyst layer, improved the oxygen transport and increased fuel cell performance. This provided an insight into how the IEC facilitated membrane and catalyst layer water management in MEAs. The electrochemically active surface area (ESA) was found to have a slight dependence on IEC - a consistent trend to that observed under the half-fuel cell system.

In addition to investigating the effect of membrane's IEC, this thesis also highlighted the capabilities of half-fuel cell and fuel cell systems as tools for electrochemical characterization. The former operated under an excess supply of liquid electrolyte to the membrane. Such a simplified experimental arrangement simulated fuel cell operating under extreme conditions where backtransport of water is neglected. Therefore the half-fuel cell system is unsuitable for mass transport investigations under practical PEMFC operating conditions. However, the measurement of ESA provides the maximum accessible area of the electrode. On the other hand, experiments performed using an operating fuel cell provides a useful performance evaluation but often contain complicating factors such as effects of membrane dehydration and interfacial resistances, both of which can be measured and compensated for. Comparing the ESA obtained under the two experimental conditions provides valuable insight into the state of hydration and the effective use of Pt in the catalyst layer. The ESA measured under fuel cell conditions was lower as a result of reduced wetting of the catalyst layer (finite supply of water to the cathode) but this was offset by an order of magnitude increase of the effective O_2 diffusion. Consequently oxygen reduction reaction performance was higher in the fuel cell system.

It is proposed that the individual effect of electroosmotic drag and backtransport of water in the membrane can be elucidated if the half-fuel cell and the fuel cell systems are used concertedly. An experimental setup using a half-fuel cell to measure the water flux from the cathode gas diffusion layer at different current densities can, in principle, be used to extract the drag coefficient (Equation 70 when the back permeation is assumed negligible). Once the drag coefficient is known, the permeability coefficient can be determined using the fuel cell system to measure the net water flux through the membrane at different current densities and pressure gradients across it. The technical challenge in this approach is how to accurately measure the net water flux. Solving this challenge may involve measuring the water balance from the inlets and the outlets of an operating fuel cell, and using these values to calculate the net water flux through the membrane from a mass balance equation.

For a membrane consisting of a hydrophobic backbone and the hydrophilic proton conducting phase like Nafion and ETFE-g-PSSA, an increase in IEC often increases water content and pore radii, leading to an increase in both the electroosmotic drag and the back-permeation coefficients. The work in this thesis may have implications in the deliberate design of membranes with improved water management, in which the electroosmotic drag and the backtransport can be controlled independently. Such membrane may contain, in addition to the hydrophobic backbones and the ionic hydrophilic proton conducting groups, a network of non-proton conducting group, which may serve as independent pathways for water transport independent to the interfering effects of electroosmotic drag.

Bibliographies:

1. F. Meier and G. Eigenberger, Electrochim. Acta 49 (2004) 1731.
2. M. Eikerling, Yu. I. Kharkats, A. A. Kornyshev, and Yu. M. Volfkovich, J. Electrochem. Soc. 145 (1998) 2684.
3. T. A. Zawodzinski, J. Davey, J. Valerio, and S. Gottesfeld, Electrochim. Acta 40 (1995) 297.
4. M. Ise, K. D. Kreuer, and J. Maier, Solid State Ionics 125 (1999) 213.
5. R. Satija, D. L. Jacobson, M. Arif, and S. A. Werner, J. Power Sources 129 (2004) 238.
6. W. He, G. Lin, and T. Van Nguyen, AIChE. 49 (2003) 3221.
7. D. Natarajan and T. Van Nguyen, J. Power Sources 115 (2003) 66.
8. T. Van Nguyen and M. W. Knobbe, J. Power Sources 114 (2003) 70.
9. J. Chen, T. Matsuura, and M. Hori, J. Power Sources 131 (2004) 155.
10. W. M. Yan, F. Chen, H. Y. Wu, C. Y. Soong, and H. S. Chu, J. Power Sources 129 (2004) 127.
11. A. J. Bard and R. L. Faulkner, Electrochemical Methods, Fundamentals and Applications, Wiley Interscience, New York, 1980.
12. K. Kinoshita and P. Stonehart, in: J.OM.Bockris and B.E.Conway (Eds.), Highly Dispersed Electrocatalytic Materials, Vol. 12, Plenum Press, New York, 1977, Ch. 4.
13. P. Costamagna and S. Srinivansan, J. Power Sources 102 (2001) 242.
14. K. Kinoshita, Electrochemical Oxygen Technology, Wiley-Interscience, New York, 1992.

15. U. A. Paulus, T. J. Schmidt, H. A. Gasteiger, and R. J. Behm, J. Electroanal. Chem. 495 (2001) 134.

16. F. N. Buchi, B. Gupta, O. Haas, and G. G. Scherer, Electrochim. Acta 40 (1995) 345.

17. R. A. Assink, C. Arnold, and R. P. Hollandsworth, J. Membr. Sci. 56 (1991) 143.

18. R. Hodgdon, J. R. Boyack, and A. B. LaConti, Advance Development and Laboratory Technical Report, No. 65DE5, General Electric Co., West Lynn, MA, USA, 1966.

19. A. Damjanovic and J. OM. Bockris, Electrochim. Acta 11 (1966) 376.

20. A. Damjanovic, in: J.OM.Bockris and B.E.Conway (Eds.), Mechanistic Analysis of Oxygen Electrode Reactions, Plenum Press, New York, 1969, Ch. 5.

21. A. Damjanovic and V. Brusic, Electrochim. Acta 12 (1967) 615.

22. K. Mauritz, Nafion -Perfluorosulfonate Ionomer, <http://www.psrc.usm.edu/mauritz/nafion.html>, last retrieved 29/June/2004

23. J. Mirzazadeh, E. Saievar-Iranizad, and L. Nahavandi, J. Power Sources 131 (2004) 194.

24. G. G. Park, Y. J. Sohn, T. H. Yang, Y. G. Yoon, W. Y. Lee, and C. S. Kim, J. Power Sources 131 (2004) 182.

25. E. A. Ticianelli, C. R. Derouin, and S. Srinivansan, J. Electroanal. Chem 251 (1989) 275.

26. J. S. Newman and C. W. J. Tobias, J. Electrochem. Soc. 109 (1962) 1183.

27. Y. Volkman, Electrochim. Acta 24 (1978) 1145.

28. A. W. Bryson and K. A. Dardis, J. Chem. Tech. Biotechnol. 30 (1980) 14.

29. F. Lapicque, A. Storck, and A. A. Wragg, Electrochemical Engineering and Energy, Plenum Press, New York, 1994.

30. H. Wendt, Electrochemical engineering : science and technology in chemical and other industries, Springer-Verlag, New York, 1999.

31. I. D. Raistrick, Electrode assembly for use in solid polymer electrolyte fuel cell, U.S. Patent No. 4,876,115 (1989)

32. E. A. Ticianelli, C. R. Derouin, A. Reodndo, and S. Srinivansan, J. Electrochem. Soc. 135 (1988) 2209.

33. M. S. Wilson and S. Gottesfeld, J. Appl. Electrochem. 22 (1992) 1.

34. S. Srinivansan, E. A. Ticianelli, C. R. Derouin, and A. Redondo, J. Power Sources 22 (1988) 359.

35. E. A. Ticianelli, C. R. Derouin, and S. Srinivansan, J. Electroanal. Chem 251 (1988) 275.

36. P. Costamagna and S. Srinivansan, J. Power Sources 102 (2001) 253.

37. M. S. Wilson, J. A. Valerio, and S. Gottesfeld, Electrochim. Acta 40 (1995) 355.

38. S. Y. Cha and W. M. Lee, J. Electrochem. Soc. 146 (1999) 4055.

39. G. S. Kumar, M. Raja, and S. Parthasarathy, Electrochim. Acta 40 (1995) 285.

40. R. O'Hayre, S. J. Lee, S. W. Cha, and F. Prinz, J. Power Sources 109 (2002) 483.

41. M. S. Wilson, Membrane Catalyst Layer for Fuel Cell, U.S. Patent No. 5,234,777 (1993)

42. V. A. Paganin, E. A. Ticianelli, and E. R. Gonzalez, J. Appl. Electrochem. 26 (1996) 297.

43. C. Marr and X. Li, J. Power Sources 77 (1999) 17.

44. Z. Qi and A. Kaufman, J. Power Sources 113 (2003) 37.

45. S. J. Lee, S. Mukerjee, J. McBreen, Y. W. Rho, Y. T. Kho, and T. H. Lee, Electrochim. Acta 43 (1998) 3693.

46. P. Gode, F. Jaouen, G. Lindbergh, A. Lundblad, and G. Sundholm, Electrochim. Acta 48 (2003) 4175.

47. E. Antolini, L. Giorgi, A. Pozio, and E. Passalacqua, J. Power Sources 77 (1999) 136.

48. A. Eisenberg and H. L. Yeager, Perfluorinated Ionomer Membranes, American Chemical Society, Washington D.C., 1982.

49. V. I. Basura, C. Chuy, P. D. Beattie, and S. Holdcroft, J. Electroanal. Chem. 501 (2001) 77.

50. F. N. Buchi, M. Wakizoe, and S. Srinivansan, J. Electrochem. Soc. 143 (1996) 927.

51. A. Parthasarathy, B. Dave, S. Srinivansan, A. J. Appleby, and C. R. Martin, J. Electrochem. Soc. 139 (1992) 1634.

52. T. D. Gierke, Proceeding of the 152nd. Meeting of the Electrochemical Society, Atlanta, GA, 1977.

53. E. J. Roche, M. Pineri, R. Duplessix, and A. M. Levelut, J. Polym. Sci. Polym. Phys. Ed. 2 (1982) 107.

54. A. L. Rollet, O. Diat, and G. Gebel, J. Phys. Chem. B 106 (2002) 3033.

55. O. Savadogo, J. New Mat. Electrochem. Systems 1 (1998) 47.

56. A. E. Steck, in: O.Savadogo and P.R.Roberge (Eds.), Proceedings of the First International Symposium on New Material Fuel Cell Systems, Part I, Ecole Polytechnique de Montreal, Canada, 2003.

57. M. Doyle and G. Rajendran, in: W.Vielstich and H.A.Gasteiger (Eds.), Handbook of Fuel Cells, Wiley, Chichester, England, 2003.

58. V. I. Basura, P. D. Beattie, and S. Holdcroft, J. Electroanal. Chem. 458 (1998) 1.

59. P. D. Beattie, V. I. Basura, and S. Holdcroft, J. Electroanal. Chem. 468 (1999) 180.

60. A. S. Arico, V. Baglio, P. Creti, A. Di Blasi, V. Antonucci, J. Brunea, A. Chapotot, A. Bozzi, and J. Schoemans, J. Power Sources 123 (2003) 107.

61. T. Navessin, S. Holdcroft, Q. Wang, D. Song, Z. Liu, M. Eikerling, J. Horsfall, and K. V. Lovell, J. Electroanal. Chem. 567 (2004) 111.

62. J. Horsfall and K. V. Lovell, Fuel Cells 1 (2001) 186.

63. J. A. Horsfall and K. V. Lovell, Euro. Polym. J. 38 (2002) 1671.

64. B. Gupta, F. N. Buchi, G. G. Scherer, and A. Chapiro, Solid State Ionics 61 (1993) 213.

65. S. D. Flint and R. C. T. Slade, Solid State Ionics 97 (1997) 299.

66. J. L. Bredas, R. R. Chance, and R. Silbey, Phys. Rev. B. 26 (1982) 5843.

67. H. Kobayashi, H. Tomita, and H. Moriyama, J. Am. Chem. Soc. 116 (1994) 3153.

68. F. Wang and J. Roovers, Macromolecules 26 (1993) 5295.

69. C. Bailey, D. J. Williams, F. E. Karasz, and W. J. Macknight, Polymer 28 (1987) 1009.

70. B. Adams and E. Holmes, J. Soc. Chem. Ind. IT (1935) 54.

71. W. Jr. Mitchell, Fuel Cells, Academic Press, New York, 1963.

72. L. E. Chapman, Proc. 7th Intersoc. Energy Conv. Eng. Conf., (1972) 466

73. Jr. R. B. Hodgdon, U.S. Patent No. 3,341,366 (1967)

74. J. Larminie and A. Dicks, Fuel Cell Systems Explained, John Wiley and Sons, Chichester, UK, 2000.

75. C. Chuy, V. I. Basura, E. Simon, S. Holdcroft, J. Horsfall, and K. V. Lovell, J. Electrochem. Soc. 147 (2000) 4453.

76. J. Huslage, T. Rager, B. Schnyder, and A. Tsukada, Electrochim. Acta 48 (2002) 247.

77. T. Kallio, M. Lundstrom, G. Sundholm, N. Walsby, and F. Sundholm, J. Appl. Electrochem. 32 (2002) 11.

78. N. Walsby, F. Sundholm, T. Kallio, and G. Sundholm, J. Polym. Sci. Polym. Part A 39 (2001) 3008.

79. B. Gupta, F. N. Buchi, and G. G. Scherer, J. Polym. Sci. Polym. Part A 32 (1994) 1931.

80. N. Walsby, M. Paronen, J. Juhanoja, and F. Sundholm, J. Polym. Sci. Polym. Part A 38 (2000) 1512.

81. C. Chuy, J. F. Ding, E. Swanson, S. Holdcroft, J. Horsfall, and K. V. Lovell, J. Electrochem. Soc. 150 (2003) E271.

82. C. Chuy, Influence of Morphology on the Electrochemical Properties of Proton Exchange Membranes, thesis, Simon Fraser University, 2002.

83. V. I. Basura, Elctrochemistry of Proton Exchange Membranes, thesis, Simon Fraser University, 2000.

84. P. Gode, G. Lindbergh, and G. Sundholm, J. Electroanal. Chem. 518 (2002) 115.

85. F. Jaouen, G. Lindbergh, and K. Wiezell, J. Electrochem. Soc. 150 (2003) A1711.

86. B. Andreaus and G. G. Scherer, Solid State Ionics 168 (2004) 311.

87. D. Song, Q. Wang, Z. Liu, T. Navessin, M. Eikerling, and S. Holdcroft, J. Power Sources 126 (2004) 104.

88. Q. Wang, D. Song, M. Eikerling, T. Navessin, Z. Liu, and S. Holdcroft, Electrochim.Acta, accepted

89. M. Perry, J. Newman, and E. Cairns, J. Electrochem. Soc. 145 (1998) 5.

90. F. Jaouen, G. Lindbergh, and G. Sundholm, J. Electrochem. Soc. 149 (2002) A437.

91. L. Giorgi, E. Antolini, A. Pozio, and E. Passalacqua, Electrochim. Acta 43 (1998) 3675.

92. N. Jia, R. B. Martin, Z. Qi, M. C. Lefebvre, and P. G. Pickup, Electrochim. Acta 46 (2001) 2863.

93. T. Navessin, M. Eikerling, Q. Wang, D. Song, Z. Liu, J. Horsfall, K. V. Lovell, and S. Holdcroft, J.Electrochem.Soc., accepted.

94. M. Uchida, Y. Aoyama, N. Eda, and A. Ohta, J. Electrochem. Soc. 142 (1995) 4143.

95. D. M. Bernadi and M. W. Verbrugge, J. Electrochem. Soc. 139 (1992) 2477.

96. F. Gloaguen, P. Convert, S. Gamburzev, O. A. Velev, and S. Srinivasan, Electrochim. Acta 43 (1998) 3767.

97. T. E. Springer, M. S. Wilson, and S. Gottesfeld, J. Electrochem. Soc. 140 (1993) 3513.

98. M. Eikerling and A. A. Kornyshev, J. Electroanal. Chem. 453 (1998) 89.

99. Y. W. Rho and S. Srinivansan, J. Electrochem. Soc. 141 (1994) 2089.

100. F. Jaouen, G. Lindbergh, and F. Sundholm, J. Electrochem. Soc. 149 (2002) A437.

101. H. S. Fogler, Elements of Chemical Reaction Engineering, 3rd ed., Prentice Hall, Upper Saddle River, NJ, 1999.

102. T. Doherty, J. G. Sunderland, E. P. L. Roberts, and D. J. Pickett, Electrochim. Acta 41 (1996) 519.

103. Q. Wang, M. Eikerling, D. Song, Z. Liu, T. Navessin, Z. Xie, and S. Holdcroft, J.Electrochem.Soc., In press

104. F. Wang, M. Hickner, Y. S. Kim, T. A. Zawodzinski, and J. E. McGrath, J. Membr. Sci. 197 (2002) 231.

105. J. R. Macdonald, Impedance Spectroscopy, Wiley Interscience, New York, 1987.

106. C. L. Gardner and A. V. Anantaraman, J. Electroanal. Chem. 395 (1995) 67.

107. J. R. Selman and Y. P. Lin, Electrochim. Acta 38 (1993) 2063.

108. P. D. Beattie, F. P. Orfino, V. I. Basura, K. Zychowska, J. F. Ding, C. Chuy, J. Schmeisser, and S. Holdcroft, J. Electroanal. Chem. 503 (2001) 45.

109. B. Andreaus, A. J. McEvoy, and G. G. Scherer, Electrochim. Acta 47 (2002) 2223.

110. M. Uchida, Y. Aoyama, N. Eda, and A. Ohta, J. Electrochem. Soc. 142 (1995) 463.

111. L. Giorgi, E. Antolini, A. Pozio, and E. Passalacqua, Electrochimica Acta. 43 (1998) 3675.

112. O. Antoine, Y. Bultel, and R. Durand, J. Electroanal. Chem 499 (2001) 85.

113. S. Brunauer, P. H. Emmet, and E. Teller, J. Am. Chem. Soc. 60 (1938) 1553.

114. S. Gilman, J. Phys. Chem 67 (1963) 78.

115. S. Gilman, J. Electroanal. Chem 7 (1964) 382.

116. F. G. Will, J. Electrochem. Soc. 112 (1965) 451.

117. J. Bett, K. Kinoshita, K. Routsis, and P. Stonehart, J. Catalysis 29 (1973) 160.

118. K. Kinoshita, J. Lundquist, P. Ross, and P. Stonehart, J. Catal. 31 (1973) 325.

119. K. F. Blurton, P. Greenberg, H. G. Oswin, and D. R. Rutt, J. Electrochem. Soc. 119 (1972) 559.

120. E. Gileadi, Electrode Kinetics for Chemists, Chemical Engineers and Material Scientists, VCH, New York, 1993.

121. Princeton Applied Research, Electrochemical Division, Technical Note 101: Potential Error Correction (iR compensation), 1999

122. L. L. Scribners and S. R. Taylor, The Measurement and Correction of Electrolyte Resistance in Electrochemical Tests, ASTM, Philadephia, PA, 1990.

123. A. Pozio, M. D. Francesco, A. Cemmi, F. Cardellini, and L. Giorgi, J. Power Sources 105 (2003) 13.

124. D. R. Lide, CRC Handbook of Chemistry and Physics, 83rd ed. ed., CRC Press, Cleveland, 2002.

125. D. Stauffer and A. Aharony, Introduction to Percolation Theory, 2nd ed., Taylor & Francis, Washington DC, 1992.

126. M. B. Ilsichenko, Rev. Mod. Phys. 64 (1992) 961.

127. Cabot Corporation, Material Safety Data Sheet: Carbon Black, 1999

128. DuPont Fuel Cells, DuPont Product Information: Nafion Membranes Extrusion-Cast, 2002

129. C. N. Satterfield and T. K. Sherwood, The Role of Diffusion in Catalysis, Addison-Wesley, Reading, MA, 1963.

130. T. K. Tokunaga, J. Chem. Phys. 82 (1985) 5298.

131. K. Kinoshita, Carbon: Electrochemical and Physicochemical Properties, Wiley Interscience, New York, 1988.

132. Z. Qi and A. Kaufman, J. Power Sources 114 (2003) 21.

133. T. R. Ralph, G. A. Hards, J. E. Keating, S. A. Campbell, D. P. Wilkinson, M. Davis, J. St-Pierre, and M. C. Johnson, J. Electrochem. Soc. 144 (1997) 3845.

134. F. N. Buchi and G. G. Scherer, J. Electroanal. Chem. 404 (1996) 37.

135. Scribner Associates Inc, FuelCell Software Operating Manual, 2001

136. T. Mennola, M. Mikkola, M. Noponen, T. Hottinen, and P. Lund, J. Power Sources 112 (2002) 261.

137. J. F. Connolly, R. J. Flannery, and G. Aronowitz, J. Electrochem. Soc. 113 (1966) 577.

138. M.Eikerling and A.A.Kornyshev, J. Electroanal. Chem 475 (1999) 107.